Corrections in clinical Magnetic Resonance Spectroscopy and SPECT

Motion correction in MR spectroscopy Downscatter correction in SPECT

de Nijs, Robin

Publication date:
2010

Document Version
Publisher's PDF, also known as Version of record

Corrections in clinical Magnetic Resonance Spectroscopy and SPECT

Motion correction in MR spectroscopy
Downscatter correction in SPECT

Robin de Nijs, MSc, PDEng

August 2009
IMM-PHD-2009-221

Technical University of Denmark
Informatics and Mathematical Modelling
Building 321, DK-2800 Kongens Lyngby, Denmark
Phone +45 45253351, Fax +45 45882673
reception@imm.dtu.dk
www.imm.dtu.dk

Danish Research Centre for Magnetic Resonance
Copenhagen University Hospital, Hvidovre
Section 340, Kettegaard Allé 30, DK-2650 Hvidovre, Denmark
Phone +45 36322885, Fax +45 36470302
www.drcmr.dk

Neurobiology Research Unit
Copenhagen University Hospital, Copenhagen
Building 9201, Juliane Maries Vej 24, DK-2100 Copenhagen, Denmark
Phone +45 35456711, Fax +45 35456713
info@nru.dk
www.nru.dk

Summary

The quality of medical scanner data is often compromised by several mechanisms. This can be caused by both the subject to be measured and the scanning principles themselves. In this PhD project the problem of subject motion was addressed for Single Voxel MR Spectroscopy in a cohort study of preterm infants. In Iodine-123 SPECT the problem of downscatter was addressed. This thesis is based on two papers.

Paper I deals with the problem of motion in Single Voxel Spectroscopy. Two novel methods for the identification of outliers in the set of repeated measurements were implemented and compared to the known mean and median filtering. The data comes from non-anesthetized preterm infants, where motion during scanning is a common problem. Both the novel outlier identification and the independent component analysis (ICA) perform satisfactory and better than the common mean and median filtering. ICA performed best in the sense that it recovered most of the lost peak height in the spectra.
The ICA motion correction algorithm described in paper I and in this thesis was applied to a quantitative analysis of the Single Voxel Spectroscopy data from the cohort study of preterm infants. This analysis revealed that differences between term and preterm infants are not to be found in the concentrations of Lactate (caused by inflammation or hypoxia-ischemia) and/or NAA (caused by hypoxia-ischemia) as hypothesized before the cohort study. Instead choline levels were decreased in the preterm infants, which might indicate a detrimental effect of the extra-uterine environment on brain development.

Paper II describes a method to correct for downscatter in low count Iodine-123 SPECT with a broad energy window above the normal imaging window. Both spatial dependency and weight factors were measured. As expected, the implicitly assumed weight factor of one for energy windows with equal width is slightly too low, due the presence of a backscatter peak in the energy spectrum coming from high-energy photons. The effect on the contrast was tested in 10 subjects and revealed a 20% increase in the specific binding ratio of the striatum due to downscatter correction. This makes the difference between healthy subjects and patients more profound.

Downscatter in Iodine-123 SPECT is not the only deteriorating mechanism. Normal scatter compromises the images quality as well. Since scatter correction of SPECT-images also can be performed by the subtraction of an energy window, a method was developed to perform scatter and downscatter correction simultaneously. A phantom study has been performed, where the in paper II described downscatter correction was extended with scatter correction. This new combined correction was compared to the known Triple Energy Window (TEW) correction method. Results were satisfying and indicate that TEW is more correct from the physics point of view, while the in paper II described method extended with scatter correction gives reasonable results, but is far less noise sensitive than TEW.

Resume

Kvaliteten af medicinske skanneres data forringes ofte af adskillige mekanismer. Forringelserne kan forårsages både af den skannede person og selve skanningsprincipperne. I dette studie behandles problemet med patientbevægelse ved lokaliseret (single voxel) MR Spektroskopi i et kohortestudie af for tidligt fødte babyer. For Jod-123 SPECT behandles problemet med spredning af højenergetiske fotoner (downscatter). Denne afhandling er baseret på to artikler.

I artikel I behandles problemet med bevægelse ved lokaliseret (single voxel) spektroskopi. To nye metoder til identifikation af atypiske værdier (outliers) i en række af gentagne målinger er blevet implementeret og sammenlignet med gennemsnittet samt medianen. Målingerne er udført på for tidligt fødte babyer uden anvendelse af anæstesi, hvor bevægelse ofte er et problem. Både den nye outlier identifikationsmetode og den uafhængige komponentanalyse (ICA) fungerer tilfredsstillende og giver begge et bedre resultat end gennemsnittet og medianen. ICA genskabte det tabte signal bedst.
Bevægelseskorrektion ved hjælp af ICA er beskrevet i artikel I og i denne afhandling, og er anvendt på den kvantitative analyse af Single Voxel Spektroskopi data af et kohortestudie af for tidligt fødte babyer. I modsætning til hypoteserne forud for dette kohortestudie viste denne analyse, at der ikke er forskel i koncentrationer af laktat (mælkesyre, forårsaget af iltmangel eller betændelse) og NAA (forårsaget af iltmangel) mellem for tidligt fødte og ikke for tidligt fødte babyer. Cholin koncentrationer var højere i de for tidligt fødte babyer. Det tyder på en negativ effekt af de ekstra-uterine omgivelser på hjernens udvikling.

I artikel II beskrives en nyudviklet metode til at korrigere for spredning af højenergetiske fotoner ved Jod-123 SPECT med lave tælletal ved hjælp af et bredt energivindue, som er placeret over det sædvanlige billeddannende vindue. Både den rumlige afhængighed og vægtfaktorerne er blevet målt. Som forventet er den implicit antagne værdi af 1 for vægtfaktoren lidt for lav. Dette er forårsaget af en tilbagespredningstop i energispektret, som kommer fra de højenergetiske fotoner. Effekten af korrektionen på billedkontrasten er testet på 10 personer og viste en forbedring på 20% i den specifikke bindingsratio for striatum. Dette gør forskellen mellem raske personer og patienter mere udtalt.
Spredning af højenergetiske fotoner er ikke den eneste mekanisme, der forringer billedkvaliteten. Spredning af de billeddannende fotoner forringer også billedkvaliteten. Dette kan der også korrigeres for ved subtraktion af et energivindue. Der er således udviklet en metode til at korrigere for de to nævnte typer af spredning samtidigt. Et fantomstudie er udført, hvor denne nye kombinerede korrektion er sammenlignet med den kendte Triple Energy Window (TEW) korrektionsmetode. Resultaterne er tilfredsstillende og tyder på, at TEW fysisk set er mere korrekt, men at den i artikel II beskrevne metode kombineret med spredningskorrektion også giver rimelige resultater. Den sidste metode er dog meget mindre støjfølsom end TEW-metoden.

Samenvatting

De datakwaliteit van medische scanners wordt vaak verslechterd door diverse mechanismen. Dit kan zowel door de te scannen persoon als de scanprincipes zelf worden veroorzaakt. In deze studie wordt het probleem van patiëntbeweging bij gelokaliseerde (single voxel) MR Spectroscopie in een cohort studie van voortijdig geboren baby's behandeld. Voor Jood-123 SPECT wordt het probleem van de verstrooiing van hoogenergetische fotonen (downscatter) behandeld. Dit proefschrift is gebaseerd op twee artikelen.

Artikel I gaat over het probleem van beweging in gelokaliseerde (single voxel) spectroscopie. Twee nieuwe methoden voor de identificatie van uitschieters in een reeks van herhaalde metingen werden geïmplementeerd en vergeleken met het gemiddelde en de mediaan. De metingen zijn verricht bij voortijdig geboren baby's zonder toepassing van anesthesie, waar beweging een veel voorkomend probleem is. Zowel de nieuwe uitschieter identificatie methode als de onafhankelijke component analyse (ICA) voldoen en geven allebei een beter resultaat dan het gemiddelde en de mediaan. ICA herschiep de verloren gegane piekhoogte het best.

De bewegingscorrectie met ICA is beschreven in artikel I en in dit proefschrift en is toegepast op de kwantitatieve analyse van Single Voxel Spectroscopy data van een cohortstudie van voortijdig geboren baby's. Deze analyse liet zien dat er geen verschil is in de concentraties van lactaat (melkzuur, veroorzaakt door zuurstoftekort of ontsteking) en NAA (veroorzaakt door zuurstoftekort) tussen voortijdig en niet-voortijdig geboren baby's, zoals verondersteld werd voor de cohortstudie. In plaats daarvan was de choline concentratie verhoogd in de voortijdig geboren baby's. Dit duidt op een negatief effect van de extra-uterine omgeving op de ontwikkeling van de hersenen.

In artikel II wordt een nieuwe methode beschreven om voor de verstrooiing van hoogenergetische fotonen te corrigeren bij Jood-123 SPECT met slechte telstatistiek met een breed energievenster boven het normale beeldvormende venster. Zowel de ruimtelijke afhankelijkheid als de weegfactoren zijn gemeten. Zoals verwacht is de impliciet aangenomen weegfaktor van 1 enigszins te laag door de aanwezigheid van een terugverstrooiingspiek van de hoogenergetische fotonen in het energiespectrum. Het effect op het beeldcontrast is getest bij 10 personen en liet een 20% verbetering van de specifieke bindingsratio van het striatum door de verstrooiingscorrectie zien. Dit zorgt voor een meer uitgesproken verschil tussen gezonde personen en patiënten.
Verstrooiing van hoog energetische fotonen is niet het enige mechanisme dat de beeldkwaliteit verslechtert. Ook de verstrooiing van de beeldvormende fotonen verslechtert de beeldkwaliteit. Hiervoor kan ook worden gecorrigeerd met de subtractie van een energievenster. Er is een methode ontwikkeld om tegelijkertijd voor de twee genoemde typen verstrooiing te corrigeren. Een fantoomstudie is uitgevoerd, waarbij de in artikel II beschreven verstrooiing van hoogenergetische fotonen is uitgebreid met een correctie voor de verstrooiing van de beeldvormende fotonen. Deze nieuwe gecombineerde correctie is vergeleken met de bekende Triple Energy Window (TEW) correctiemethode. De resultaten waren tevredenstellend en duiden erop dat TEW natuurkundig gezien meer correct is, maar dat de in artikel II beschreven methode uitgebreid met verstrooiingscorrectie ook redelijke resultaten geeft. De laatste methode is echter veel minder ruisgevoelig dan de TEW-methode.

Preface

This PhD project was carried out at the Danish Research Centre for Magnetic Resonance (DRCMR) located at the Copenhagen University Hospital, Hvidovre and the Neurobiology Research Unit (NRU) located at the Copenhagen University Hospital, Copenhagen.

This PhD project was financially supported by Danish Medical Research Council and Copenhagen University Hospital, Hvidovre.

The project was supervised by prof. Lars Kai Hansen PhD (principal supervisor), Department of Informatics and Mathematical Modelling, Technical University of Denmark and Lars G. Hanson PhD (project supervisor), Danish Research Centre for Magnetic Resonance.

Gevninge, August 2009

Robin de Nijs

Papers

The work described in this thesis resulted in two articles as a first author:

I. de Nijs R, Miranda MJ, Hansen LK, Hanson LG. Motion correction of Single Voxel Spectroscopy by Independent Component Analysis applied to spectra from non-anesthetized pediatric subjects. *Magn Reson Med.* 2009;**62**(5):1147-54.

II. de Nijs R, Holm S, Thomsen G, Ziebell M, Svarer C. Experimental determination of the weighting factor for the energy window subtraction based downscatter correction for I-123 in brain SPECT-studies. *J Med Phys.* 2010:**35**(4):215-22.

Acknowledgements

First of all I am very grateful to the Danish Medical Research Council, which made this project financially possible.
Lars G. Hanson got me to the MR-department and helped me with sending applications for the funding of a PhD project, while I was learning about MR, and working with clinical trials for the reader centre. Without his contribution it would not have been possible to start this PhD project. Before and during the PhD project Lars used quite some time and effort to help me understand MR stuff. So a lot of thanks goes to him.
Special thanks goes to Claus Svarer at NRU for inspiring discussions about nuclear medicine. He functioned to some extend as a supervisor for this area.
I would like to thank everybody at DRCMR and NRU for the nice atmosphere.
Lars Kai Hansen's contribution with Independent Component Analysis to this project is much appreciated. It led indirectly to the first paper.
Likewise is Søren Holm's idea of a broad downscatter window appreciated. It was one of the reasons to start the research for the second paper.
Furthermore, I would like to thank Gerda Thomsen for helping me with the experiments on the SPECT scanner.

Contents

CHAPTER 1

Introduction

This thesis presents correction algorithms and methods for motion correction in Single Voxel Magnetic Resonance Spectroscopy and downscatter correction in SPECT. Methods and concepts are discussed in detail in the following chapters.

1.1 Objectives

The overall objective of this PhD was to develop corrections for often encountered deteriorating mechanisms in medical imaging. The focus was on Magnetic Resonance Spectroscopy and Single Photon Emission Computer Tomography.

Subject motion in Single Voxel Magnetic Resonance Spectroscopy was identified as a severe problem in a cohort study of preterm infants. Spectroscopic measurements need to be repeated several times in order to achieve satisfactory signal-to-noise-ratio. Motion causes uncertainty in the subject position and during motion the measurements are corrupted. The objective was to find an algorithm to identify and reject the measurements that were deteriorated and corrupted and to ensure the position of the volume of interest.

Chemical limitations makes it sometimes necessary to use radioactive isotopes that are not ideal from the physics point of view. In Single Photon Emission Computer Tomography a photon energy between 100-200 keV is preferred. Iodine-123 is such an isotope, and it emits photons with an energy of 159 keV, but unfortunately also a significant amount of photons with a higher energy. These high-energy photons loose some of their energy by scattering and partly end in the energy window used for imaging. This is called downscattering. In dynamical SPECT-studies count statistics are poor and downscatter correction with the known Triple Energy Window method is too noise sensitive. Therefore, the objective was to develop a downscatter correction for low count SPECT.

1.2 Reader's guide

This section provides a reader's guide for the thesis.

Chapter 1 is this chapter that contains the objectives and the reader's guide for this PhD-thesis.

Chapter 2 describes the basic principles of Proton Magnetic Resonance and in vivo Single Voxel Magnetic Resonance Proton Spectroscopy.

Chapter 3 deals with the motion correction of Single Voxel Spectroscopy data. Several algorithms are described, among others the well-known mean and median filtering. A novel expression for the expectation value of the difference between mean and median is given in section 3.3.2. Algorithms were tested on the data of a cohort study of preterm infants. The focus is on the motion correction, but at the end of the chapter results for metabolite ratios are given. These results would have been more difficult to obtain without motion correction. The analysis of the motion correction algorithms is published as a paper in Magnetic Resonance in Medicine.

Chapter 4 gives a general introduction to Single Photon Emission Computer Spectroscopy. A novel implementation of Chang's attenuation correction is given in section 4.1.9.

Chapter 5 describes a method to correct for downscatter by the subtraction of a broad energy window. Both weighting and spatial dependency is investigated with an I-123 point source and in a group of subjects with healthy subject and patients. These results were published

as a paper in the Journal of Medical Physics. Hereafter a phantom study is presented were scatter and downscatter correction is combined for broad energy windows, and compared to the known Triple Energy Window correction with narrow windows.

Chapter 6 contains recommendations and future outlook.

CHAPTER 2

Proton Magnetic Resonance Spectroscopy

This chapter explains the basic principles of Magnetic Resonance (MR) and MR spectroscopy, followed by a description of in vivo MR Spectroscopy using a predefined volume of interest. This is called single voxel spectroscopy (SVS). A description of the basic principles can also be found in Webb (1998) and Hanson (2008) and principles of in vivo spectroscopy can be found in Drost (2002).

2.1 Basic principles of Proton Magnetic Resonance

2.1.1 The magnetic moment

Most nuclei possess a quantum mechanical property called spin. As a consequence of this spin these nuclei have a magnetic moment. The strength of this magnetic moment is characteristic for the nucleus and determines the detection sensitivity in MR experiments. Hydrogen nuclei, i.e. protons, possess the strongest magnetic moment of all stable nuclei, which, together with the high biological abundance of hydrogen, makes it the most used nucleus in MR spectroscopy and MR imaging. The spin quantum number for protons is I=½. Associated with the spin is

the magnetic quantum number m, which can be either +½ or –½, for I=½. So, two eigenstates (energy levels) exist, which form a basis for all possible mixed states.

2.1.2 The magnetic field

In the absence of an externally applied magnetic field, the individual magnetic moments have no preferred orientation. However, if they are brought into a strong magnetic field (B_0), the magnetic moments will precess along the magnetic field and a macroscopic net stationary longitudinal magnetization parallel with the external field will gradually form (Hanson 2008) as the distribution is skewed slightly toward the magnetic north by T_1-relaxation (see 2.1.6). From an energy accounting point of view, it *appears* as if all nuclei are in their eigenstates (Hanson 2008), and hence the nuclei (appear to) occupy the two energy states (spin up + and down -) according to the Boltzmann distribution

$$\frac{n_+}{n_-} = \exp\left(\frac{\Delta E}{kT}\right), \tag{2.1}$$

where ΔE is the energy difference between the spin up and down energy state, k is Boltzmann's constant ($=1.38\cdot10^{-23}$ J/K), T is the absolute temperature in Kelvin and n the number of spins in a given state. Since the energy difference between the two states is very small, thermal energy alone causes the two states to be almost equally populated. The energy difference is dependent on the strength of the magnetic field and the type of nucleus:

$$\Delta E = h\frac{\gamma}{2\pi}B_0, \tag{2.2}$$

where h is Planck's constant ($=6.63\cdot10^{-34}$ Js), γ is the gyromagnetic ratio ($\gamma/2\pi = 42.6$ MHz/T for protons) and is related to the strength of the magnetic moment for the type of nucleus considered. The remaining population difference results in a small net bulk magnetization aligned parallel to B_0. The population difference is approximately one part in 10^5 for B_0=3 T. The magnetization that is detectable by MR techniques is the net magnetization of the spins M, i.e. the macroscopic dipole density.
The individual magnetic moments do not align exactly parallel to B_0, but precess around the axis of B_0 at an angle, due to interaction between the

magnetic moment and the B_0-field. The net magnetization shows the same behavior and its time evolution is given by:

$$\frac{d\mathbf{M}}{dt} = \gamma \cdot \mathbf{M} \times \mathbf{B}_0 . \tag{2.3}$$

The precession frequency is proportional to the strength of the magnetic field and the strength of the magnetic moment for the type of nucleus considered. This frequency f_L is called the Larmor frequency:

$$f_L = \frac{\gamma}{2\pi} B_0 . \tag{2.4}$$

2.1.3 Radiofrequency Pulses

Irradiation of an ensemble of spins in an external magnetic field with radio-frequency (RF) pulses at the Larmor frequency induces transitions between the two energy levels. RF energy at other frequencies has no effect. The RF-pulse can be considered as a rotating magnetic field B_1 perpendicular to B_0. The B_1 field exerts a torque on the net magnetization, causing a rotation around the x- or y-axis. This creates a transverse component M_{xy}, which precesses around B_0 with f_L. The RF field causes the magnetic moments to precess in phase around the static magnetic field at their individual Larmor frequencies. If the RF-pulse is on for only a short period of time, the net magnetization is rotated by a certain angle away from the longitudinal axis; this angle is called the flip angle. The flip angle is proportional to the duration of the RF pulse τ and the amplitude of the RF-pulse, B_1:

$$\alpha = \gamma B_1 \tau \tag{2.5}$$

The precessing transverse magnetization induces an Electric Magnetic Force of frequency f_L in the receiver coil: the free induction decay (FID). When the flip angle is 90°, a maximum signal will be detected.

2.1.4 Field gradients

A magnetic field gradient is a spatial variation of the strength of the B_0 field. If there exists a constant gradient along one spatial axis, the

Larmor frequencies of protons will vary according to their positions along the gradient direction. This is the key to the understanding of MR localization and image formation. Since the imposed spatial variation of B_0 is known, the positions of resonating protons can be determined from their frequencies. The frequencies are calculated from the FID signal by Fourier transformation. RF pulses containing a narrow range of frequencies (RF bandwidth) excite only a slice of spins along the axis, orthogonal to the gradient, whose resonance frequencies correspond to the frequencies present in the RF (see next section). Gradients are also used to dephase MR signals by destroying the phase coherence of the individual spins. This is called gradient 'spoiling'.
When transverse magnetization is present, the magnetic field gradient causes transverse magnetization to precess at a frequency, which is proportional to a position along the gradient axis according to:

$$f = \frac{\gamma}{2\pi}(B_0 + r \cdot G_r), \tag{2.6}$$

where r is the distance to the position, where $f=f_L$, along the direction of the gradient G_r. The presence of a gradient has no significant effect on longitudinal magnetization.

2.1.5 Slice selective pulses

The excitation spectrum of an RF pulse of length τ extends over a frequency range in the order of τ^{-1} centered on the carrier frequency f_{RF}. This range of frequencies is called the bandwidth Δf. The pulse excites all resonances with offset frequencies within its bandwidth. An RF pulse is said to be nonselective or "hard" if the bandwidth is much larger than the frequencies in the sample. Strictly speaking such pulses are not available on clinical MR scanners. Instead "soft" pulses with a duration of milliseconds are used. Shorter pulses are typically called hard pulses though they are somewhat slice selective. In the presence of a gradient and if the flip angle is small such pulses excite a slice that corresponds approximately to the Fourier transform of the pulse shape. During the pulse the transverse magnetization is dephased and has to be refocused by the inverted slice gradient of half the pulse duration.
The slice profile is given by the Fourier transform of the RF pulse. An approximately rectangular slice profile can be produced by a so-called sinc pulse ($\operatorname{sinc} x = (\sin x)/x$), which is the (inverse) Fourier transform

of a rectangular profile. Such a selective pulse gives a relatively well-defined selected volume for the case of small flip angles. But there are large deviations between the profile of the excited magnetization and the Fourier transform when the flip angle is increased, especially for a 180° pulse. The shape of the selective pulses will determine the distribution of flip angles in the volume. A volume should be understood as a local weighting of the echo by the pulse profiles. The sharpness at the border depends on the design of the pulses.

2.1.6 Longitudinal relaxation

Resonant RF pulses induce transitions between the nuclear energy levels and change the populations of the different states. The original equilibrium population is then restored by so-called longitudinal relaxation, a process where the magnetic nuclei transfer energy to the environment (the lattice) by radiationless transitions between the energy levels. The longitudinal magnetization difference $M_{z,0} - M_z$ decays exponentially with a time constant T_1, the longitudinal relaxation time, given by

$$M_0 - M_z = (M_0 - M_{z,t=0}) \cdot \exp\left(-\frac{t}{T_1}\right), \tag{2.7}$$

where $M_{z,t=0}$ is the longitudinal magnetization immediately after the pulse and M_0 is the equilibrium magnetization in the z-direction.

Relaxation can be caused by several different mechanisms, but for protons only the magnetic dipole-dipole interaction between different protons are of importance. The dipole-dipole interaction between two protons depends on the distance between them and on the orientation of the internuclear vector relative to the external magnetic field and the orientation of the spins. The random tumbling of the molecules in a liquid (Brownian motion) makes the dipole-dipole interaction time dependent and gives rise to transitions between the nuclear energy levels. This property makes the longitudinal relaxation time depend on the substance.

2.1.7 Transversal relaxation

The transversal decay time T_2 is a measure of the loss of net magnetization in the transverse plane. This process can be described as dephasing of the individual nuclear magnetic moments. After a spin system has been excited by an RF pulse, all microscopic components precess in phase around B_0 and dephasing will eventually lead to complete cancellation of the signal. The relationship describing the decay of the transverse magnetization is:

$$M_{xy} = M_{xy,0} \exp\left(-\frac{t}{T_2}\right), \tag{2.8}$$

where $M_{xy,0}$ is the initial transverse magnetization after the pulse and M_{xy} is the transverse magnetization after time t.

The same mechanisms that are active in longitudinal relaxation also contribute to T_2-relaxation. In addition, transversal relaxation is also caused by molecular magnetic fields, which change the local magnetic field experienced by the nucleus causing the frequency of precession to vary. This causes a loss of phase. Another effect that gives rise to the loss of phase is an exchange of the spin state between two nuclei with no net loss of energy from the spin system, but with a loss of phase information. Transversal relaxation times are always shorter than longitudinal relaxation times. For pure water the so-called extreme narrowing condition applies, where $T_1 \approx T_2$ whereas in tissues $T_1 >> T_2$ due to the binding of some water molecules to slowly reorienting macromolecules.

2.1.8 Local field inhomogeneity

Transversal relaxation as described above represents “true” loss of transverse magnetization, because it is caused by the random molecular tumbling which cannot be reversed. Another cause of dephasing is B_0 inhomogeneity: spins at different locations are not exposed to exactly the same B_0 field, which implies a range of Larmor frequencies. This dephasing can be reversed. An effective transversal relaxation time T_2^*

can be defined, which represents dephasing due to the combination of T_2 and inhomogeneities in the static magnetic field:

$$\frac{1}{T_2^*} = \frac{1}{T_2} + \gamma \Delta B_0 , \tag{2.9}$$

where ΔB_0 is the average difference between the magnetic field for different locations. It is the decay of magnetization with the time constant T_2^* that constitutes the free induction decay, FID. A short T_2^* indicates a fast dephasing, which corresponds to a wide spread of the resonance frequencies. This leads to a short FID and a broad absorption in the frequency domain.

2.1.9 The Fourier transform

The MR signal of frequency f_0 received by the receiver coil is preamplified and then demodulated with respect to the excitation carrier frequency f_r. This demodulation is performed by means of a mixer that essentially multiplies the MR signal from the preamplifier with a reference signal. The output is composed of two signals at frequencies f_r-f_0 (low) and f_r+f_0 (high). The high frequency is eliminated by a low-pass filter. The low-frequency signal can then be digitized by an ADC. Demodulation is performed with two references with a phase difference of 90°. This is called quadrature detection. By combining the signals arising from the two channels, denoting the frequency difference $2\pi \cdot (f_r$-$f_0)$ by ω', the response $s(t)$ of a spin system to a radio frequency pulse can be written as:

$$s(t) = M_0 \cdot \exp(i\omega' t) \cdot \exp\left(-\frac{t}{T_2}\right), \tag{2.10}$$

where M_0 is equilibrium magnetization in the z-direction. The transversal relaxation time should be replaced by T_2^* if the static magnetic field inhomogeneities are significant. The FID from the acquisition is a function in the time domain. The Fourier transform is used to represent the information in the FID in the frequency domain. The Fourier transform of the signal in equation (2.10) is given by

$$S(\omega) = \int_0^\infty s(t)\exp(-i\omega t)dt = M_0\left(\frac{T_2}{1+T_2^2\Delta\omega^2} + i\cdot\frac{T_2^2\Delta\omega}{1+T_2^2\Delta\omega^2}\right), \quad (2.11)$$

where $\Delta\omega = \omega' - \omega$. The real part is the absorption spectrum (a Lorentzian line at frequency $\omega' = \omega$, and the imaginary part is the dispersion spectrum, see figure 2.1. The full width at half maximum of the line (FWHM) depends on the decay rate of the transversal relaxation as

$$\text{FWHM} = \frac{1}{\pi T_2} \ . \quad (2.12)$$

If the signal has not decayed to zero, the FID will be truncated and the resonance after Fourier transformation will show oscillations on both sides of the line.

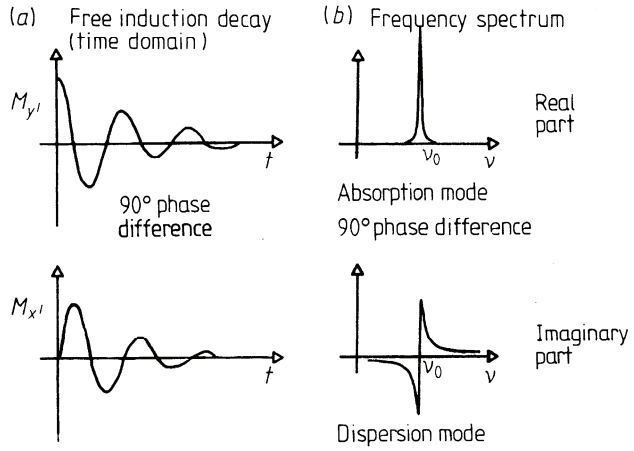

***Figure 2.1**: (a) The FID signals obtained by quadrature detection, and (b) the absorption and dispersion mode signals obtained after Fourier transformation.*

2.1.10 Spin-echoes

Dephasing in the transverse plane caused by B_0 inhomogeneities can be refocused by turning the spins 180° at time TE/2 after the initial 90° pulse. At echo time TE an echo forms. The 90° – 180° pulse sequence is called spin-echo sequence, see figure 2.2.

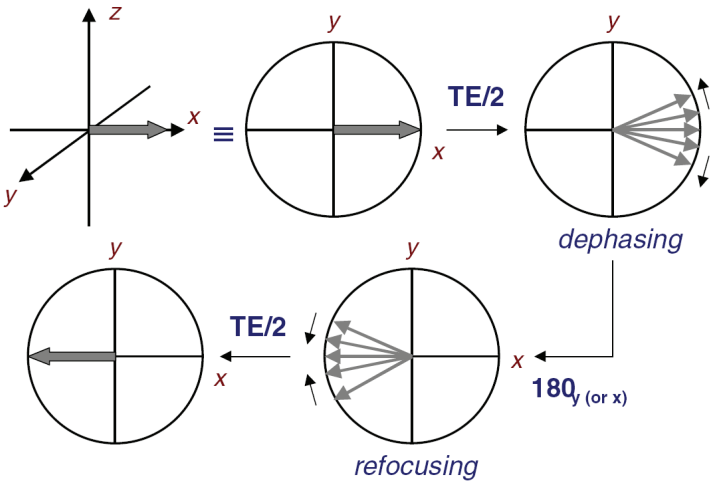

***Figure 2.2**: The principle of spin-echo with a 90 °– 180 ° pulse sequence.*

An echo can also be generated by 90° pulses (Hahn echo). The resulting echo recovers only 50 % of the initial magnetization. The other half is converted to longitudinal magnetization by the second 90° pulse. If a third 90° pulse is applied some time after the echo, these longitudinal components are returned to the transverse plane, where they refocus and give rise to a so-called stimulated echo. Transversal relaxation originates from random motion of the molecules and constitutes real, irreversible loss of coherence. It can not be refocused with a spin-echo or a stimulated echo.

2.1.11 Chemical Shift

In molecules, the nuclei experience slightly different magnetic fields due to their chemical environment. Each nucleus is surrounded by electrons, which reduce the magnetic field caused by the nucleus (shielding). This causes the resonance frequencies for different proton spins to be slightly different. This effect is called the chemical shift δ. The chemical shift is expressed in terms of the difference in resonance frequencies between the nucleus of interest f and a reference substance f_{ref}.

$$\delta = \frac{f - f_{\text{ref}}}{f_{\text{ref}}} \tag{2.13}$$

In proton MR spectroscopy tetramethylsilane (TMS) is used as a reference. The frequency difference is divided by the reference frequency so that the chemical shift becomes independent of the magnetic field used to measure it. Since chemical shifts are small, it is common to express them in parts per million (ppm), or alternatively the frequency difference in Hz (since the resonance frequencies are expressed in MHz).

2.2 In vivo MR Spectroscopy

2.2.1 The MR scanner

The B_0 field is generated by a superconducting horizontal, whole body magnet. The scanner used for the experiments was a Siemens Trio operating at 3 T. The magnet is fitted with a set of coils to optimize the magnetic field homogeneity (shimming). The B_1 field is generated by a digital frequency synthesizer set to yield RF-pulses at the proton Larmor frequency. Three sets of gradient coils create the magnetic field gradients in the *x*-, *y*- and *z*-directions. The maximum attainable gradient amplitude limits the minimum slice thickness and the maximum spatial resolution that can be used. In practice, gradients are not powered at all times, but are switched on and then off again (pulsed) at certain times during a pulse sequence. Switching gradients on and off induces eddy currents in the metallic structures of the magnet. The transverse magnetization induces an AC voltage in the RF coil used for reception, the resulting signal is approximately one billionth of the amplitude of the transmitted RF pulse. The signal is amplified by a factor 10^4 to 10^5 by an RF amplifier.

2.2.2 Metabolites of the brain

10-20 brain metabolites can be detected with MRS. Brain spectra have a good reproducibility. That is because of homeostasis, which refers to the mechanisms that provide for the stability of biological systems. It maintains the balance of energy production and consumption, and the stable ionic and osmotic equilibrium of living cells. The main metabolites of the brain that can be observed with proton MRS are

creatine and phosphocreatine, N-acetyl aspartate, choline containing compounds, myo-inositol, glutamate and glutamine. In addition, lactate can sometimes be observed. Changed concentrations of the metabolites from normal values are clear indications of pathology.
The selection of molecules that can be observed with MRS is limited to low molecular weight metabolites and must be present in sufficiently high concentration (approximately > 0.5 mmol/kg of wet weight or more).
A short presentation of the main metabolites of the brain follows below (Danielsen, 1999). It is important to state that each metabolite has its characteric field dependent spectrum and each metabolite (actually each resonance) has a specific transversal and longitudinal relaxation time.

Creatine and phosphocreatine
The sum of creatine (Cr) and phosphocreatine appears as the central peak in the proton brain spectrum as a singlet from the methyl group at 3.04 ppm and has another singlet from the methene group at 3.92 ppm. Phosphocreatine plays an essential role in the storage and fast supply of high-energy phosphate in organs that have to quickly engage in energy-consuming action such as muscle and brain. The sum of creatine and phosphocreatine is a reliable marker of intact energy metabolism.

N-acetyl-aspartate
NAA has an acetyl group which gives a singlet resonance at 2.02 ppm, and an aspartate group with coupled resonances (three doublets of doublets) centered around 2.49, 2.67 and 4.38 ppm. NAA is present in the brain at relatively high concentrations. The abundance of NAA and the presence of a prominent singlet resonance greatly facilitate MR observation in vivo. Brain NAA is believed to provide a marker of neuronal density and function.

Choline
The choline (Cho) signal is primarily observed as a prominent singlet at 3.24 ppm that includes contributions from free choline, glycerophosphorylcholine, and phosphorylcholine. Choline is an essential nutrient that is primarily obtained in the form of phospholipids from the diet. It is a precursor to acetylcholine and cell membrane components and a marker of cellular membrane turnover, and is therefore elevated in neoplasms, demyelination and gliosis.

Lactate
Lactate (Lac) appears as a doublet at 1.33 ppm. The lactate doublet can be masked by lipid resonances. Lactate is the product of anaerobic

glycolysis and thus an intermediate product of the energy metabolism. Lactate elevations are found in many diseases with failed oxidative metabolism, which is the case for many diseases of the brain. The normal lactate level in the brain is less than 1 mM and lactate can typically not be seen in the spectrum.

Myo-Inositol

Myo-inositol (MI) is a sugar alcohol whose structure is similar to that of glucose. It has a complicated spectral pattern that is explained by the asymmetric distribution of its six hydrogen atoms. The peaks are located at 3.27, 3.56 and 4.05 ppm. It is estimated that 70 % of the MI peak comes from free MI and 15 % from MI phosphate. MI may act as a marker of glial cell numbers, an osmoregulator, intracellular messenger, or detoxification agent in the brain as well as in the liver.

Glutamate and glutamine

Glutamate (Glu) has two methylene groups and a methine group that are strongly coupled, which gives rise to a complicated spectral pattern spread between 2.0 and 3.8 ppm, resulting in low intensities of individual peaks despite its relative abundance. Glutamate is the most abundant amino acid found in the brain. It is known to act as an excitatory neurotransmitter.

The amino acid glutamine (Gln) is a storage form of glutamate. Glutamine is structurally similar to glutamate with two methylene groups and a methine group, and its spectrum is very similar to Glutamate, and so it is difficult to distinguish these two. Therefore glutamate and glutamine are often combined and referred to as “Glx”.

Lipids

Lipids cause two broad peaks at 1.3 and 0.9 ppm. Since the concentration of lipid is much higher than the concentration of the metabolites, the signal can be very high and deteriorate the spectrum around between 0.8 and 1.5 ppm, are even makes it impossible to identify most common metabolites such as NAA and Cr. Therefore it is important to place the volume to be measured far away from lipids. Since the signal is very high compared to the metabolite signals it is also spatially spread out. If lipid signal is a problem, areas with lipid can be suppressed by saturation slabs that locally spoil the complete MR-signal effectively removing the contribution of the lipid signal to other areas.

2.2.3 Single Voxel Spectroscopy

Single voxel MRS makes it possible to measure MR signals originating only from a specific region of the brain, the so-called volume of interest (VOI). By combining three orthogonal gradients with three pulses, the VOI is defined at the intersection of the three slices. The first pulse, applied in the presence of a gradient, creates a slice of transverse magnetization through the object, perpendicular to the gradient axis. With the second pulse, another slice is excited with help from a gradient, orthogonal to the first one. A rod is created from the spin echo at the intersection of the two slices. The third pulse and gradient creates a third slice orthogonal to the first two. The echo comes from the cubic volume at the intersection of the three slices. Spoiler gradients destroy FID signal in the three slices and the spin echoes in the rods outside of the VOI.
To choose the localization of the VOI or voxel, MR images of the object are acquired. From the MR images, the voxel can be selected. Offset frequency and gradient strengths are automatically calculated to get the desired volume size and location, see figure 3.1.

2.2.4 STEAM and PRESS

Two pulse sequences that are used for single volume MRS are STEAM (Frahm, 1987) (stimulated echo acquisition mode) and PRESS (Bottomley, 1987) (point-resolved spectroscopy). STEAM selects a stimulated echo from the pulse sequence 90° – TE/2 – 90° – TM – 90° – TE/2 – ”ECHO”, where TE is the echo time and TM is the mixing time. PRESS creates a double spin echo from the pulse sequence 90° – TE1/2 – 180° – TE1/2 – TE2/2 – 180° – TE2/2 – ”ECHO”, where TE =TE1 + TE2. See figure 2.3 for an illustration (Nilsson 2002) of the two pulse sequences.
The choice of STEAM and PRESS affects the appearance of the spectra. In theory PRESS gives a factor two larger signal size than STEAM given the same echo time. The STEAM sequence is less sensitive to T_2-relaxation effects since no T_2-relaxation occurs during the mixing time while PRESS is sensitive to T_2-relaxation throughout the localization sequence. STEAM has two echo intervals, while PRESS has four. With the same hardware, shorter TEs can therefore be achieved with STEAM than with PRESS.

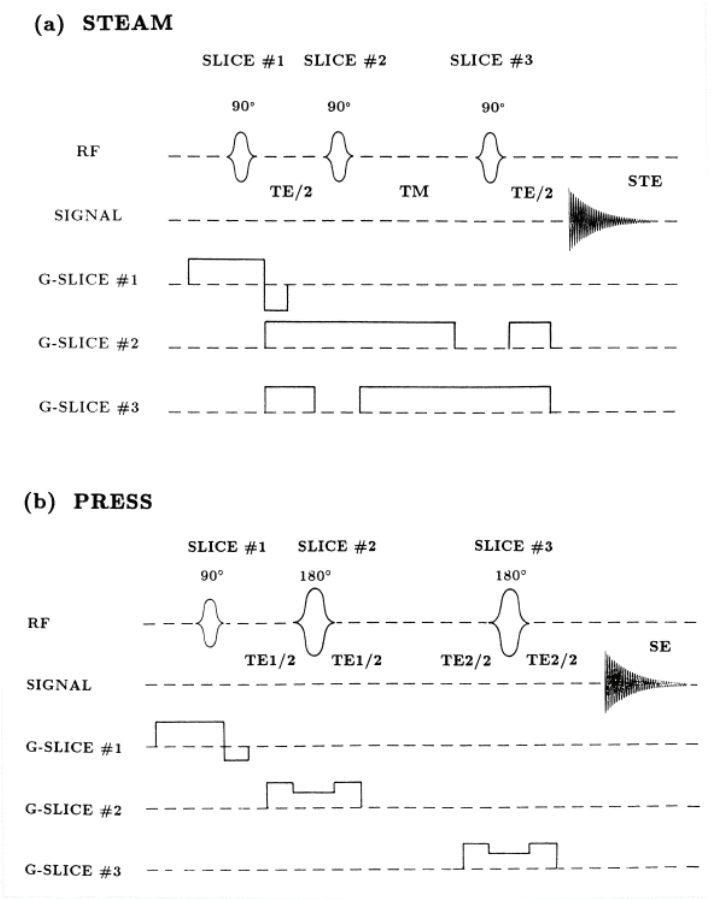

***Figure 2.3**: Scheme of (a) STEAM and (b) PRESS of pulse sequences.*

With short TE, shorter RF pulses with less selective slice profiles and shorter gradient crusher pulses with lower spoiling power have to be used. This may lead to more signal contamination from outer volume signal. On standard clinical systems, STEAM and PRESS sequences with TE from 20-30 ms can be used without too big a compromise with respect to outer volume contamination.

Shorter TE gives rise to smaller T_2 losses and therefore better SNR because of the T_2 relaxation at long TE. Some resonances ”disappear” more slowly than others, depending on different T_2-relaxation, which gives rise to different peak ratios at different TEs. Some of the clinically important metabolites with strong coupling can only be seen with short echo times. With longer TE the spectra are easier to interpret due to fewer peaks and less overlap, at the expense of signal loss. Of the previously mentioned metabolites creatine, NAA, choline and lactate can

be measured with long echo time (>70 ms), while the other metabolites need to be measured with a short echo time of 30 ms or less. However, lipid can also be visible in long echo time spectra, due its high intensity. The repetition time TR of the pulse sequence should typically be at least of the order of the highest T_1 of the substance to be measured.

2.2.5 Parameters affecting the quality of the spectra

Sampling

The computer samples the FID signal with constant intervals Δt between two consecutive data points. Δt is called the dwell time. The voltage is converted into numerical form using an analog-to-digital converter (ADC). The MR signal contains many components oscillating at different frequencies. In order to fully represent all components, the sampling rate of the ADC must be sufficiently high; i.e. the dwell time must not be too long. For obtaining a well-defined frequency from a discrete Fourier transformation, a real valued sinusoid must be sampled at least two points per period. This means the highest measurable frequency, called the Nyquist frequency, is half the sample frequency. The width of this frequency window is equal to the sample frequency (including negative frequencies) is called the spectral width. If the sampling rate is too low, then the signal components with frequencies above the Nyquist frequency still appear within the frequency window of the MR spectrum, but are "folded" around the Nyquist frequency.

Digital resolution

The digital resolution is the spectral width (Hertz) divided by the data size (points). In the frequency domain, the digital resolution is given by the frequency interval between two consecutive points. Zero filling may be performed to improve the digital resolution without increasing the acquisition time. After the acquired FID zeroes are added before Fourier transformation. This is valid as long as the FID has decayed to a quasi-zero value, and this corresponds to sinc-interpolation of the spectrum.

Phase corrections

The FID has an arbitrary phase. This is called zero order phase error and is frequency independent. It can be corrected with an inclusion of a factor $\exp(i\varphi_0)$ in the equation of the signal. Phase error of first order, which is when the phase factor increases linearly with the frequency, can

easiest be understood by a time delay between the excitation and beginning of the data acquisition.
When the gradients are switched on and off, electrical currents, called eddy currents, are induced into materials constituting the probe and the magnet. These currents create a magnetic field that varies in time and space, and in turn perturb the detection of the MR signals. Eddy currents can cause artifacts in images and may seriously degrade overall magnet performance. In the context of MR spectroscopy, eddy currents cause a non-linear evolution of the signal phase. This may lead to severe distortion of all the lineshapes in the spectra.
Eddy currents cannot be corrected by ordinary phase correction of zero and first order. Reference scans without water suppression but with otherwise identical acquisition parameters can be used for eddy current correction (Klose 1990, Drost 2002). The phase behavior of the water resonance due to eddy currents is measured and used to correct the signal of all the resonances in the spectra.

Signal to noise ratio
Since the signal intensities of the metabolites are very low compared to the water signal the acquisition needs to be repeated several times in order to get a satisfactory signal-to-noise-ratio (SNR). The signal-to-noise ratio (SNR) of a resonance is defined as the relation between the peak height and the standard deviation of the noise. The signal is proportional to the number of scans. In the case of white and constant noise the SNR is proportional to the square root of the number of scans. To get twice the SNR it is necessary to perform four times as many scans. The volume of interest also affects signal size. A small VOI needs more scans to get a good SNR.

Shimming
Shimming is performed to increase the homogeneity of the B_0 field. The field within the volume of interest (VOI) can be optimized by adjusting the currents in auxiliary shim coils. If the field is homogeneous the peaks in the spectrum are taller and narrower. That is because inhomogeneities make identical protons resonate at slightly different frequencies and the peaks become wider and lower. An adjustment of the frequency has to be done after the shimming, because it changes the magnetic field and hence the frequency. A smaller VOI is easier to shim than a larger one. However, the signal strength is proportional to the size of the VOI and an appropriate volume has to be a compromise from those factors.

Water suppression

The concentration of water in the brain is about 10,000 times higher than the metabolites of interest and the water signal dominates the spectrum. The water signal causes a sloping baseline that may hide the metabolite resonances. In addition, it causes artifacts in the spectrum that may be about the same size as the metabolite signals. Therefore, it is desirable to suppress the water signal. Water suppression has to be done during the acquisition of spectra, and cannot be applied afterwards because the artifacts cannot be erased by post-processing methods. The water is suppressed by an RF-pulse (actually 3) designed to excite only a narrow frequency band, centered around the water peak frequency without affecting the metabolite signals. The bandwidth used in this study was 60 Hz, corresponding to approximately 0.5 ppm. The RF pulse tips the water magnetization into the transverse plane and then the water magnetization is dephased by a crusher gradient pulse.

CHAPTER 3

Motion correction in MR Spectroscopy

In this chapter the problem of motion during consecutive single voxel spectroscopy acquisitions is addressed. In Single Voxel Spectroscopy (SVS) the acquisition of the spectrum is typically repeated n times and then combined in order to improve the Signal-to-Noise Ratio (SNR) with a factor $\sqrt{n}$. In practice the acquisitions are not only affected by random noise, but also by physiological motion and subject movements. Since the influence of physiological motion such as cardiac and respiratory motion on the data is limited, it can be compensated for without data-loss. Individual acquisitions hampered by subject movements on the other hand need to be rejected, if no correction or compensation is possible. If the individual acquisitions are stored, it is possible to identify and reject the motion-disturbed acquisitions before averaging.

Several automatic algorithms were investigated using a dataset of spectra from non-anesthetized infants with a gestational age of 40 weeks. Median filtering removed most subject movement artifacts, but at the cost of increased sensitivity to random noise. Neither Independent Component Analysis (ICA) nor outlier identification with multiple comparisons has this problem. These two algorithms are novel in this context. The peak height values of the metabolites were increased compared to the mean of all acquisitions for both methods, although primarily for the ICA method.

3.1 The problem of motion

Subject movement during consecutive Single Voxel Spectroscopy (SVS) acquisitions is often not detected and the resulting distorted data affects the outcome measures. Since severe patient movements, as present for instance in SVS of non-anesthetized pediatric patients, psychiatric and demented patients, cause significant deterioration in spectra, they should not be ignored. For example, movements may introduce a bias in a comparative study between patients and healthy controls. Despite its significance, the issue of identifying motion-distorted spectra, in contrast to motion correction and compensation, is quite unexplored and often not mentioned, see e.g. Drost (2002) and Jansen (2006).

Compensation for spectra that are potentially affected by physiological motion can be performed by cardiac and respiratory gating (Felbinger 1998) and/or breath holding techniques (Katz-Brull 2003). Since disturbances in phase and frequency by physiological motion are limited (Katz-Brull 2004), they can be compensated for by phase correcting the individual acquisitions before averaging, a process known as phase coherent or constructive averaging (Zhu, 1992), followed by frequency shift correction (Helms 2001, Bolan 2004). However these techniques can potentially introduce a bias caused by differences in noise between subjects. A bias towards increased phase reference signals may also result.

Severe patient movement cannot be compensated for and the acquisitions distorted by patient motion need to be identified and rejected. Motion can be tracked by a water-signal-based navigator (Shanbhag 2005), or an interleaved navigator scan (Thiel 2002). Especially J-difference editing is sensitive to motion artifacts and it was shown that the interleaved navigator scan is sufficient (Bhattacharyya 2007).

However, a navigator scan is not necessarily needed since the single voxel spectra of the consecutive acquisitions reveal information of the subject's movement. The motion-distorted acquisitions seem easy to identify visually, but commonly used “objective” rejection criteria are typically based on the position, amplitude and width of the suppressed water peak and an arbitrary threshold (Pfeuffer 2004). Alternatively a cluster analysis of the lipid signals can be used to correct for subject motion (Skimminge 2003), but a lipid signal might not always be present.

In practice, motion correction consists of two steps. First the acquisitions severely deteriorated by subject movements need to be identified and

excluded. Second the remaining acquisitions need to be frequency-shifted and phase-corrected individually (Pfeuffer 2004).
Movements during an individual acquisition, and severe movements between acquisitions, may corrupt the entire spectrum of the acquisition irreversibly. Limited movement between individual acquisitions will introduce a simultaneous broadening and lowering of the peak in the mean spectrum but keeping the area under the peak approximately constant. This can affect the output of the fitting procedure, if peak shapes are assumed. Movement can also result in a different location of the measured volume, which additionally can cause an error in metabolite concentrations if these vary with position. There can be a difference between the group of patients and the healthy controls regarding unrecoverable subject movements. The patient data might suffer more from subject movements, and if no movement compensation is performed, this will cause a systematic underestimation of metabolites in this group and thus introduce a bias in the study (Helms 2001).
Corrections primarily have to ensure robust positioning of the measured volume while keeping the signal free of motion-induced bias, and secondarily keeping the noise low and the Signal-to-Noise Ratio (SNR) as high as possible. SNR is typically increased compared to conventional averaging by phase-coherent averaging (Gabr 2006) and also potentially by outlier rejection techniques due to the unwanted contributions to the motion-distorted signal.
Here, subject movement is demonstrated to be a severe problem for non-anesthetized infants. Several algorithms for identifying and rejecting motion-corrupted spectra were proposed, implemented and compared to existing methods.

3.2 Subjects and data acquisition

Subjects were infants born at the Copenhagen University Hospital, Hvidovre, Denmark, and taking part in a MRI/MRS-preterm infant cohort study. The study includes data from 97 infants; 77 preterm infants (prematurely born between 12 and 6 weeks before term) and 20 controls (born at term). All infants were MR-scanned around term or term-equivalent age, and were not anesthetized before or during scanning. The local ethics committee accepted the study and informed parental consent was obtained in all cases.
MR scanning was performed on a Magnetom Trio 3 tesla scanner (Siemens, Erlangen, Germany) with a quadrature single channel head coil. An 8 mL cubic voxel was placed in the posterior periventricular

white matter, by the posterior horn of the lateral ventricles, and a 3.4 mL cubic voxel was placed at the level of the basal ganglia and thalami, both randomly positioned in the right or left hemisphere. For each voxel position 48 Free Induction Decay signals (FIDs) based on two phase-cycled averages, each with 1024 complex points and a readout period of 850 ms, were acquired with a Point RESsolved Spectroscopy (PRESS) sequence (Bottomley 1987) for two echo times (30 and 144 ms) with a repetition time of 2 seconds.
For every subject, four datasets of 48 repetitions each were acquired for the two different voxels and the two echo times. In order to investigate the effect of subject movement under more controlled conditions, a healthy volunteer was scanned with the same sequences with 30 ms echo time and same position and size of the 8 mL cubic voxel. The 48 acquisitions were repeated three times for the volunteer. The volunteer was instructed to lie motionless during the acquisition of the first dataset and instructed through the intercom to move his head a few centimeters to the left and right for a few seconds approximately at every 16th acquisition of the last two datasets.

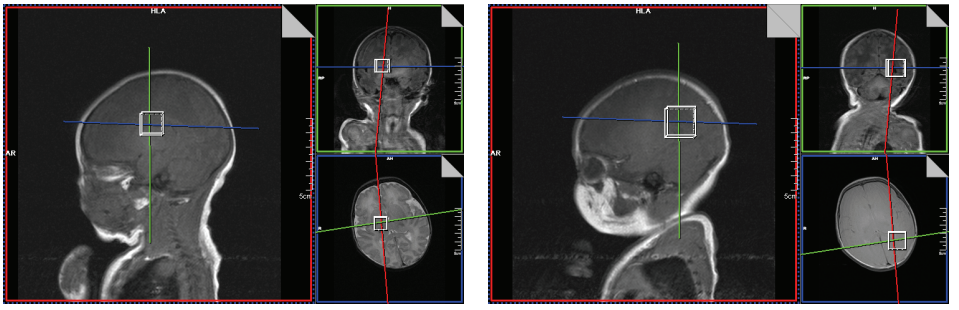

Figure 3.1: *The placement of the two voxels on an MR-image.*

Datasets where all 48 repetitions contained severely corrupted measurements, or where water suppression failed, were excluded from this comparative study after visual inspection of the spectrogram. This resulted in 130 datasets (64 with long echo time) for an 8 mL voxel and 113 datasets (56 with long echo time) for a 3.4 mL voxel. From the 130 datasets with an 8 mL voxel and from the 113 datasets with a 3.4 mL voxelsize, 30 and 26 datasets respectively originated from term infants. The resulting mean or median spectra are zero-order phase-corrected and filtered with a first order Gaussian low pass filter with a full width at half maximum of 1 Hz. Spectra were frequency adjusted based on the position of the N-acetyl aspartate (NAA), creatine (Cr) and choline (Cho)

peak, at 2.02 ppm, 3.04 ppm and 3.24 ppm, respectively. Phase-coherent averaging was not applied.
Since the motion-distorted acquisitions are visible as shifts in the frequency domain, it is natural to perform the motion rejection in this domain. It is also possible to carry out the analysis on the Free Induction Decay (FID) signal in the time domain (Slotboom 2007), but this has not been done in this study.
The performance of three classes of subject-movement-rejection algorithms was investigated: 1. Simple median filtering, which provides a more robust but more noise sensitive estimate than mean filtering. 2. An outlier identification (OI) algorithm with and without multiple comparisons. 3. Independent Component Analysis (ICA), where the main component represents the spectrum least affected by motion. Corrections as described in the introduction (Zhu 1992, Helms 2001, Thiel 2002, Gabr 2006) were not performed. Focus was on identification and rejection of the corrupted acquisitions within a dataset.

3.3 Outlier detection

3.3.1 Mean and median filtering

In the conventional way of data processing all spectra are averaged permitting motion distorted acquisitions to degrade the final spectrum. One way of dealing with this problem is to reduce the influence of outliers by median filtering (Slotboom 2005, 2007a). Instead of the mean, the median is used, which provides a more robust estimate. However, this has two drawbacks.
The mean minimizes the expectation value of the squared deviation, i.e. the variance, while the median minimizes the expectation value of the absolute deviation. This means that the influence of outliers in the median is reduced but not cancelled. This can be illustrated by the influence of one sample x_i on a normal distributed data set with n samples, mean $\bar{x}$ and standard deviation σ. The mean $\bar{x}$ is shifted by

$$\Delta\bar{x}_i = \frac{x_i - \bar{x}}{n} \equiv \frac{\Delta x_i}{n}. \tag{3.1}$$

The influence of outliers on the mean is reduced by a large amount of samples and depends on the value of the outlier.

For a large number of samples *n* and a continuous probability function *p(x)* the shift in the median $\tilde{x}$ caused by one sample can be approximated by half the uniform bin width *w*, where the center bin contains one sample. The shift in the median is then given by

$$\Delta\tilde{x}_i \approx \frac{w}{2} = \frac{1}{2 \cdot n \cdot p(\tilde{x})}, \tag{3.2}$$

and shifted in the opposite direction for samples with a value lower than the median. Alternatively equation (3.2) can be derived by the analysis of the influence of one sample on the cumulative distribution, see Appendix A.1.

It is an appealing property of the median that the shift does not depend on the value of the outlier; only the position of the median in the list of ordered samples is shifted half a position. In the case of an even number of outliers symmetrically spread around the true mean value the shift is even cancelled.

The noise *N* of the mean with standard deviation of the population σ is given by

$$N^2_{\text{mean}} = \text{var}(\bar{x}) = \sum_i (\Delta\bar{x}_i)^2 = \frac{<(\Delta x)^2>}{n} = \frac{\sigma^2}{n}, \tag{3.4}$$

and the noise in the median is given by

$$N^2_{\text{median}} = \text{var}(\tilde{x}) = \sum_i (\Delta\tilde{x}_i)^2 \approx \frac{1}{4 \cdot n \cdot p^2(\tilde{x})} = \alpha \cdot N^2_{\text{mean}}. \tag{3.5}$$

The approximation of the noise for the median holds for large sample sizes with an arbitrary probability function *p(x)* consistent with the literature (Slotboom 2006, Rider 1960, Kenney 1962). The constant α is called the relative efficiency of the mean compared to the median and is $\pi/2$ for normal distributions and 3 for uniform distributions.

For normal distributions the random noise in the median is approximately 25% higher than for the mean. For a uniform distribution the random noise is 73% higher in the median compared to the mean. The probability function of the median is normally distributed for any probability function of the samples. The median as an estimator is more sensitive to noise, and therefore it is expected to be better to identify the outliers, reject them, and calculate the mean of the remaining data.

Median filtering (together with minimum and maximum filtering) is a well-known type of order-statistics filtering (Kenney 1962). A combination of order-statistics filters as All-Rank Selection Order-Statistics filtering (Barner 1998) might reduce noise and outlier sensitivity compared to median-filtering, but this has not been shown. Since spectra are complex the average and the median of both the real and imaginary part were calculated separately.

3.3.2 Mean or Median?

A method to determine whether to use the mean or the median is to look at the difference between these two. For symmetrical probability distributions such as the normal and the uniform distribution the expection value of the mean and median are identical and the expectation value for the difference between these two is zero. In practice the calculated difference can be compared with the expected squared difference. Because the median and mean are strongly correlated, the variance is not just the sum of the variances. For large n and distributions, where mean and median have the same expectation value, the expectation value of the squared difference between mean and median can be approximated, see Appendix A.2, with

$$< (\bar{x} - \tilde{x})^2 > \approx \frac{1}{n} \cdot \left(\mathrm{var}(x) + \frac{1}{4p^2(\tilde{x})} - \frac{< |x| >}{p(\tilde{x})} \right) = \beta \cdot \mathrm{var}(\bar{x}) , \qquad (3.6)$$

where β is a constant related to the efficiency α. For normal distributions β is $\pi/2 - 1 \approx 0.57$ and for uniform distributions β is equal to unity. So the expectation value of the difference between mean and median is of the order of the variance of the mean for normal and uniform distributions without outliers.

3.3.3 Outlier identification (OI)

Outliers can be identified and excluded by an approximation of the standard deviation and a t-test. Performing this outlier identification and rejection for every single frequency (pointwise outlier identification) will reduce the contribution of outliers. In this context, a novel alternative is to reject a whole acquisition, if only one Fourier component is identified

as an outlier (outlier identification). It is assumed that the acquisitions without outliers are normally distributed. The significance level p for the first method was arbitrarily chosen at 5% double sided, i.e. z_{max}=1.96, where z is the z-score, which is defined by the difference from the mean measured in the number of standard deviations. The significance level for the second method is corrected for multiple comparisons and this was arbitrarily chosen at 10% (double sided) divided by the number of data points (=1024) for one acquisition, i.e. z_{max}=3.9. Since the outliers were included in the calculation of the standard deviation, the procedure needs to be repeated in an iterative fashion. The first (crude) estimation of the outlier-free signal is given by the mean and the standard deviation of all samples x_i. The next estimates, denoted x^* with iteration number j are calculated in an iterative fashion as in Thomsen (2008) with

$$x^*_{j+1} = \bar{x} \text{ and } \sigma^2_{j+1} = \overline{(x^*_{j+1} - x_i)^2}$$
$$\text{for all } x_i \text{ with } |x_i - x^*_j| < z_{max} \cdot \sigma_j \ , \qquad (3.7)$$

until convergence is reached. An iterative t-test has apparently never been applied before in this context, but the idea behind the method is similar to the iterative f-test algorithm described by Andersson (1977).

3.3.4 Independent Component Analysis (ICA)

Independent Component Analysis (ICA) supplies a mathematical framework for analysis of a group of acquisitions. The method (Bell 1995) is implemented as a toolbox[1] (Højen-Sørensen 2001, Maximum likelihood (Infomax), icaML) in Matlab (Mathworks, Natick, Massachusetts). ICA is a set of methods for blind signal separation sharing the assumption that two arbitrary components s_1 and s_2 with probability functions $p(s_1)$ and $p(s_2)$ are assumed statistically independent (Hyvärinen 2000), defined by

$$p(s_1, s_2) = p(s_1) \cdot p(s_2) \text{ and}$$
$$< f(s_1) \cdot g(s_2) > = < f(s_1) > \cdot < g(s_2) > \qquad (3.8)$$

[1] Kolenda T, Sigurdsson S, Winther O, Hansen LK, Larsen J. DTU:Toolbox, Intelligent Signal Processing group at the Institute of Informatics and Mathematical Modelling at the Technical University of Denmark, 2002, http://isp.imm.dtu.dk/toolbox/

for any function *f* and *g*. Blind signal separation refers to the common situation in signal processing in which we aim to separate unknown source signals from an unknown mixture. This happens, for example, in the so-called "cocktail party" problem where the target is to separate a number of simultaneous speakers based on one or more microphone measurements. Another way of describing or defining ICA is by minimizing the mutual information between the components.
With index *i* denoting the acquisition number, and the index *j* denoting the component number, the dataset consisting of *n* acquisitions $x_i(t)$ is described by *M* components $s_j(t)$ with coefficients a_{ij} with

$$x_i(t) = \sum_{j=1}^{M} a_{ij} \cdot s_j(t) + \text{noise}. \tag{3.9}$$

Since the ICA algorithm only works for real signals, the complex spectrum is transformed into a real signal by adding the imaginary amplitude spectrum behind the real spectrum. An important complication that often arises in practical applications is that the number of components *M* is unknown. Using a Bayesian ICA formulation, this problem can be solved in the limit of many acquisitions (Kolenda 2001, Hansen 2001). The Bayesian Information Criterion (BIC) selects the number of components by estimating the probability of the model containing *M* components given the observed data *p*(*M*), where the number of components is varied in a range from 1 to $M_{\max}$ (the maximum number of components was arbitrary set to 12). The signal variance not accounted for by the *M* components is assumed to be contributed by an additive normal independent identically distributed white noise signal component (the BIC selection of the number of components is included in the toolbox (Højen-Sørensen 2001). Checks are performed to see if the probability for the number of components is less than 50%.
In the case of a dataset without distorted spectra, ICA will find one component representing the underlying spectrum. The difference between the spectra reconstructed with this component and the measured spectra equals the noise as identified by the ICA algorithm.
If the ICA algorithm finds more than one component, the independent component representing the undistorted spectrum needs to be identified, since ICA does not assign a clear meaning to its components. The dominant component of every single acquisition is determined and the acquisitions with the dominant component equal to the most frequent dominant component (the main component) for all acquisitions are considered to be a measurement of the undistorted spectrum. No

arbitrary thresholds need to be set. The ICA method produces three spectra: 1. the mean of the selected acquisitions, 2. the mean of the selected acquisitions reconstructed with *M* independent components and 3. the mean of the selected acquisitions reconstructed with only the main independent component. The latter spectrum corresponds to the scaled main independent component. The application of ICA and the identification of the non-distorted ICA component are novel in this context.

3.4 Noise and SNR analysis

In principle, noise can be estimated at one frequency by determining the standard deviation of the selected acquisitions and dividing by the square root of the number of acquisitions. Possibly only few acquisitions may be left, and this will make this noise estimation unreliable. However this is not a problem with the datasets used as completely corrupted data was excluded. Noise will be underestimated, however, since the standard deviation is minimized for the outlier identification methods. This is most prominent for the algorithm without connection between the Fourier components (the frequency direction). The ICA method does not have this problem, but the independent components have a lower noise than the original acquisitions. For ICA, the noise at each particular frequency can be determined by resampling with the JackKnife (Miller 1974) method, but in order to aid comparison an identical noise estimation procedure for all motion-rejection algorithms is preferred. Since there are no metabolite signals between 8 and 9 ppm, this part of the spectrum is used for estimating the noise. The standard deviation of the final signal is determined over this frequency range, which does not depend on the number of selected acquisitions. It is assumed that the signal is constant in this part of the spectrum and that the noise is independent of frequency.

For the Signal-to-Noise Ratio (SNR) and signal analysis, the signal is regarded as the peak height of the three main metabolite peaks, N-acetyl aspartate at 2.02 ppm, creatine at 3.04 ppm and choline at 3.24 ppm. Both mean peak height and average SNR of these three peaks were calculated for each dataset. In order to be able to compare between subjects, both signal and SNR were normalized by the values for the mean filtered signal. The algorithm with both the highest signal and highest SNR is considered as the optimal algorithm. Since position change is a source of erroneous measurements and causes simultaneous

broadening and lowering of peaks, the area under the metabolite peak is not a proper measure of the quality of the measurement.
Acceptance percentage for each algorithm and each dataset was defined by the number of single data points that were not rejected by the algorithm as a percentage of the total number of data points. The total number of data points equals the number of repetitions times the number of Fourier components.

3.5 Results

The first dataset of the healthy volunteer had 48 comparable spectra and the ICA algorithm found only one component, as is expected for a dataset without motion. The effect of (instructed) motion on the other two datasets of the volunteer was comparable. Figure 3.2 shows the spectrogram (top panel) and the coefficients for the components (bottom panel) of the second dataset, where the healthy volunteer was instructed to move his head at certain times. The influence of head movement is clearly seen in the spectrogram, and ICA components describe the different periods. A typical result for measurement of a preterm infant that has been hampered by motion is shown in figures 3.3 to 3.7. The top panel in figure 3.3 shows the spectrogram for short echo time, and the bottom panel shows the coefficients for the components in the ICA algorithm. Figures 3.4 and 3.5 show the final spectra between 2.8 and 3.5 ppm for all algorithms for an 8 mL voxel with short echo time (figure 3.4) and long echo time (figure 3.5). Figure 3.6 shows the entire short-echo-time spectrum. The noise is estimated from the signal between 8 and 9 ppm, since there are no metabolite signals there. Figure 3.7 shows the short-echo-time spectrum around the residual water peak and the removal of a water peak erroneously displaced by subject movement.
Both peak heights and SNR for the three main metabolite peaks behave comparably, so only the average signal and SNR for the three metabolite peaks are discussed, and referred to as “the signal” and “the SNR”. The SNR of the mean filtered spectra ranged from 8.4 to 54.3, and was highest for the 8 mL voxel with short echo time and lowest for the 3.4 mL voxel with long echo time. The SNR was (mean ± standard deviation) 29.9 ± 8.3 for the 8 mL voxel with short echo time and 15.1 ± 5.1 the 3.4 mL voxel with long echo time.

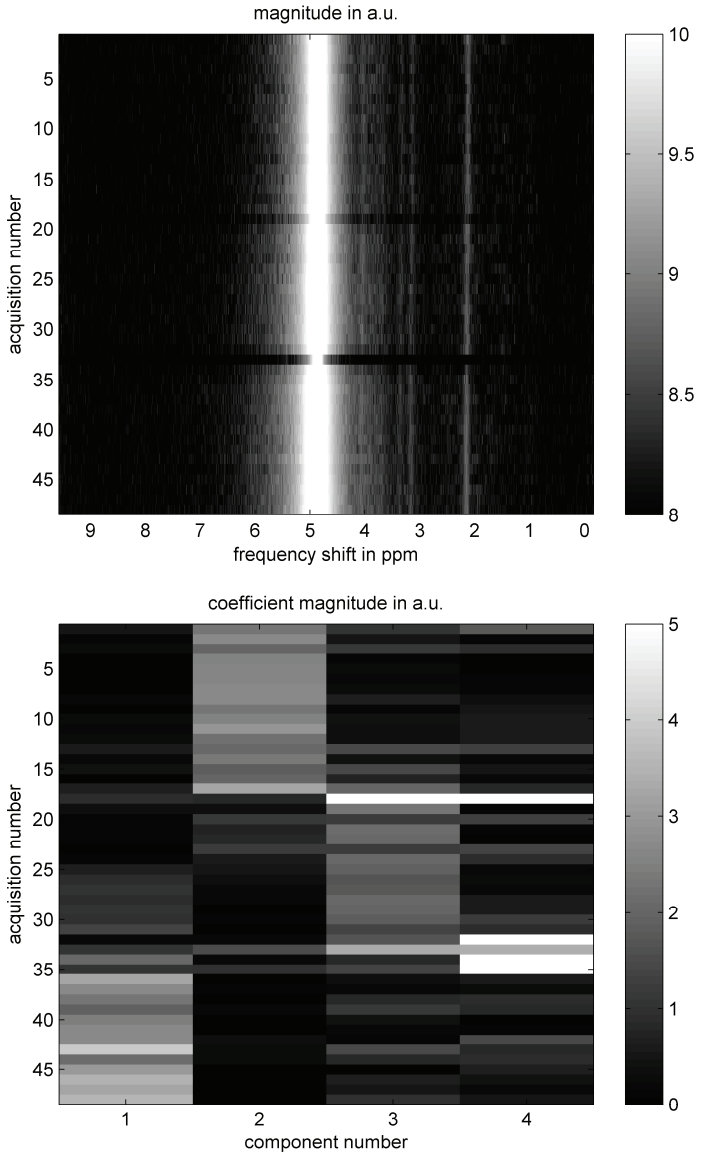

Figure 3.2: *The spectra of 48 acquisitions of an 8 mL voxel with an echo time of 30 ms for a healthy volunteer (top panel). The volunteer was instructed to move his head 2-3 cm continuously from the left to the right at acquisitions 18-19, and 32-34. Each spectrum is shown as a row using the grayscale for the log of the magnitude of the signal intensity in arbitrary units (a.u.). The residual water peak at 4.7 ppm is clearly visible, as are metabolite signals at the right hand side of the water peak. In the bottom panel, the coefficients for the ICA components for the spectra are shown. A grayscale is used to show the amplitude of the coefficients in a.u. The three periods without movement are mainly described by a single component for each period (component 2-3-1), while the spectra during head movement are described by a combination of all four components.*

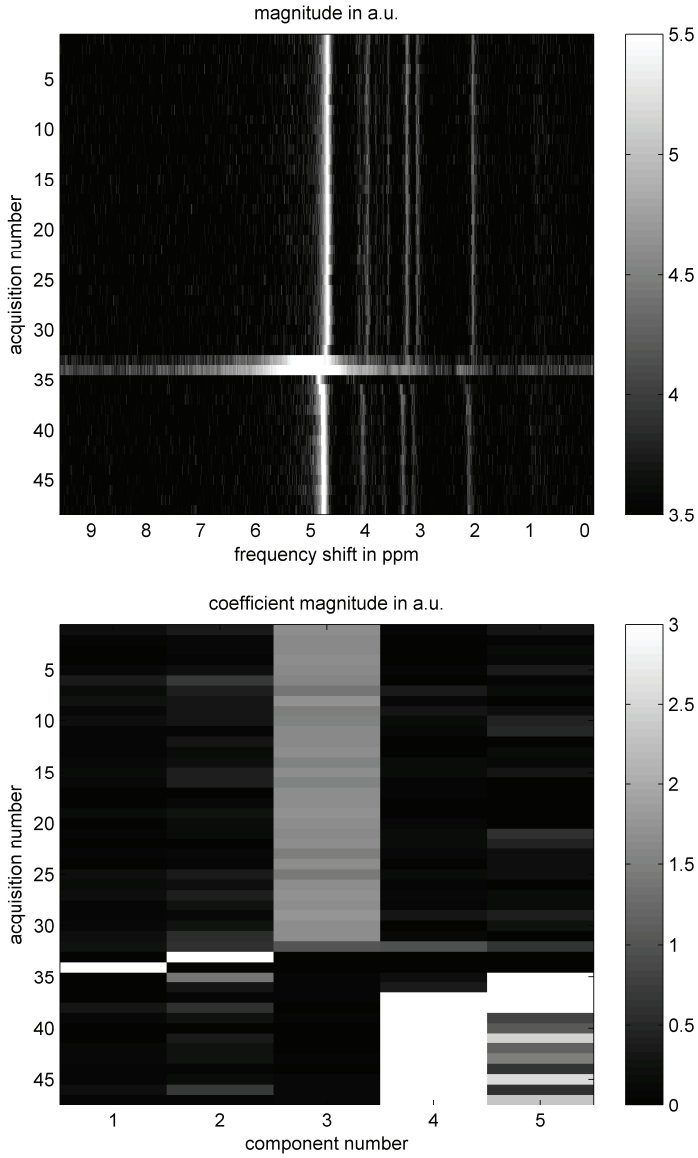

Figure 3.3: *The spectra of 48 acquisitions of an 8 mL voxel with an echo time of 30 ms for a preterm infant (top). Acquisitions number 33 and 34 are likely to be corrupted by motion, while acquisitions 35 to 48 are likely to be measured at another position (the spectrum is slightly shifted) and should be rejected. In the bottom panel, the coefficients for the ICA components for the spectra are shown. In this case the most frequent dominant component is component 3, and it is interpreted by the ICA algorithm as the undistorted component. Components 1 and 2 describe acquisitions 33 and 34, which are interpreted as motion corrupted, see top panel. Components 4 and 5 describe the acquisitions 35 to 48. Notice that component 3 almost solely describes the undisturbed data.*

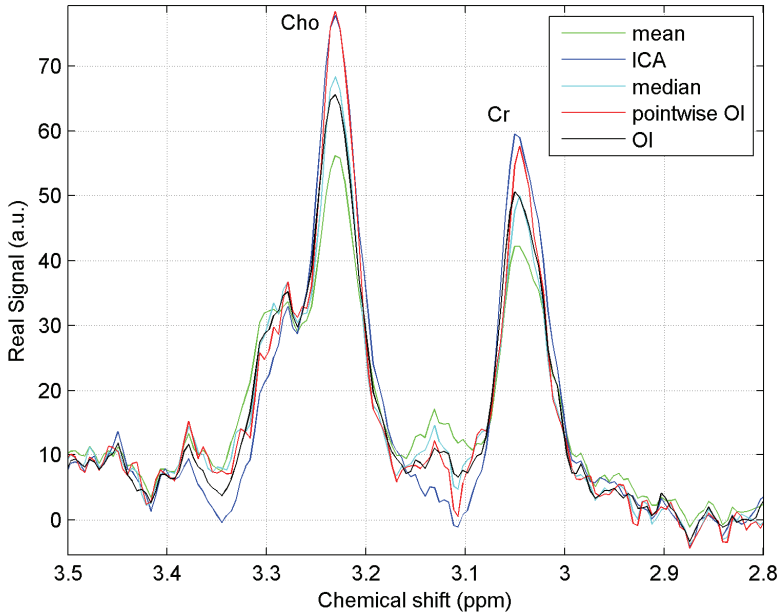

***Figure 3.4**: A part of the zero-order phase-corrected spectrum for a 30 ms echo time after motion rejection with the creatine peak at the right and choline peak at the left. On the left shoulder of the choline peak the myo-inositol resonance at 3.28 ppm is visible. The curves illustrate the performance of the different algorithms, mean, ICA, median, pointwise outlier identification (pointwise OI) and outlier identification (OI). It is clearly seen that the median improves the signal, and that in this case pointwise OI and ICA perform best in agreement with quantitative analysis.*

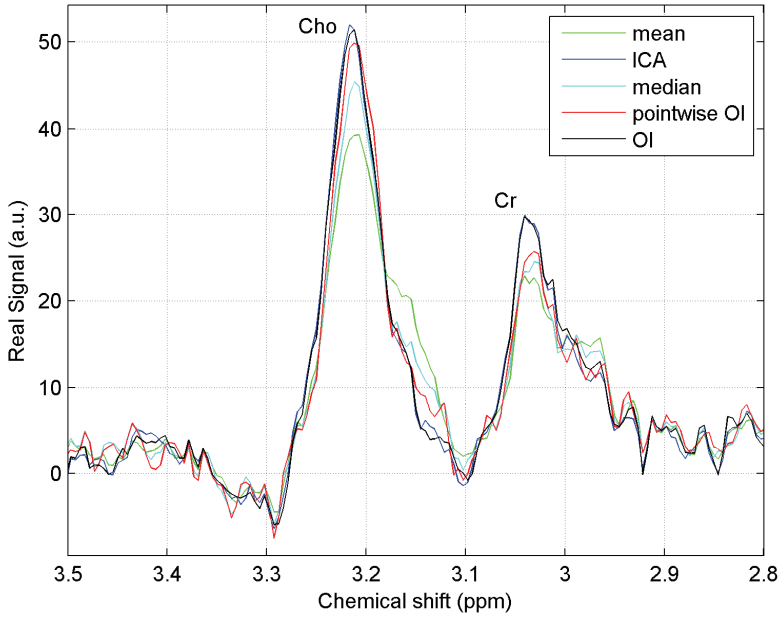

***Figure 3.5**: Graph similar to figure 3.4, but based on data acquired with an echo time of 144 ms. It is seen that the median improves the signal, that pointwise OI performs better, and that in this case ICA and OI perform best in agreement with quantitative analysis.*

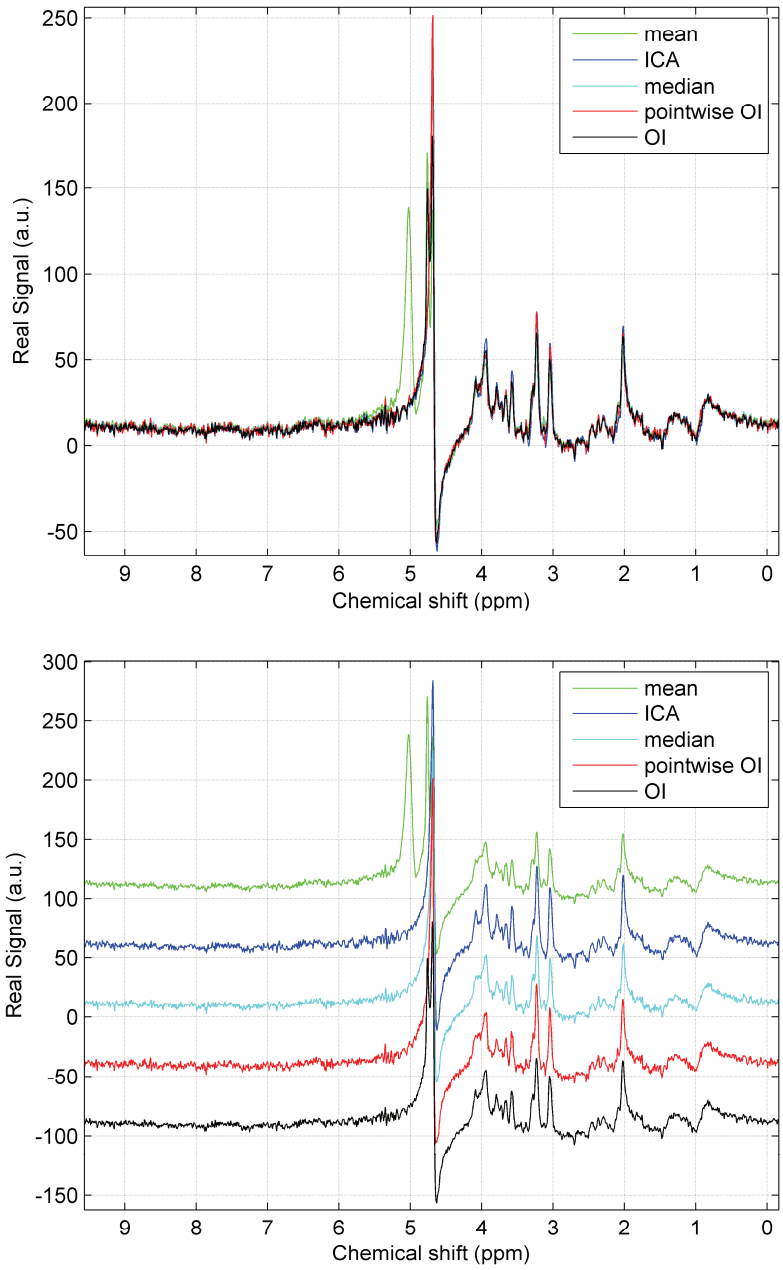

***Figure 3.6**: Entire water-suppressed spectra acquired with an echo time of 30 ms for the same subject as in figure 3.4. The residual water peak at 4.7 ppm is clearly seen. Peaks in the mean signal (green) at 5.0 and 4.8 ppm originate from the residual water signal and subject motion. The top figure shows all spectra on top of each other. The bottom figure shows the spectra vertically separated from each other.*

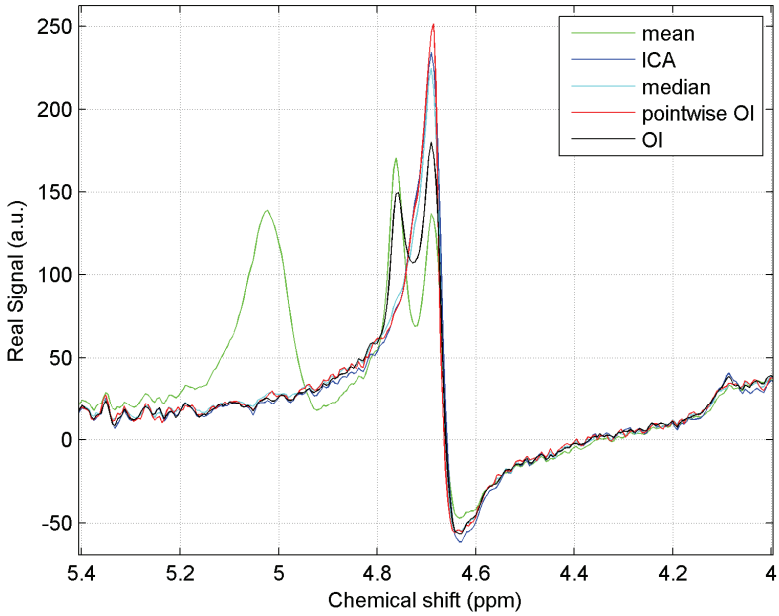

***Figure 3.7**: The 1.4 ppm frequency range around the residual water peak acquired with an echo time of 30 ms for the same subject as in figure 3.4. The residual water peak at 4.7 ppm is clearly seen. Peaks in the mean signal (green) at 5.1 and 4.8 ppm originate from the residual water signal and subject motion. All motion rejection algorithms remove these erroneous water peaks, except the outlier identification with multiple comparisons that fails to remove the peak at 4.8 ppm.*

The Signal and the SNR relative to the signal, as well as the SNR of the mean of all repetitions (both defined as 1) for all motion-rejection algorithms with and without non-motion-distorted acquisitions are shown in table 3.1. The acceptance percentage, defined as the percentage of the data points that is accepted by the algorithms described in the methods section, is shown in the last column. The values for the subset of the datasets where ICA detected more than one component are given in brackets. The values for the signal, the SNR and the acceptance percentage in table 3.1 are averaged over all datasets. All motion-rejection algorithms improve the signal and remove movement artifacts. The results for the dataset of the healthy volunteer, see figure 3.2, were similar to the results in table 3.1.

***Table 3.1**: The mean signal (here "signal" is defined as the average height of the NAA, Cho and Cr peaks), SNR and acceptance percentage for all datasets. Between brackets the values for the subset of datasets where ICA detects more than one component, i.e. with motion artifacts, are shown. Signal and SNR are stated relative to the signal and SNR of the mean of all acquisitions.*

Method	Signal	SNR	acceptance percentage
mean	1	1	100
median	1.030 (1.036)	0.849 (0.866)	100
pointwise OI	1.066 (1.082)	0.739 (0.758)	85.3 (84.8)
OI	1.069 (1.106)	0.939 (0.948)	75.7 (70.6)
ICA mean	1.114 (1.201)	0.950 (0.912)	75.4 (56.7)
ICA all components	1.100 (1.178)	0.976 (0.957)	75.4 (56.7)
ICA main component	1.088 (1.158)	0.970 (0.945)	75.4 (56.7)

Both the signal and the SNR were statistically tested bilaterally between all methods with a paired, double-sided t-test. Apart from the difference in the signal for the two outlier identification methods (point wise OI and OI), all the differences in the signal and the SNR in table 3.1 are significant ($p<0.05$) for all datasets.

3.5.1 ICA and components

138 out of 243 subject spectra (each containing 48 acquisitions) contained more than one component. So in 105 subject spectra the ICA algorithm finds only one component, and identifies differences between this component and the measured signal as noise. The calculated probability of having estimated the correct number of components was less than 100% for 30 of these patient spectra (ranging from 50 to 99%). Of the 138 spectra with more than one component, 43% of the measurements were rejected. The average number of components was 3.2 (range 1-12, the maximum number of components was set to 12) for all measurements and 3.6 (range 2-12) for the motion-distorted measurements. On average 75% of all the measurements were kept.

3.6 Discussion and conclusion

Motion compensation of SVS spectra of non-anesthetized infants and other moving patients is necessary. The effect of motion on the spectrogram of the healthy volunteer in figure 3.2 showed that spectra are corrupted during motion and that the frequency of the metabolite peaks is shifted after motion due to a change of voxel position. During motion of the healthy volunteer, the water peak was reduced while it was increased in the preterm infant. A signal loss as seen in the volunteer spectrum is expected due to imperfect refocusing when motion happens during the spin-echo period of the sequence. A signal increase as seen in the infant spectrum is expected when the water suppression is compromised by movement. The proposed methods detect and compensate both effects.

Visual inspection of the spectra indicates higher signals and better spectral resolution for all the motion-rejection algorithms. In practice it is not possible to visually appreciate the noise properties of the algorithms, for instance by observing the signal where no metabolite peaks are present in figure 3.6. Visual inspection also indicates that the ICA methods are better at suppressing the signal just next to the metabolite peaks and that median filtering does not completely remove the influence of outliers, resulting in a lower signal at the metabolite peaks.

Because motion is likely to reduce the peak height, the signal and the SNR are reasonable measurements for the performance of the algorithms, although since true metabolite concentrations are not known, the true performance is not known. Simulations could be performed to address the issue of the true performance of the algorithms.

If SVS with a relatively large voxel of more than 1 mL is used to measure a “global” metabolite concentration, small changes in which the voxel stays within the same tissue of interest are less relevant than in the case where a small voxel is used and a spectrum at a specific position, e.g. the hippocampus, is required. In the latter case it is advisable to perform a localizer scan before and after the spectroscopy measurement in order to ensure that the voxel position is not changed, even though the acquired spectra are not noticeably different. If the exact voxel position is very important, the selection of the ICA component can be altered by identifying the undistorted component as the dominant component of the first acquisition instead of the most frequent dominant component. In this way the ICA algorithms reject acquisitions that differ significantly from the first acquisition. It is also possible to reject all acquisitions after the first detected movement. On the other hand the selection of the acquisitions in the ICA method only accepts acquisitions which differ by

the ICA-identified noise, which indicates that the underlying noiseless spectrum is unchanged by motion, and that the head has therefore probably returned to the original position after motion.
Quantitative evaluation shows that median filtering results in a considerable improvement of the signal and compensation for movement-distorted spectra. However, it does not perform as well as the other methods, and the SNR is reduced by more than 15% compared to the uncorrected mean signal, although the mean signal may, however, be corrupted. A combination of order-statistics filters such as All-Rank Selection Order-Statistics filtering (Slotboom 2007b) might reduce noise and outlier sensitivity compared to median filtering, but this has not been shown. Pointwise outlier identification has even lower SNR, but slightly better signal amplitude compared to the median filter. Outlier identification with connection between the consecutive Fourier components did not give this SNR loss and restored the signal well. The relatively conservative *p*-value for the pointwise outlier identification method is necessary, as otherwise too many measurements will be excluded. The outlier identification method with multiple comparisons, however, needs a slightly higher *p*-value in order to reject enough measurements.
The resulting noise depends on the algorithm and it increases if the number of accepted acquisitions *n* is lower. The signal is increased if the motion-distorted acquisitions are rejected, and the SNR is reduced less than expected from the increase in noise only. In general the noise in the median is higher than the noise in the mean. For normal distributions this is approximately 25%. The SNR is only 15% lower for the median and this is due to the fact that the median recovers the signal better than the mean. As an estimator, the median is more sensitive to noise, and therefore it is probably better to identify the outliers, reject them, and calculate the mean of the remaining data. Outlier identification with multiple comparisons performs better than the median, but the pointwise outlier identification method does not. This is probably because of the noise sensitivity of the (pointwise) outlier detection itself.
The advantages of ICA compared with the other methods are that no arbitrary thresholds need to be set, that both the resulting signal and the SNR are best, and that it provides a possibility to identify outliers without ignoring connections between consecutive Fourier components. Another advantage of the ICA methods is that they make it possible to accept all the measurements if just one component is considered as most probable, for instance if the patient does not move. Also the range of the acceptance-rate-defined percentage of the measurements which are not rejected indicates larger flexibility. The standard deviation of the

acceptance rate considering both movement-distorted and undistorted data for ICA was 25%, while it was 11% for outlier identification and only 1.5% for pointwise outlier identification. The latter is explained by the influence of the majority of the Fourier components, where no metabolite signal is present. The difference between the three versions of the ICA method was small. Using ICA only to identify movement-distorted acquisitions, and then taking the mean of the remaining acquisitions gives the highest signal. On the other hand, taking the mean of signals reconstructed with the main or all components showed slightly better SNR.

In the case of a short movement, it is possible that the first few measurements after the movement are transients due to history effects in the spin system. ICA will describe this transition with two or more components. Hereafter the measurement is described with one component, different from the component found before movement, unless the subject returned to the original position.

Independent Component Analysis (ICA) instead of the better known Principal Component Analysis (PCA) is used, because the latter maximizes the explained variance for each component, i.e. minimizing the mean square error of approximating the data, whereas ICA seeks independent components. In the case of a measurement with some motion-distorted acquisitions, PCA finds a mixture of all acquisitions for the first and other components (often after the mean has been subtracted), and because of the large deviations in the motion-distorted acquisitions, the uncorrelated principal components will be mainly determined by distorted acquisitions. This gives no opportunity to identify the motion-distorted acquisitions, while ICA finds the undistorted acquisitions as one independent component, and one or more components for the motion-distorted acquisitions. A possible limitation of ICA is that it cannot detect a scaling of the entire spectrum, but since this in practice never happens, it is not a problem. ICA does detect changes in the relative scaling of the metabolite peaks and frequency shifts.

Subject movement will cause the signal values to have a bi- or multimodal distribution. Independent component analysis will find one of the relative maxima, while this is not the case for the mean and median filtering. Outlier identification could find a relative maximum, but only if the other maxima are identified as outliers, which typically is not the case.

Phase-coherent averaging after motion rejection will probably increase the SNR even more, but caution is necessary, since it can potentially introduce a bias (Helms 2001). In this study no phase-coherent averaging

was applied, because only the performance of the motion rejection algorithms was investigated.

3.6.1 Conclusion

Subject movements cannot be ignored in certain patient groups and they need to be compensated for. This can be done by storing the individual SVS acquisitions and identifying and rejecting the acquisitions distorted by subject movements followed by phase correcting (and optionally frequency shift compensating) the individual remaining acquisitions before averaging. It is strongly advised to implement a procedure to detect subject motion. A first implementation of motion rejection in clinical practice could be to monitor the difference between the mean and the median and compare this with the estimated noise. If the difference is significant, the median instead of the mean should be used, or outlier identification or ICA analysis could be applied to the dataset.
Fully automated ICA analysis proved to be the most powerful and reliable tool for movement identification and rejection. In this study the signal increased by 20% for the subject-movement-distorted data, keeping the SNR as high as 91% of the SNR of the mean signal and keeping the undistorted patient data unaffected.

3.7 Metabolite ratios in preterm born infants

Motion correction with ICA was applied to the data of the previously described cohort study of infants. Single voxel proton spectroscopy was used to compare brain metabolite ratios between prematurely born infants at term age and regularly born infants (controls). Epidemiological studies have correlated infection in pregnancy and damage to the immature brain (e.g. Dammann 1997). It was hypothesized that a significant number of prematurely born infants have funicitis (inflammation of the umbilical cord) resulting in increased Lactate levels in the brain.
Lactate is elevated in preterm born infants at term with White Matter Disease (Robertson 2000). It was hypothesized that inflammation and hypoxia-ischemia might be concomitant factors resulting in lactate accumulation (or increased Lactate levels) and decreased NAA levels in prematurely born infants at term age.

3.7.1 Methods

A PRESS sequence with water suppression, echo times of both 30 and 144 ms and a repetition time of 2 s was used. The data was corrected for motion artifacts with independent component analysis, where the motion distorted acquisitions were rejected before averaging. Spectra were first point phased, zero-filled and frequency calibrated with NAA, Cr and Cho. Identical measurements without water suppression were used as peak shape references after adjustment for frequency and T_2 literature value. The real part of the signal was fitted with regression with these metabolite peaks using the peak shape's second derivative for peak width correction. The area under the peak is proportional to the metabolite concentration. The frequency position of the individual peaks was fitted with a peak position finding algorithm. Amongst others the singlets NAA (2.02 ppm), Cr (3.04 ppm), Cr2 (3.94 ppm), Cho (3.22 ppm), Glx (3.77 ppm), Ins (3.54 ppm) and the doublet Lac (1.33 ppm with J=6.94 Hz) were fitted. Peak positions were fitted independently.
Spectra were collected for 20 controls and 67 subjects resulting in usable data for 17 controls and 50 subjects. All the subjects were scanned at a postmenstrual age of 40 weeks. The prematurely born infants had a gestational age between 27 and 34 weeks. Both umbilical cord and placenta were investigated for signs of inflammation. Inflammation of the umbilical cord was regarded as funicitis.
An 8 mL cubic voxel was placed in the posterior periventricular white matter, by the posterior horn of the lateral ventricles (randomly right or left side). Also, a 3.4 mL cubic voxel was placed at the level of the basal ganglia and thalami (randomly right or left side). In order to distinguish between concentration changes and T_2 changes the data was analyzed for both echo times, and the ratio between the short and intermediate echo time peak area for each metabolite and subject was determined. Metabolite ratios were calculated, since the calculation of absolute metabolite concentrations amongst others require precise knowledge of relaxation times. Since some metabolites are detectable at both echo times a rough estimate of the transversal relation time could be obtained, but this was not used in the analysis.

3.7.2 Results

There were no significant differences in the ratios for the two subject groups between short and intermediate echo time for the metabolites detectable at both echo times. This means that changes in ratios at one echo time reflect changes in concentration.
No significant changes in Lactate ratios and NAA ratios were found. The hypothesis of both funicitis and hypoxia-ischemia was not supported by the data. Funicitis (inflammation of the umbilical cord) was only found in 4 subjects.
Choline/Creatine ratios were significantly different between the subject groups, whereas (Robertson 2000) did not find significant differences in Cho levels in subject with on MRI visible WMSH (white matter signal hyperintensities). In table 3.2 the Cho/Cr ratios with a significant (double tailed p-value<0.05) difference are given. The mean value of the statistical control group is stated between brackets. For the last three colums the control group is the part of the preterm infant group that does not have WMSH, chorioamnionitis or funicitis, respectively.
Standard deviation of the Cho/Cr levels is typically less than 0.2. Cho/NAA results are similar to Cho/Cr results.

***Table 3.2**:Cho/Cr levels at 144 ms for the different subject groups.*

Cho/Cr	Controls	premature	WMSH	chorioamnionitis	funicitis
8 ml	2.27	1.79 (2.27)	1.69 (1.81)	-	2.01 (1.77)
3.4 ml	1.90	1.42 (1.90)	-	1.52 (1.40)	1.57 (1.39)

Ins/Cr ratios were lower in premature born infants compared to controls 0.52 vs. 0.70 (TE=30 ms, p=0.05) and 0.22 vs. 0.32 (TE=144 ms, p=0.003) respectively. Glx/Cr was significantly (p=0.03) lower in prematurely born infants compared to controls, 0.76 vs. 1.04 (TE=30 ms). Ins/Cr ratios were higher in the 3.4 ml voxel in subjects with funicitis compared to prematurely born infants without funicitis, 0.82 vs. 0.52 (TE=144 ms, p=0.025).
Since there is no significant T_2 effect, the decreased Choline-levels likely indicates delayed or poorer quality of myelination in preterm infants (not seen on MRI), even in preterm infants at term without brain lesions. This may indicate a detrimental effect of the extra-uterine environment on brain development, as described in Mewer (2006) and Inder (2005).

CHAPTER 4

SPECT

This chapter explains the basic principles of Single Photon Emission Computer Tomography. A description of the basic principles can also be found in Webb (1998) and details about nuclear physics can be found in Krane (1988).

4.1 Basic principles of SPECT

Single Photon Emission Computer Tomography (SPECT) is one of the two main imaging techniques applied in nuclear medicine. Both Positron Emission Tomography (PET) and SPECT are based on the emission of gamma photons inside the body of the patient. In nuclear medicine the source of the measured signal is inside the subject, while in other imaging techniques as e.g. computer tomography (CT) based on the absorption of X-rays the source is outside the subject. CT is based on transmission while SPECT and PET are based on emission.
There are two main differences between SPECT and PET. In PET a positron is emitted which within a few millimeters annihilates with an electron into two photons of 511 keV travelling in opposite directions. In SPECT only one photon is emitted and the energy of the photon is typically between 100 and 200 keV. By the simultaneous detection of the two photons in PET the events can be assigned to a line of response in the scanner and in this way spatial information for calculation of the activity distribution is provided. In SPECT only one photon is emitted at a time and spatial information has to be obtained by the use of a lead

collimator containing parallel holes providing a line of response for each photon at the cost of absorption of photons in the collimator.
Other imaging techniques such as X-ray CT, Magnetic Resonance Imaging (MRI) and ultrasound are dedicated to anatomical details of the human body. SPECT and PET image radio-pharmaceutical distributions which provide functional information of the organ or metabolic process of interest. In nuclear medicine subjects are injected with radio-pharmaceuticals and the distribution of them is determined by blood flow and metabolic processes. SPECT and PET both have their pros and cons. The labeling of pharmaceuticals in PET is often done with isotopes with a low atomic mass as oxygen, carbon and fluor (but also possible with iodine-124, rubidium-82), while labeling in SPECT is done with isotopes with a higher atomic mass as iodine, technetium and thallium.

4.1.1 The gamma camera

In SPECT a gamma camera, which also is called an Anger-camera, is used for the detection of the emitted photons coming from the radio-pharmaceuticals. A gamma camera consists of a collimator, a large-area NaI(Tl) crystal, a light guide for optically coupling the photo-multipliers to the crystal and circuits for position encoding and pulse-height analysis. The entire camera is surrounded by a lead shield to prevent contributions of background radiation outside the field of view of the camera.

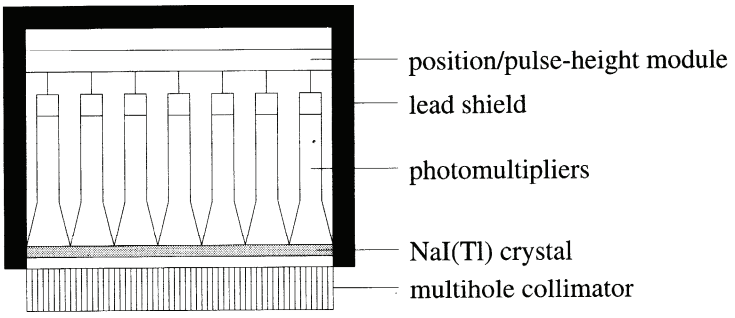

***Figure 4.1**: Schematic view of a gamma camera, showing only its basic components.*

Most SPECT systems now-a-days consist of several gamma cameras mounted on a frame in a such a way that they can rotate around the patient. By acquiring planar images at a sufficient number of angles around the patient, the data required for the calculation of the distribution

of the source activity is obtained. Scintillation crystals are incapable of determining the direction of the incoming photons, and therefore SPECT systems are provided with a collimator. A collimator is usually a slab of lead with several ten thousands of holes which covers the entire detector surface. Most of the photons will be absorbed by the lead. Only the photons that travel through the holes of the collimator without entering the lead will be detected. The direction of these photons is defined by the direction of the hole in the collimator, and this information is essential for the reconstructing of the distribution of the source activity. Unfortunately, this information is obtained at the cost of a tremendous loss in the detected number of counts. The geometric efficiency of a collimator is typically 0.02-0.05 % meaning that only this fraction of the emitted photons will be detected. Collimation is the main reason for the poor count statistics in SPECT.

4.1.2 Scintillation detection

Scintillation detection is the main technique for the detection of gamma photons. It is based on the emission of visible or near-visible light in the scintillation crystals when energy is absorbed from ionizing radiation. This emission of light is a result of the inelastic collisions of the secondary electrons with other atomic electrons. At the photocathode of the photo-multiplier tubes (PM tubes) light is converted into photoelectrons. These electrons are amplified and converted into electrical pulses. For many inorganic scintillation detectors the light emission is proportional to the energy deposit in the material enabling the determination of the energy of the photons, see figure 4.2. Energy resolution is typically 10-15% at 100-200 keV. This enables a rough discrimination between unscattered (primary) photons and photons, which have scattered and lost energy. A photo peak or imaging energy window is applied with a width of typically 15-20% of the photo-peak energy and its center is normally chosen at the energy of the photon.

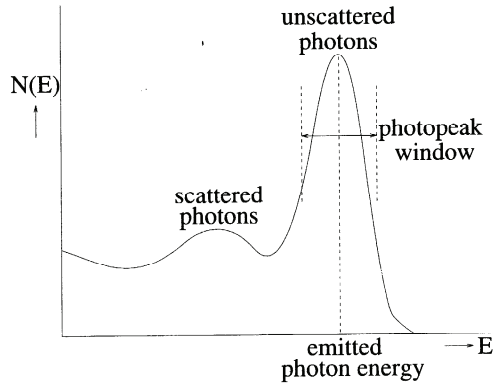

***Figure 4.2**: The pulse-height spectrum from a gamma ray detetected by an inorganic scintillation dectector.*

4.1.3 Collimation

The optimal method for collimation depends on the study and depends on the size of the field of view (FOV), the radionuclide in the radiopharmaceutical and the associated dose. Geometrically there is a choice between parallel-hole, pinhole and converging multihole collimators. The last two are used for smaller objects and have improved sensitivity and resolution. Fanbeam and cone beam collimators are examples of converging multihole collimators. Parallel hole collimators are most widely used, because this collimator is suitable for most studies and it allows fast reconstruction techniques. Spatial resolution R_c of the collimator is depending on both the hole length L and hole diameter d by

$$R_c \approx d \cdot \frac{L+z}{L}, \tag{4.1}$$

with z the source collimator distance. The spatial resolution expressed in mm increases with increasing source collimator distance. There is a trade-off between resolution (smaller holes) and sensitivity (larger holes). There are also demands to the wall thickness of the holes. Ideally speaking it should not be possible for a photon to enter a neighboring hole by penetration of the hole wall. The thickness of the hole wall is called septal thickness. The design of the collimator also depends on the energy of photons. Photons with a higher energy need a higher septal thickness for effective collimation. For radio-isotopes that emit a significant amount of high-energy photons the septa needs to be thicker in order to prevent penetration of the collimator and contamination of the

energy spectrum, or alternatively a correction for the high-energy photons need to be applied.

4.1.4 Poisson statistics

Photons emitted by the radio-pharmaceuticals in the subject are described in good approximation by Poisson statistics. The probability p for a measured number of counts n is given by

$$p(n) = \frac{N^n \exp(-N)}{n!}, \tag{4.2}$$

here N is the expectation value of the amount of counts. The variance or the squared standard deviation is given

$$\mathrm{var}(n) \equiv < n^2 > - < n >^2 = N . \tag{4.3}$$

The Poisson distribution in equation (4.2) can be approximated for large N (10 or higher) with a normal distribution given by

$$p(n) = \frac{1}{\sqrt{2\pi \cdot N}} \exp\left(- \frac{(n-N)^2}{2N} \right). \tag{4.4}$$

4.1.5 Reconstruction

The gamma-camera measures projection data for each slice, where the slice direction is defined in the direction of the axis of rotation. For each position on the camera head the intensity, i.e. the measured amount of counts, comes from a projection line perpendicular to the camera surface, see figure 4.3. A three dimensional distribution of the activity can be calculated from the projections by tomographic reconstruction using the inverse Radon transform. Johan Radon (Radon 1917) published a paper which explained how a real function of two real variables could be reconstructed from all its existing line integrals (the projection lines, p) in the ideal continuous case.

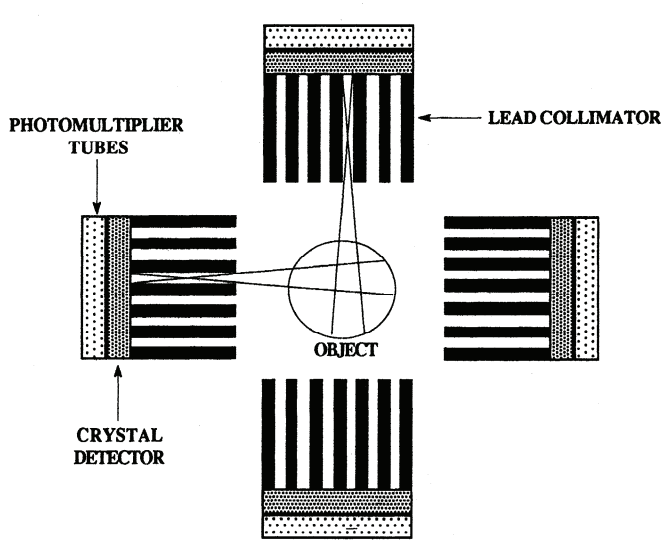

***Figure 4.3**: Image acquisition in SPECT. By moving the detector collimator complex (camera heads) around the object, multiple views are obtained and provide the primary data for image reconstruction.*

Radon's theory is the basis of the well-known filtered back projection (FBP) algorithm which can be formulated (Webb 1998) as

$$I(x,y) = \mathrm{B}(\mathrm{F}^{-1}(|f| \cdot \mathrm{F}(p))) = B(q * p) \quad \text{with} \quad q = F^{-1}(|f|). \tag{4.5}$$

Here F is the one dimensional Fourier transform, f the spatial frequency, $|f|$ the ramp filter and B is the backprojection operator defined by

$$\mathrm{B}(f)(x,y) = \frac{1}{2\pi}\int_0^{\pi} f(x\cos\theta, y\sin\theta)d\theta. \tag{4.6}$$

This operator represents the accumulation of the projections that pass through the point (x,y). The back projection of just the projection data is a blurred version of the desired image. The reconstruction formulas above require all projections to be known. In practice only a finite set of projection lines is obtained and equation (4.5) and (4.6) need to be discretized. This means that the back-projection operator is approximated by summing the finite amount of angles and that it has to be mapped to a discretized Cartesian grid by an interpolation operator. In principle the ramp filter is not a well behaved function, but in the discrete case the ramp filter is band-limited by the maximum frequency of the discrete

Fourier transform. In the Filtered Back Projection algorithm, first the discrete inverse Fourier transform of the ramp filter with limited band-width q is calculated. This filter function q is then convolved with the projection data for each angle. Finally this set of convolutions products is back-projected and mapped on the discretized Cartesian grid by interpolation. This was first desribed by Ramachandran and Lakshminarayanan (1971) and therefore the filter function q is known as Ram-Lak filter, see Webb (1998).

Alternatively, backprojection and interpolation can be applied directly to the projection data resulting in a blurred back-projected image followed by a two dimensional ramp filter. This alternative method is called the back projection filtering algorithm. Because of the discretized version of the ramp filter with zero for the first frequency bin the mean level of the image is lost. However, by applying a non-zero value for the first frequency bin and keeping the original values for the ramp filter for the other frequency bins this can be corrected for. Because the filtering is performed after the back-projection, the back-projection filtering algorithm is more sensitive to aliasing by the finite resolution of the back-projection matrix, but this can be compensated by performing the back-projection in a higher resolution. However, Zeng (1995) showed that even with compensation for the mean level and aliasing the filtered back-projection algorithm is superior to the back-projection filtering algorithm.

The Fourier transform of the projection data is decreasing with increasing spatial frequency and subsequently the signal to noise ratio is lower at higher frequencies (assuming Poisson noise=white noise). The ramp filter amplifies the higher spatial frequencies, which results in an amplification of the noise. Therefore a low-pass filter needs to be applied. Low pass filtering can be applied before and after reconstruction. Before reconstruction the low-pass filter can be incorporated in the Ram-Lak filter by calculating a modified filter function q by calculating the inverse Fourier transform of the product of the ramp-filter and a decreasing function (a low pass filter). This can be combined with low pass filtering in the slice direction if the low pass filter is applied on the Fourier transform of the projection data. This is called two dimensional pre-filtering. After reconstruction a three dimensional low pass filter can be applied on the entire reconstructed three dimensional dataset. A commonly used low pass filter is the Butherworth filter $BW(f)$, which is defined by

$$BW^{-1}(f) = 1 + \left(\frac{|f|}{f_c} \right)^{2n} \tag{4.7}$$

Here n is the order of the Butterworth filter and f_c is the so-called cutoff frequency. The higher the order the steeper the roll-off of the filter.
Filtered backprojection is widely used because of its speed. Other reconstruction methods exist and the most important alternative today to FBP is statistical reconstruction with the expectation maximization algorithm (Lange 1984, Shepp 1982). Unlike the FBP method statistical reconstruction take the Poisson nature of the noise in the projection data into account potentially resulting in images with a lower noise than the FBP-reconstructed images.

4.1.6 The cut-off frequency

The cut-off frequency and order need to be chosen depending on the amount of noise in the projection data. An idea of a suitable cut off frequency can be calculated by analyzing the projection data in the frequency domain P. Since projection data p_i follows Poisson statistics and the noise is frequency independent, the Poisson noise can be estimated from the noise in the DC component of the Fourier transform of the projection data P_0. The squared noise N^2 in the frequency domain is given by the variance, which is given by the total amount counts in the zero frequency bin:

$$N^2 = \mathrm{var}(P_0) = P_0 = \sum_i p_i \tag{4.8}$$

The spatial system resolution (Full Width Half Maximum=FWHM) can be modeled by a Gaussian isotrop system resolution of $\mathrm{FWHM}_x = \sqrt{8 \ln 2} \cdot \sigma_x$. Consequently the system resolution $R(f)$ can be modeled in the frequency domain with $\sigma_x \sigma_f = 1/2\pi$ and

$$R(f) = \exp\left(-\frac{f^2}{2\sigma_f^2} \right) \quad \text{with} \quad \sigma_f = \frac{\sqrt{2 \ln 2}}{\pi} \frac{1}{\mathrm{FWHM}_x}, \tag{4.9}$$

with f the spatial frequency in cm. The frequency spectrum of a projection can then be found by multiplying the system resolution with

frequency spectrum of the object $S(f)$ to be measured. An upper bound of the cut-off frequency can be found by the intersection of the frequency spectrum and the noise, where the Signal-to-Noise-Ratio (SNR) is one:

$$R \cdot S(f_{\max}) = N = \sqrt{\sum_i p_i} \tag{4.10}$$

Alternatively, the measured projection data, which includes noise N, can be used to estimate $f_{\max}$ with

$$P^2(f_{\max}) = 2N^2 = 2\sum_i p_i \ . \tag{4.11}$$

A suitable cut-off frequency can then be found demanding that the applied low pass filter, see equation (4.7), has a certain value, e.g. 10 %, at this maximum frequency, i.e. $BW(f_{\max})=0.1$.
It is important to stress that the cut-off frequency is determined for one projection angle and is not necessarily the same for all projection angles. The modeling of the system resolution with an isotrop Gaussian is an rather crude approximation. In practice the system resolution depends on the distance between object and collimator, see equation (4.1), but for the purpose of determining a reasonable cut off frequency equation (4.10), if the object is known, or alternatively equation (4.11) are reasonable estimates. The cut-off frequency depends on system resolution, the frequency spectrum of the object and the number of counts in the data.

4.1.7 Photon matter interaction, attenuation

Photons in SPECT typically have an energy between 100 and 200 keV. The emitted photons can interact in several ways with matter, but for this energy range three interactions are important (Krane 1988). Sometimes Rayleigh scattering is mentioned as well (Seibert 2005) and the four interactions are illustrated in figure 4.4. The interaction results in an attenuation of the photons and is the sum of four different mechanisms.

Photo-electric effect
All energy is absorbed by an atom and one of the atomic electrons is released.

Pair production
A photon creates a electron-positron pair and the photon itself disappears. This process is only possible if the photon has at least two times the energy corresponding to the rest mass of an electron, i.e. 1022 keV.

Inelastic Compton scattering
A photon scatters from a nearly free atomic electron, resulting in a less energetic photon and a scattered electron carrying the energy lost by the photon

Elastic Rayleigh scattering
The energy of the electron is raised temporarily without removing it from the atom. The electron returns to its previous energy level by emitting a photon of equal energy but with a slightly different direction. Rayleigh scattering has low probability compared to Compton scattering for photon energies used in nuclear medicine.

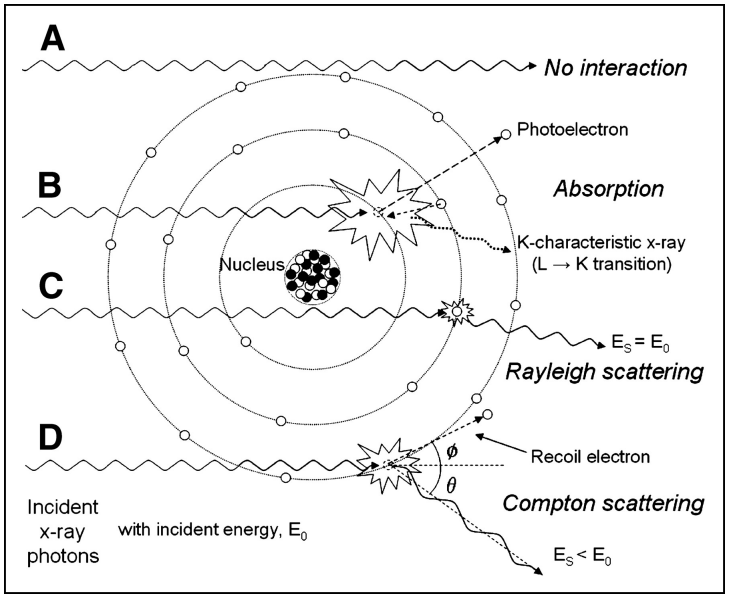

Figure 4.4*: Four possible scenarios of the interaction of a photon with matter. (A) Primary photons do not interact with material. (B) Photoelectric absorption results in total removal of the photon with energy greater than binding energy of electron in its shell, with excess energy distributed to kinetic energy of photoelectron. (C) Rayleigh scattering is interaction with electron (or whole atom) in which no energy is exchanged and incident photon energy equals scattered photon energy with small angular change in direction. (D) Compton scattering interactions occur with essentially unbound electrons, with transfer of energy shared between recoil electron and scattered photon.*

Photons in nuclear medicine do not have high enough energy for pair production, so the interaction is caused by the photo-electric effect and Compton scattering. Interaction with matter causes attenuation.
For matter with low atomic number such as water and brain tissue the photo-electric effect is negligible compared to Compton scattering. In lead which has an atomic number of 82 the photo-electric effect is dominant. In figure 4.5 the first three interaction processes as a function of photon energy and atomic number are shown.

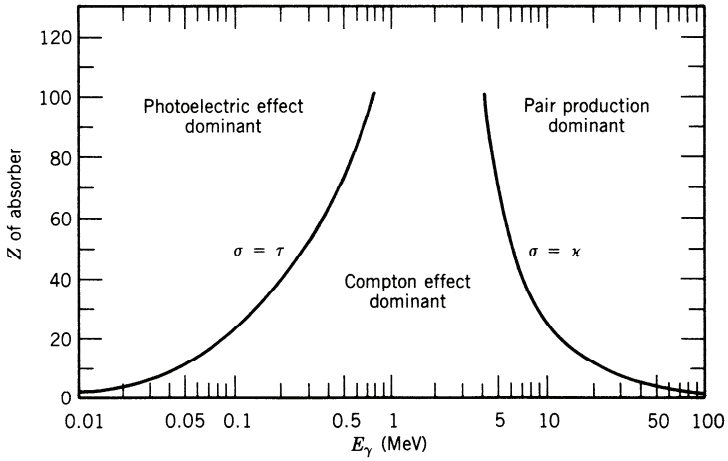

***Figure 4.5**: The three photon matter intertaction processes and their regions of dominance (Krane 1988). The total attenuation factor is the sum of the photoelectric effect (τ), the Compton effect (σ) and pair production (χ).*

4.1.8 Attenuation

The previous described interaction processes result in attenuation of the primary photons. Attenuation is the result of the sum of all possible interactions. Attenuation along dimension x is described by a linear attenuation coefficient μ defined by

$$\frac{dI(x)}{dx} = -\mu(x) \cdot I(x) . \tag{4.12}$$

Here I is the intensity expressed in the amount of counts per second at position x. The linear attenuation coefficient is in principle depending on the position x as the composition of the matter (tissue, bones and air in humans) in differs with position. This can written as

$$\frac{I(x)}{I(x=0)} = \exp(-\int_0^x \mu(x)dx) = \exp(-\mu x), \tag{4.13}$$

where the last equal sign holds for a uniform attenuation factor. Values for the attenuation factor depend both on the photon energy and matter. For brain tissue and 159 keV photons coming from iodine-123 the attenuation coefficient is 0.15 cm^{-1}. This means that after 5 cm of brain tissue only 47% of the original intensity of the 159 keV photons is left.

4.1.9 Chang's attenuation correction

Even if a uniform attenuation factor is assumed it is not straightforward to correct the reconstructed images for attenuation. Attenuation can be integrated in iterative reconstruction, since it is based on forward calculation of images to projection data. In the filtered back projection Chang's attenuation correction (Chang 1978) is often used. Chang's attenuation correction has the advantage that is does not assume a certain distribution of the activity in contrary to Sorenson's attenuation correction (Sorenson 1974), where a uniform distribution along a projection line is assumed. Chang's attenuation correction is a correction factor *C*, which is multiplied on the reconstructed image and is given by

$$C^{-1} = \frac{1}{2\pi}\int_0^{2\pi} \exp(-\mu l_\varphi)d\varphi, \tag{4.14}$$

where φ is the projection angle and l_φ the attenuation path length (distance from pixel to the edge of the attenuation object) for the projection angle. Even if the edge is known it is in practice a bit tedious to evaluate equation (4.14) directly, because the lines between the pixel position and the edge do not correspond with the discrete angles of the projection data. This means that if the data is evaluated at the edge determined under each projection angle equation (4.14) is evaluated with a different weight for the different angles. One solution is a parameterization of the edge which supplies a value for each angle. Another solution is to rewrite equation (4.14) in the following way:

$$C^{-1} = \frac{1}{2\pi}\int_0^{2\pi}\left(1-\mu\int_0^{l_\varphi}\exp(-\mu r)dr\right)d\varphi = 1-\frac{\mu}{2\pi}\iint_H g(r)dxdy$$

$$\text{with } g(r)=\frac{\exp(-\mu r)}{r} \text{ and } r=\sqrt{x^2+y^2}\,, \tag{4.15}$$

where H refers to the area of the head. This equation can immediately be evaluated and approximated in sampled data with pixelsize d at grid x,y with $x = i \cdot d, y = j \cdot d$. However, this approximation is not possible in the origin, because r=0, there equation (4.15) needs to be calculated for the first pixel with

$$d \cdot g(0) = \frac{\int_{-\frac{d}{2}}^{\frac{d}{2}}\int_{-\frac{d}{2}}^{\frac{d}{2}} g(r)dxdy}{d} = 4\ln\left(1+\sqrt{2}\right)-\mu d + O((\mu d)^2) \tag{4.16}$$

$$\approx 3.5255 - \mu d$$

Here the last integral is approximated for small values («1) of μd. This is practically always the case, and the highest values for set-ups in this thesis are $\mu = 0.15\ \text{cm}^{-1}$ and a pixelsize of 2.33 mm yielding $\mu d = 0.035$.

4.1.10 Compton Scatter

Photon matter interaction not only result in attenuation, but also in the appearance of photons with a lower energy. The energy of a photon after Compton scattering E_C can be calculated with (Krane 1988)

$$E_C = \frac{E_\gamma}{1+(E_\gamma/mc^2)(1-\cos\theta)}\,. \tag{4.17}$$

Here E_γ is the original energy of the photon, mc^2 is the rest energy of an electron (511 keV) and θ is the angle of the scattered photon. Zero angle corresponds to no interaction. The energy loss is highest at an angle of 180 degrees, called backscatter. Photons can scatter multiple times resulting in photons with a much lower energy than the primary photon.

4.1.11 High-energy photons

Ideally the radio-isotope of the radiopharmaceutical emits mono-energetic gamma radiation. In practice this is often not the case. The radio-isotope might emit both gamma photons with a lower and higher energy. Photons with a lower energy do not have a big influence. They are absorbed more than the primary photons and their energy lies beneath the imaging energy window. By scattering these low-energy photons end with an even lower energy. However, if the so-called dual energy window (DEW) correction scatter correction (Jaszczak 1984), and the unscattered low-energy photons have an energy just below the primary photons, the low-energy photons might have an influence on the final images.
High-energy photons are more problematic, since they also loose energy by Compton scattering in the subject and the camera head. They can very well end in the imaging energy window and give rise to erroneous counts and consequently deteriorate the final images. This process is called downscatter, because the photons “move” from the upper to the lower part in the energy spectrum.

CHAPTER 5

Downscatter correction in SPECT

In this chapter downscatter correction in I-123 Single Photon Emission Computer Tomography (SPECT) by the subtraction of a second energy window from the imaging window with identical width is described. Others have performed this correction with a weight of one for the downscatter window. However, the second window needs to be weighted with a factor higher than one due to a broad backscatter peak from high-energy photons appearing at 172 keV. Spatial dependency and numerical value of this weight factor and the image contrast improvement of this downscatter correction was investigated. The weight factor was measured with a lead shielded I-123 point source inside and a non shielded I-123 point source outside the SPECT scanner. For comparison the weight factor was also determined in 5 healthy subjects and 5 patients in a dopamine transporter brain SPECT study with the PE2I-tracer. Contrast in the reconstructed images was measured as specific binding ratio of both the left and right striatum and as the count density ratio between a reference region in the brain and the count density outside the subject. After applying downscatter correction the measured specific binding ratio increased significantly for healthy subjects with typically more than 20%. It was shown that the weight factor despite identical window widths is higher than one. In clinical practice a weight factor of 1.1-1.2 can be applied.

5.1 Backscatter of high-energy photons

Radioisotopes used for imaging with Single Photon Emission Computer Tomography (SPECT) like Technetium-99m typically emit photons with an energy between 100 and 200 keV that allows effective collimation by lead. Iodine-123 which has a primary photon energy of 159 keV also emits a significant amount of photons with a higher energy (abundance 3.1%). The most important of these have a photon energy of 529 keV and an abundance of 1.4%, whereas the primary photons at 159 keV have an abundance of 83.4% (Kocher 1981). The high-energy photons are not well collimated but penetrate through the lead into the scintillation crystal (septal penetration). Also photons from the parts of the patient's body outside the SPECT scanner may contribute by penetration through either the collimator or the camera shield. At 529 keV in Sodium Iodide, Compton scatter is a far more likely process than photo absorption, and only a minor part of the counts will be located at the 529 keV photopeak. Because the high-energy photons are detected at a lower energy this process is called downscatter. The resulting spectrum is rather flat with little structure above the 159 keV peak, except for a weak and broad backscatter peak around 172 keV corresponding to photons passing the collimator and crystal without interaction being backscattered in the material behind and finally absorbed. Due to the low efficiency of collimators and the high probability of penetration, the erroneous counts coming from the high-energy photons (despite the much lower abundance) become a significant fraction of the observed signal at 159 keV, and subsequently the reconstructed SPECT images are deteriorated. The contribution of the high-energy photons depends on the type of collimator and is significant for Low Energy collimators (Dobbeleir 1999). The observation of a fairly constant energy spectrum above the 159 keV peak see figure 5.1a suggests that a correction can be estimated from a second energy window with identical width above the one used for imaging. Based on the implicit assumption of a flat energy spectrum the second energy window may just be subtracted from the imaging window before reconstruction (Small 2006, Kobayashi 2003, Motomura 1999).

However, within the imaging window at 172 keV a broad backscatter peak coming from high-energy photons is present (Tanaka 2007). The fact that the so-called Compton edge at 358 keV coming from the 529 keV photons is visible in the energy spectrum in figure 5.1a indicates that the contribution of the high-energy photons is significant. Therefore it is expected that the second energy window has to be weighted with a

factor slightly higher than one depending on the height of the backscatter peak. The impact of the energy window subtraction on the final images and the value of the appropriate weighting factor for the second energy window have been investigated in a brain SPECT-study and in experiments with an I-123 point source.

5.2 Energy windows and imaging

Measurements were performed with a triple head IRIX camera (Philips Medical, Cleveland, U.S.A.) fitted with parallel hole Low Energy General Purpose (LEGP) collimators (spatial resolution 8.5 mm at 10 cm distance to the collimator). Projection data was obtained in 128x128 matrix size with an isotropic pixel size of 2.33 mm.
Two energy windows both with a full width of 32 keV were set at 143-175 keV for the primary imaging photons with corresponding raw projection data **I** (imaging) and 184-216 keV for the downscattered photons with projection data **D** (downscatter). In order to minimize the overlap of primary photons in the downscatter window the small energy gap between the two windows was chosen based on the properties of a Tc-99m spectrum (not shown). Downscatter corrected projection data **J** was calculated with

$$\mathbf{J} = \mathbf{I} - k \cdot \mathbf{D}\,, \tag{5.1}$$

where k is the spatially invariant weighting factor for the downscatter window.
SPECT imaging of the subjects was performed by recording projection data at 120 fixed angles with an interval of 3 degrees with a non-circular orbit. The mean radius of rotation was 13.9 cm. Reconstruction of projection data with and without downscatter correction was performed in MATLAB 7.5 (Mathworks, Natick, Massachusetts, U.S.A.) in 128x128 matrices (2.33 mm pixels and identical slice thickness) using standard filtered back projection (FBP) with a 3D low pass 4th order Butterworth postfilter with a cut-off frequency of 0.3 Nyquist (=0.64 cm^{-1}) and using first order Chang's uniform attenuation correction (Chang 1978) with an empirical linear attenuation factor of 0.10 cm^{-1} for I-123 imaging without Compton scatter correction of the primary 159 keV photons (Shiga 2002).

5.3 Experimental determination of the weighting factor

The weighting factor k in equation (5.1) was determined experimentally with an I-123 point source with 37 MBq activity, where the primary photons were "removed" by (I) shielding the source with 6 mm lead, efficiently excluding the 159 keV photons, and placing it inside the camera field-of-view (FOV), and by (II) placing a 6.3 L cylindrical water filled phantom with a diameter of 16 cm inside the scanner as a scattering medium for mimicking a subject and placing the unshielded I-123 source outside the FOV, near the scanner axis, but 20 cm in front of the gantry.
Camera angles in both experiments were positioned at 90 (collimator surface perpendicular to the floor), 210 and 330 degrees, and the weighting factor k was determined as the ratio of the total amount of counts between the two energy windows in the raw projection data with

$$k = \frac{\sum \mathbf{I}}{\sum \mathbf{D}}. \tag{5.2}$$

The energy spectrum in figure 5.1b shows the contribution of the high-energy photons for the lead shielded I-123 point source (method I) as a broad peak at 172 keV. This energy spectrum looks very similar to the spectrum of a Fluor-18 source (emitting mono-energetic photons of 511 keV) in the SPECT-scanner with low-energy collimators. In method II some of the 159 keV primary photons scatter around 90 degrees in the water filled phantom and give rise to 121 keV photons, but the primary photons are effectively removed, see figure 5.1c. The broad backscatter peak of the high energy photons at 172 keV is less clearly visible in the latter case.

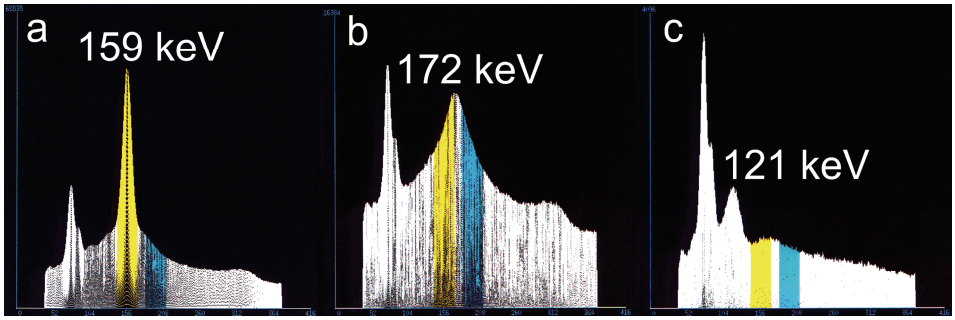

Figure 5.1: *Energy spectra of the detected photons from an Iodine-123 point source as measured by the SPECT-scanner. In the left panel (a) the spectrum of an unshielded I-123 source is shown. The Compton edge at 358 keV for 529 keV photons is visible. The photons with an energy of 159 keV are used for imaging. The middle panel (b) shows the energy spectrum for the I-123 source shielded with 6 mm lead. The broad peak at 172 keV comes from backscattered high-energy photons. The right panel (c) shows the energy spectrum for the I-123 source placed outside the scanner. The peak at 121 keV comes from 90 degree Compton scattering of 159 keV photon in the object placed in the scanner. The peaks between 50 and 100 keV come from interactions with the electron shells of the collimator's lead. The imaging energy window is highlighted with yellow and the (higher) second energy window with cyan.*

5.4 The spatial dependence of the weighting factor

In order to investigate the spatial dependence, pixelwise *k*-maps were calculated. Because the uncertainty in *k* depends on the number of counts which varies with position a *z*-score, which does not scale with the amount of counts, was calculated. With I and D the pixel value in the corresponding projection data **I** and **D** the *z*-score for each pixel was defined by the difference between the global *k* factor defined by equation (5.2) and the pixel value $k_{\text{pixel}} = I/D$ normalized by the theoretical standard deviation σ_{pixel}, and given by

$$z = \frac{k - k_{\text{pixel}}}{\sigma_{\text{pixel}}} \approx \frac{k - \dfrac{I}{D}}{k \cdot \sqrt{\dfrac{1}{I} + \dfrac{1}{D}}} \quad . \tag{5.3}$$

Here the squared relative standard deviation (the relative variance) was calculated with reciprocal value of the number of counts (assuming Poisson statistics). The relative variance of the quotient I/D was approximated for small relative variances by adding the relative

variances of I and D. In order to detect significant outliers the doublesided p-value was calculated from z for every pixel based on the assumption that the data was normally distributed. Negative differences in equation (5.3) were indicated with a negative p-value. All pixelwise p-values were corrected for multiple comparisons with the Bonferroni method by multiplication with a global scaling factor $P/(1-\sqrt[n]{1-P}) \approx n$, where P=0.05 is the overall significance level and n the number of pixels. For small P-values the scaling factor is approximately the number of comparisons. In this way a scaled p-value of 0.05 corresponds to a double sided 5% confidence value corrected for multiple comparisons. Since outliers have a low p-value pixelwise $1/p$ maps, where outliers have high intensity, are calculated. Pixelwise k-maps and $1/p$-maps were investigated in different matrix sizes, because another balance between uncertainty and spatial resolution can reveal other outliers. Resolution was reduced by box filtering with a uniform kernel, i.e. adding the counts in the kernel area. In this way Poisson statistics is preserved at the reduced resolution.

5.5 Subjects and evaluation of the downscatter correction

The downscatter correction was investigated in human brain studies of the dopamine transporter binding in 5 healthy subjects and 5 patients. All subjects had informed written consent, the study was performed in accordance with the ethical standards of the Declarations of Helsinki and was approved by the ethical committee of Copenhagen and Frederiksberg (KF 12-009/04).

An average intravenous bolus of 74.3 MBq (range 65.8-79.9 MBq) of [^{123}I]PE2I (MAP-Medical Technologies Oy, Tikkakoski, Finland) was given, immediately followed by a constant infusion (mean 96.5 MBq; range 88.6-100.1 MBq) of [^{123}I]PE2I for three hours. The Bolus/Infusion (B/I) protocol was similar in both healthy subjects and patients, with a bolus worth 2.7 hours (range 2.6-2.8 hours) of infusion (the B/I ratio). (Pinborg 2005, Ziebell 2007). Six SPECT acquisitions each of 10 minutes duration were obtained between 120 and 180 minutes post injection and resulting in typically 3-3.5 million counts (range 2.4-4.2 million counts) in the primary energy window for the summed acquisitions. The total amount of counts in the downscatter energy window was approximately 35-40% of the total counts in the primary window. Image quality after reconstruction with FBP and applying

Chang's attenuation correction and 3D-postfiltering was evaluated as the contrast, defined as the ratio of the count concentrations in the Volumes of Interest (VOI), between the striatum and a reference region of the brain on the same slices, and the contrast between the intensity of the background outside the subject and the reference region. The latter two regions are expected to have a uniform intensity, but this is not the case for the regions with the striatum. Specific binding ratio (SBR) is used as a measure for striatal contrast, which has the advantage that it is a clinically known and familiar quantity. The SBR is defined by the ratio of the specific striatal count concentration and the reference count concentration in the rest of the brain. Count concentrations are defined by $c \equiv C/V$ and measured in counts/mL with C the amount of counts and V the volume in mL. In order to minimize the subjectivity of drawing VOIs a method similar to the one developed by Tossici-Bolt et al (2006) was used. Relatively large VOIs covering a larger volume than the striatum were drawn on every slice where the striatum was visible and the SBR for each striatum was calculated with

$$\mathrm{SBR} \equiv \frac{c_\mathrm{S} - c_\mathrm{ref}}{c_\mathrm{ref}} = \frac{1}{V_\mathrm{S}} \cdot \left(\frac{C_\mathrm{VOI}}{c_\mathrm{ref}} - V_\mathrm{VOI} \right), \tag{5.4}$$

where subscript S refers to the striatum, VOI to the volume of interest around the striatum, and subscript ref to the reference region. Identical VOIs were used for both reconstructions with and without downscatter correction. VOIs were drawn on reconstructed non-resliced images on each single slice, where the striatum was (or just not) visible. A standard striatal volume of 11.2 mL was assumed (Bolt 2006), but this might be significantly different from the volume measured by a structural MRI-scan due to individual variation (Koikkalainen 2007). Ziebell et al (in preparation) reported a variation of 36% in striatal volume measured with MRI of 8 subjects. So some caution is needed before interpreting the SBR-values determined in this way. However, in this study the improvement in SBR by downscatter correction is important, and since the striatal volume is a constant scaling factor in equation (5.4) it cancels in the calculation of the relative improvement in SBR.

For comparison with the I-123 source experiments the weighting factor in each of the 10 subjects was determined by minimizing the background *outside* the subject. Since there should be no counts, neither primary photons nor scattered primary photons, outside the subject in the corrected projection data, i.e. **J=0** in equation (5.1), the weighting factor can be determined by applying equation (5.2) using the counts in the

region outside the subject only. In order to assure the correctness of the assumption of no counts in the region outside the subject, the region for determining k was drawn at 3 pixels (=7 mm) (radially) from the edge (edge offset) of the head in the reconstructed image. The region selection was aided by an algorithm which finds the most outward placed crossing of a manually set threshold and the intensity for every projection angle in the sinogram. The threshold was tuned at the edge (this is used for Chang's attenuation correction) and the radial distance to the centre was increased with the edge offset. The weighting factor k was calculated with equation (5.2) applied at the raw projection data. For one subject the edge threshold was varied in order to investigate the influence on k. Differences between subject groups were t-tested, and the stated p-values are calculated by standard two-tailed t-tests. For the independent t-test, equal variance was not assumed.

5.6 Results

By determining the ratio of the total amount of counts in the raw data for the three projection angles the weighting factor k was calculated with equation (5.2). The weighting factor was 1.123, 1.132 and 1.122 for the measurements with the lead shielded I-123 source in the scanner. The total number of counts in the primary window was 1.7, 1.1 and 1.7 million counts. The uncertainty in k due to Poisson statistics was less than 0.002. The weighting factor determined for the I-123 source placed outside the scanner was 1.107, 1.109 and 1.115 for the three angles. The total number of counts in the primary window was 0.37, 0.39 and 0.24 million counts. The uncertainty in k due to Poisson statistics was less than 0.003.

Figure 5.2 shows the images from the imaging and downscatter window for the lead shielded I-123 source (upper row) and the I-123 source placed outside the scanner (bottom row) for the 90 degree angle of the camera head. The k-maps and $1/p$-maps in figure 5.3 (I-123 in lead) and 5.4 (I-123 outside the scanner) show almost no significant differences from the global value for k. However, to the left of the k-map relatively far away from the source there might be a larger area with a somewhat lower value of k. This is also seen relatively far away from the source at the other two angles (not shown). In 8x8 matrix size this is also indicated by four pixels with a significant negative difference.

Based on the experiments with the I-123 source a value of 1.1 for k for the reconstruction of the subject data was chosen. The results for the subjects are listed in table 5.1. For comparison with the I-123 source

experiments the weighting factor *k* was determined in the subjects by minimizing the background and ranged from 1.155 to 1.170 for healthy subjects and significantly different ($p<0.005$) from 1.174 to 1.181 for patients.

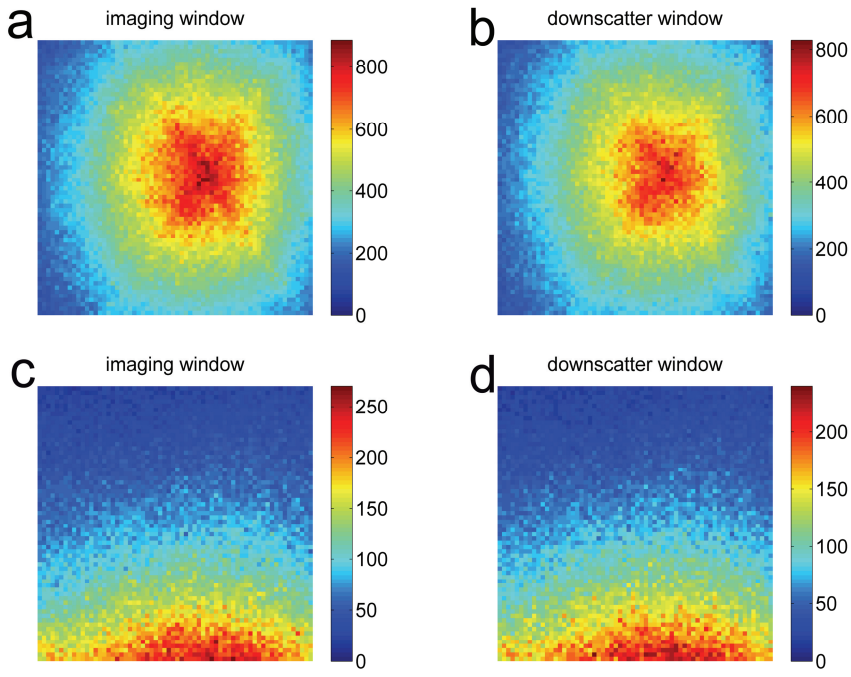

***Figure 5.2**: The raw projection data images acquired by placing an I-123 source shielded with 6 mm Lead in the SPECT-scanner (ab) and by placing the I-123 in front of the scanner (cd). Images are shown in a matrix size of 64x64. In the left column the raw projection data for the two source positions the imaging energy window (143-175 keV) is shown. The right column shows the identical data, but for the downscatter energy window (184-216 keV). The colour scale shows the amount of counts for the projection data*

The uncertainty in *k* caused by the limited amount of counts was 0.002 for all subjects. The background in the image was effectively removed by the downscatter correction for all subjects. The contrast between background outside the subject and the reference region decreased from (mean +/- SD) 0.15 +/- 0.02 to 0.00 +/- 0.01. A t-test revealed a significant difference ($p<0.005$) between the SBR with and without downscatter correction for each striatum in healthy subjects. The difference in SBR was not significant ($p>0.2$) for the patient group. SBR for the healthy subjects increased with (mean +/- SD) (23 +/- 3) % and

(22 +/- 5) % for the left and right striatum, respectively. The relative SBR change in the striatum for patients ranged from -13.5% to 16.9% (left striatum) and from -10.0% to 20.2% (right striatum). Linear regression without intercept revealed a slope of (1.21 +/- 0.01) between corrected and uncorrected SBRs for all subjects and both left and right striatum in table 5.1. The correlation coefficient was 99.8%.

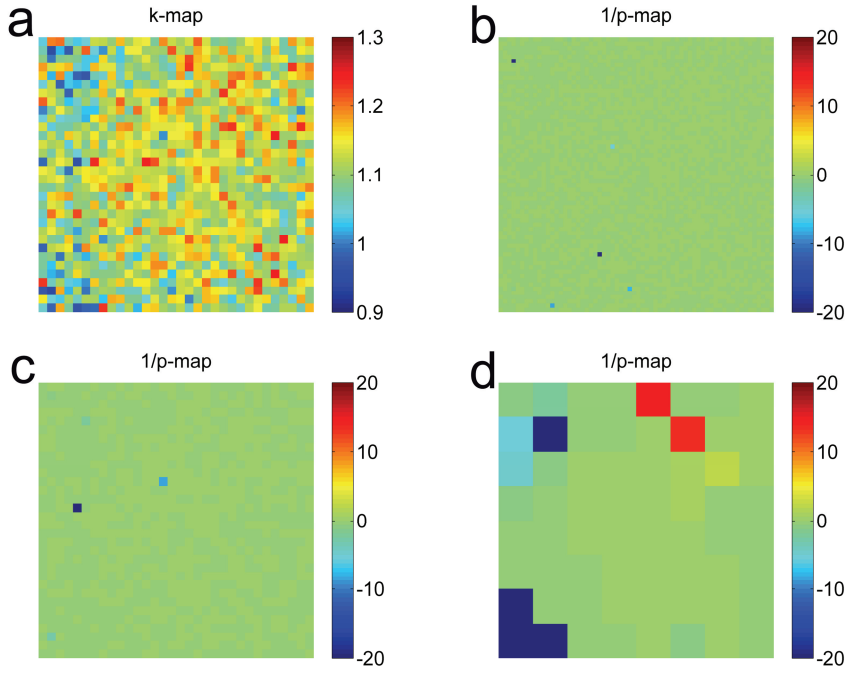

***Figure 5.3**: k-maps and 1/p-maps for the Iodine-123 source in lead. The top left image show (a) shows the ratio (k-map) of the two images of the two energy windows in a 32x32 matrix size. In other image (bcd) 1/p-maps are shown in a matrix size of 64x64, 32x32 and 8x8. The colour scale shows the value of k and 1/p for their respective maps. The p-values correspond to Bonferroni corrected double sided significance levels, and a 1/p value of 20 corresponds to a significance level of 5%. Negative p-values indicate negative differences.*

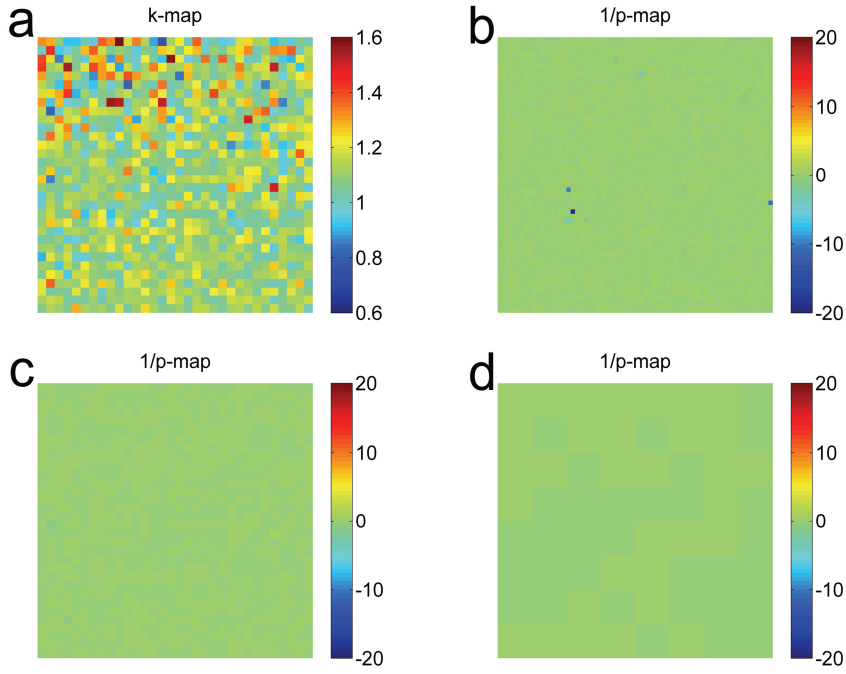

Figure 5.4*: k -map and 1/p-maps for the Iodine-123 source placed in front of the scanner. The top left image show (a) shows the ratio (k-map) of the two images of the two energy windows in a 32x32 matrix size. In other image (bcd) 1/p-maps are shown in a matrix size of 64x64, 32x32 and 8x8. The colour scale shows the value of k and 1/p for their respective maps. The p-values correspond to Bonferroni corrected double sided significance levels, and a 1/p value of 20 corresponds to a significance level of 5%. Negative p-values indicate negative differences.*

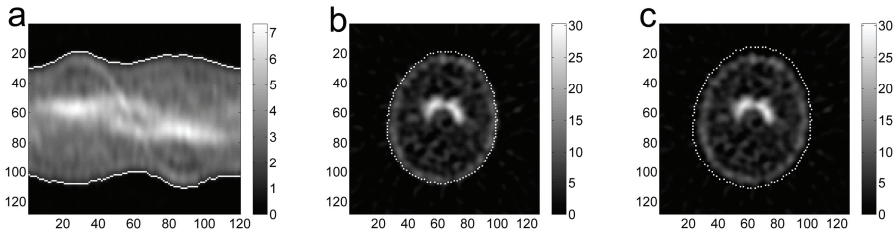

Figure 5.5: *Illustration of the edge detection in a healthy subject (subject 3). The left panel (a) shows the so-called sinogram for a slice. Vertically the tangential position and horizontally the 120 angles are shown. The right panel (b) shows the corresponding reconstructed slice. The edge is shown with maximum intensity (white). The right panel (c) shows the edge with a radial offset of 3 pixels.*

***Table 5.1**: Results for the evaluation for 5 healthy subjects (1-5) and 5 patients (I-V). In the numerical fields where two values are separated by a slash the first value is without downscatter correction (k=0) and the second value is with downscatter correction (k=1.1). The percent symbol denotes the column with the relative effect in % of the downscatter correction. The last column shows the contrast between background and the reference region. Uncertainty due to the amount of counts in SBR is of the order of 0.1.*

subject	*k*	SBR left	%	SBR right	%	Bg/Ref
1.	1.159	6.17/7.35	19.2	6.14/7.07	15.1	0.162/0.008
2.	1.168	9.22/11.03	19.7	8.76/10.43	19.0	0.134/0.006
3.	1.170	10.14/12.61	24.4	9.72/12.28	26.4	0.152/-0.014
4.	1.163	8.45/10.70	26.6	9.13/11.32	24.1	0.152/-0.013
5.	1.155	9.25/11.46	23.9	7.91/9.93	25.6	0.133/-0.003
I.	1.179	2.11/2.28	7.9	2.06/2.31	12.3	0.119/-0.013
II.	1.174	3.99/4.66	16.9	5.50/6.61	20.2	0.117/0.004
III.	1.180	1.43/1.23	-13.5	1.72/2.02	17.9	0.141/0.007
IV.	1.181	5.30/5.69	7.3	4.38/4.50	2.7	0.155/0.004
V.	1.177	1.25/1.21	-3.1	1.57/1.42	-10.0	0.202/0.006

Figure 5.5 shows the edge detection in a sinogram and the corresponding reconstructed slice in a healthy subject. Figure 5.6 shows the determined weighting factor as a function of the edge offset. Figure 5.7 shows a reconstructed slice for a healthy subject with and without downscatter correction and the manually drawn regions of interest for determining the specific binding ratio and the contrast between background and reference region. Figure 5.8 shows an intensity profile though the left striatum of the healthy subject with and without downscatter correction. Figure 5.9 shows a reconstructed slice for a subject V in table 5.1 with and without downscatter correction and the manually drawn regions of interest. In a typical patient study the amount of counts in the downscatter window is approximately 35-40% of the amount of counts in the imaging window comparable to the value reported by Du et al (2006). Downscatter (with k=1.1) and non-downscatter corrected images are visually comparable, but show improved contrast. Because of the energy window subtraction the mean amount of counts in the reference region, the background and in lesser degree in the striatal region is decreased.

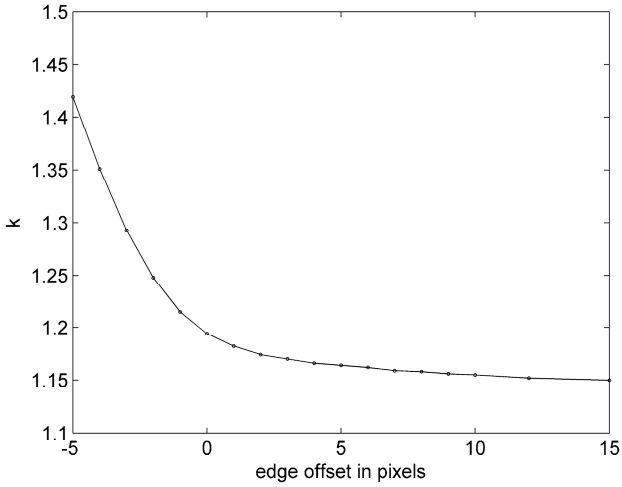

***Figure 5.6**: The calculated weighting factor k as a function of the edge-offset. Within the object (offset<0) the assumption of no primary photon counts for the calculation of k does not hold.*

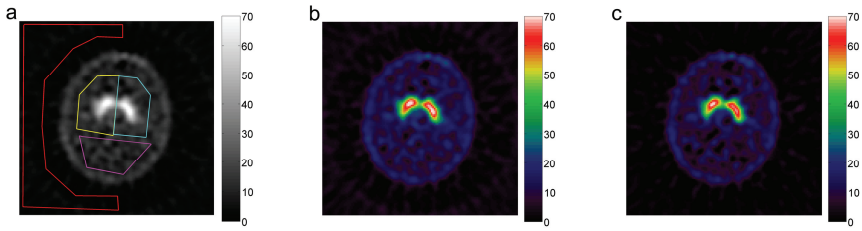

***Figure 5.7:** A slice of a reconstructed SPECT image for subject 3 (normal) in table 5.1. In the left panel (a) the regions of interest are drawn. The ROIs for the left stratium, right striatum, the reference region and the region outside the brain are drawn in yellow, cyan, magenta and red, respectively. In the middle panel (b) the reconstructed image without downscatter correction and in the right panel (c) the reconstructed image with downscatter correction are shown. Note the lower background and the improved contrast between the striatum and reference region. The amount of counts in the striata is slightly lower with correction, and the background outside the head is minimized by the correction.*

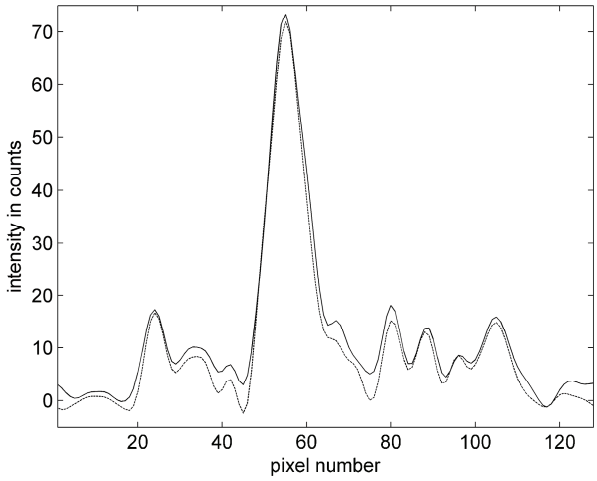

***Figure 5.8**: Intensity profile from front to the back of the head through the maximum of the left striatum of the healthy subject in figure 5.7. The solid line is without downscatter correction and the dashed line is with downscatter correction. Maximum intensity is close to be the same, but the intensities are lower in the brain regions outside the striatum and close to zero outside the head.*

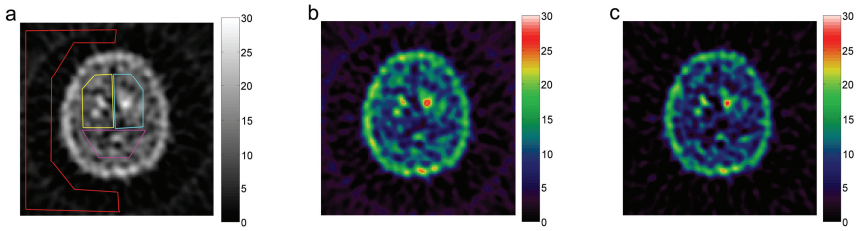

***Figure 5.9**: A slice of a reconstructed SPECT image for subject V (patient) in table 5.1. The shown images are similar to figure 5.7.*

5.7 Discussion and conclusion

Values for the weighting factor *k* for all experiments are between 1.1 and 1.2. There was however a small difference between the three angles and two set-ups with the iodine source which cannot be accounted for by Poisson noise only. A possible explanation of this small variation is the uncertainty in the calibration of the camera heads, the noise in the electronics or a small distance and/or geometrical dependency of *k*. Possibly the fact that the 6 mm lead attenuates the photons coming from I-123 between 300 and 500 keV more than the 529 keV photons might also be a factor contributing to the difference. One of our a-priori assumptions was that the factor *k* is position independent, because there are no obvious mechanisms that could introduce a strong geometrical dependency. Inspection of the images in figure 5.3 and 5.4 indicates that the assumption of a spatially invariant weighting factor *k* holds reasonably. Relatively far away from the source the weighting factor *k* might be lower, but this is less important, as it is far away from the source position outside the central field of view. Figures 5.3 and 5.4 show a fairly constant and identical value of *k*, even though the geometrical set-up is different. The amount of noise in the second set-up is higher especially in the upper part of the image due the low amount of counts.

Slightly higher differences between the weighting factor determined by the I-123 source experiments and the subjects were found. Figure 5.6 shows the dependency of *k* on the edge offset for a healthy subject. The determined weighting factor increased with decreasing edge-offset. Possibly the assumption of no primary photons close to the edge does not hold, resulting in a too high value for *k*. However, the value of *k* determined for the volume of stacked layers around the head between 3 and 5 pixels edge offset was calculated as 1.245 +/- 0.009. Because of the distance to the edge the assumption of no primary photons counts holds, and this indicate that the *k*-factor is slightly higher for projection lines going through the head. This may correspond to high-energy photons backscattered in the subject and detected in the imaging window. In order to understand this dependency this could be investigated with a Monte Carlo simulation, which also might reveal the value of *k* for the position corresponding to projection lines going though the head. Source-detector distance dependency of the downscatter count rate has been reported before (Dobbeleir 1999, Small 2006), and if this distance dependency is energy dependent this might be an explanation of the distance dependency of weighting factor *k*. The significant difference in *k* between subjects and patients is small although significant. The

difference might be caused by the more uniform distribution of the activity in the brain in patients due to the lower activity in the striatum.
In the case of scatter of the primary photons energy window subtraction can in principle be performed before or after reconstruction, since both primary and scattered photons are collimated (Jaszczak 1984). Since the downscattered photons are (almost) not collimated the assumption of perpendicular parallel projection lines is not valid. Reconstruction based on this assumption is therefore not possible, and subtraction of the downscatter energy window has to be performed *before* reconstruction. While the sinogram of the primary photons have a clear structure as in figure 5.5a the sinogram of the downscattered photons (not shown) has almost no visible structure, no edges and the intensity decreases slowly and smoothly with increasing radial distance from the center of the field of view almost without angular dependence.
The contribution of the downscattered high energy photons depends on the type of collimator (Dobbeleir 1999), but since that is the case for both the photons in the downscatter window and the downscattered photons in the imaging window it is expected that the weighting factor for the downscatter multiplier is more or less independent of the chosen collimator type.
SBR increases typically more than 20% for the healthy subjects, but not statistically significant for the patients due to the low values of SBR. The largely improved SBR for healthy subjects improves discrimination between healthy subjects and patients. The effect of the higher value (compared to one) of the weighting factor on the SBR is not really profound. In healthy subjects with an SBR of approximately 10 the SBR compared to the calculated SBR for k=1 is increased with 0.3 for k=1.1 and 0.6 for k=1.2. The uncertainty in SBR due to the limited amount of counts is approximately 0.1 or less.
Pareto et al (2003) used the difference between Tc-99m and I-123 as a measurement for the high-energy photons in their Monte Carlo calculations. This can in principle also be done in patients, but since the Tc-99m and I-123 contributions needs to be separated and since simultaneous dual isotope imaging is not without problems (El Fakhri 2001) this is difficult to achieve in clinical practice. Two separate scans with the patient in the same position for each isotope would have to be performed.
Contrast might be improved even more by applying a scatter correction for the primary photons, which might be included by one of more energy windows below the imaging window, as in the Dual Energy Window scatter correction for Tc-99m, (14) (later adapted for I-123 by Luo et al (1994)), or Triple Energy Window (TEW) scatter correction (1991). The

TEW correction might however be noise sensitive (Zaidi 2004). An extra complication is the contribution of downscattered photons to the scatter energy window. The weight for the downscatter window needs to be corrected (reduced) in this case, unless theoretical values based on interpolation as in the TEW correction method are used.

5.7.1 Conclusion

Septal penetration of high-energy photons causes a reduced contrast in I-123 SPECT images, if Low Energy collimators are used. A simple and effective way of correcting the raw emission data is to subtract data from a second (higher) energy window. This also improves the data quality for quantitative purposes. The constant factor for multiplication of the second energy window can be determined experimentally for a scanner set-up by using a lead shielded Iodine-123 source, or determined before reconstruction but after data acquisition by minimizing the background in the projection images in subject studies. The weighting factor is as expected slightly higher than one, which is the value expected for a flat downscatter energy spectrum and two energy windows with identical width. After subtraction of the energy windows the raw data can be reconstructed as usual.

Correcting for high energy photons significantly improves the contrast between high and low count regions in the brain (regions of interest and reference regions). In the case of SPECT brain studies of the dopamine transporter with the PE2I tracer, the contrast, measured as specific binding ratio, is improved more than 20% in healthy subjects.

As shown in this study the weighting factor for the high energy window based on the assumption of a flat backscatter energy spectrum is too low, therefore experimental determined weights for the high energy window are preferred. In clinical practice a spatially invariant weighting factor can be used with a value of k=1.1-1.2. However, analysis of the subject data might indicate a slightly higher value of k closer to the subject, i.e. for projection lines through the head.

5.8 Combined scatter and downscatter correction

As mentioned in section 5.7 contrast might even more improved by applying scatter correction for the primary photons. In I-123 SPECT Iodine-123 studies typically 30% of the total amount of counts comes from scattered imaging photons and typically 25% from downscattered high energy photons.
One possibility to correct for scatter is by energy window subtraction. Both the Dual Energy Window (DEW) method as described in Jaszczak(1984) for Tc-99m and the Triple Energy Window (TEW) as described by Ogawa(1991) use this approach. The TEW method has the advantage that it also corrects for high energy downscattered photons. Motomura(1999), Small (2006) and others suggested the subtraction of an energy window with identical width placed just or slightly above the imaging window. A combined approach of DEW with this downscatter correction method (DEW+D) will be described.
All the above methods assume either a flat or a linear downscatter energy spectrum, which is not entirely correct as illustrated in figure 5.1a. The downscattered photons have a broad backscatter peak at 172 keV close to the imaging photons with an energy of 159 keV, see figure 5.1b and Tanaka (2007). Therefore, it is expected that these methods underestimate the contribution of downscattered photons.
An alternative method for the weighting of subtraction energy windows was developed and applied on the TEW method and the novel DEW+D method. The method was tested in a pilot study with a phantom.

5.8.1 Energy window corrections

In general correction methods based on energy subtraction can be formulated as

$$\mathbf{J} = \mathbf{I} - k_1 \cdot \mathbf{W_1} - k_2 \cdot \mathbf{W_2} - \ldots \quad . \tag{5.5}$$

Here **I** is the projection image from the imaging energy window, $\mathbf{W_1}$ and $\mathbf{W_2}$ denote the correction windows, and k_1 and k_2 are the weights for the correction windows. **J** is the resulting corrected projection image, which can be reconstructed as usual.
In the case of the Triple Energy Window (TEW) the scatter and downscatter are approximated by linear interpolation between two

narrow abutting energy windows around the imaging window. The weights, L=low, H=high are in this case given by

$$k_L = \frac{1}{2}\frac{w_I}{w_L} \qquad k_H = \frac{1}{2}\frac{w_I}{w_H}, \tag{5.6}$$

where w indicates the width of the energy windows.
In the Dual Energy Window (DEW) approximation scatter (S) is corrected by subtracting a window with identical width placed in the Compton part of the spectrum just below the imaging window weighted with an empirical value of 0.5 for 20% energy width imaging windows. If a flat downscatter energy spectrum is assumed combining DEW with the subtraction of a downscatter (D) window with equal width yields

$$k_S = 0.5 \qquad k_D = 1. \tag{5.7}$$

However, using these weights is not correct, since the scatter window also contains downscattered photons. To estimate the Compton part (C) without downscatter the scatter window (S) can be corrected with

$$\mathbf{C} = \mathbf{S} - k_{S,D} \cdot \mathbf{D} \qquad \text{with} \qquad k_{S,D} = \frac{w_S}{w_D} = 1, \tag{5.8}$$

resulting in

$$\mathbf{J} = \mathbf{I} - k_S \cdot \mathbf{C} - k_D \cdot \mathbf{D} = \mathbf{I} - k_S \cdot \mathbf{S} - k_D^* \cdot \mathbf{D}$$
$$\text{with} \qquad k_D^* = k_D - k_S k_{S,D} = 1 - 0.5 \cdot 1 = 0.5. \tag{5.9}$$

The scatter multiplier k_S is not affected by the downscatter correction.

5.8.2 Alternative determination of the weights

In the above downscatter correction methods it is assumed that the downscatter energy spectrum is flat (Motomura's downscatter correction method and DEW+D) or is linear (TEW). This is not entirely correct, since the downscattered photons have a broad backscatter peak at 172

keV. This means that weights determined in this way will be too low and not all the downscattered photons are corrected for.
However, there is another experimental way to determine the weights. Keeping the scatter multiplier (k_1 in this case) fixed and demanding that there should be no counts in the background outside the object the window weight can be determined by

$$\mathbf{J} = \mathbf{I} - k_1 \cdot \mathbf{W_1} - k_2 \cdot \mathbf{W_2} = \mathbf{0} \qquad \longrightarrow \qquad k_2 = \frac{\overline{\mathbf{I}} - k_1 \cdot \overline{\mathbf{W_1}}}{\overline{\mathbf{W_2}}}. \quad (5.10)$$

The bar above the images denotes the mean of the pixels in the background outside the object. This equation holds for weights that are not position depended, such as the universal scatter multiplier in DEW and the downscatter weight in section 5.2-5.7.

5.8.3 Measurements

Phantom measurements were made on a 3-headed IRIX camera (Philips Medical, Cleveland) with Low Energy General Purpose (LEGP) parallel hole collimators and an orbit radius of 16.5 cm. The system resolution was 8.4 mm FWHM. Energy windows were set as in table 5.2.

Table 5.2: *Energy window settings in keV.*

Window	Imaging	Scatter	Downscatter	TEW Low	TEW High
Energy (keV)	143.1-174.9	111.3-143.1	184.0-216.0	139.1-143.1	174.9-178.9

In order to minimize the overlap of imaging photons in the downscatter window a small energy gap between these two windows was chosen. Projection data was recorded at 120 angles with an interval of 3 degrees. Reconstruction of images was performed in MATLAB 7.5 (Mathworks) in 128x128 matrices (2.33 mm pixels and identical slice thickness) using standard filtered back projection with a low pass 4th order Butterworth filter at 0.3 Nyquist (=0.64 cm^{-1}), and using Chang's uniform attenuation correction with an attenuation factor of 0.15 cm^{-1} with and 0.10 cm^{-1} without scatter correction. Reconstruction was performed for the imaging window only, named Single Energy Window (SEW), DEW and TEW and with downscatter correction for SEW and DEW.

The cylindrical water filled Perspex phantom of 5.7 liter had an inner diameter of 19 cm and three cylindrical inserts of 0.27 liter each. The cylindrical inserts were filled with 74.5, 49.1 and 0 MBq and the background was filled with 249 MBq I-123. The calculated activity ratio between the two hot spots was 1.52 and the ratio between the hot spots and the background was 5.36 and 3.54. The total amount of counts in the imaging window of the data was approximately 300 million Counts.

5.8.4 Results

The determined weights for the downscatter windows are given in table 5.3. Experimentally determined weights were calculated with equation (5.10) in the same way as shown in figure 5.5a.

***Table 5.3**: Weights of the downscatter windows*

Weighting:	k_H (TEW)	k_D^*	k_D	$k_{S,D}$
Theoretical	3.98	0.50	0.99	0.99
Experimental	4.57	0.82	1.36	1.06

Figure 5.10 shows the reconstructed centre slice for the phantom with a single energy window and with scatter correction with the dual energy window correction. Figure 5.11 shows the triple energy window correction with theoretical and experimentally determined weights. Figure 5.12 shows the Dual Energy Window scatter correction combined with downscatter correction with theoretical and experimentally determined weights.

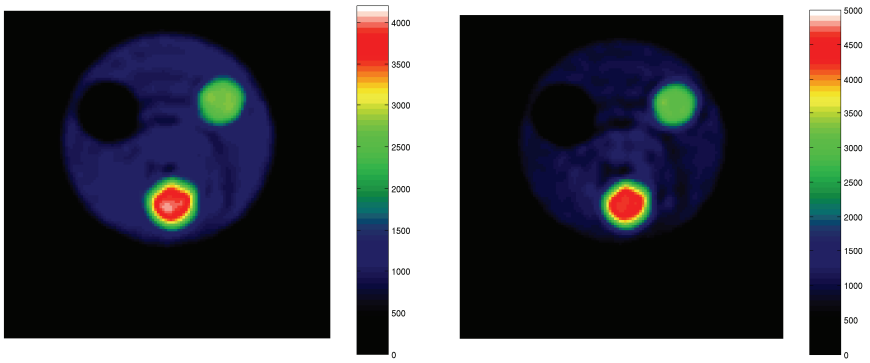

***Figure 5.10**: The reconstructed centre slice of the phantom data. In the left panel no energy window subtraction (SEW) is performed, and in the right panel scatter correction is performed by the dual energy window (DEW) correction.*

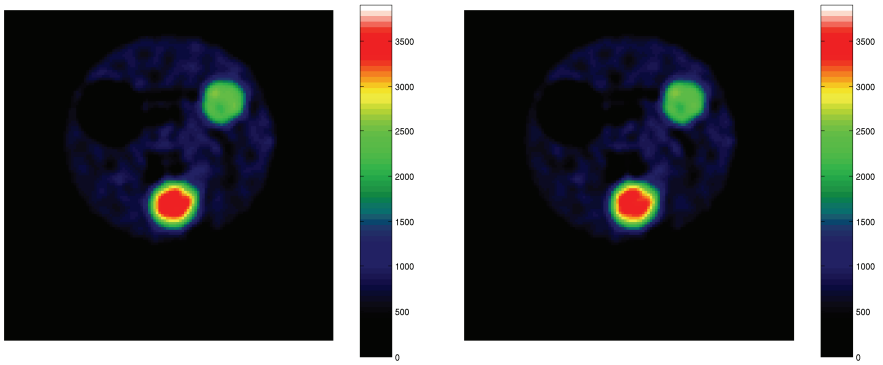

***Figure 5.11**: The reconstructed centre slice of the phantom data with the Triple Energy Window correction. In the left panel with theoretical weights and in the right panel with experimentally determined weights. Note the visible background outside the phantom due to downscattered high-energy photons.*

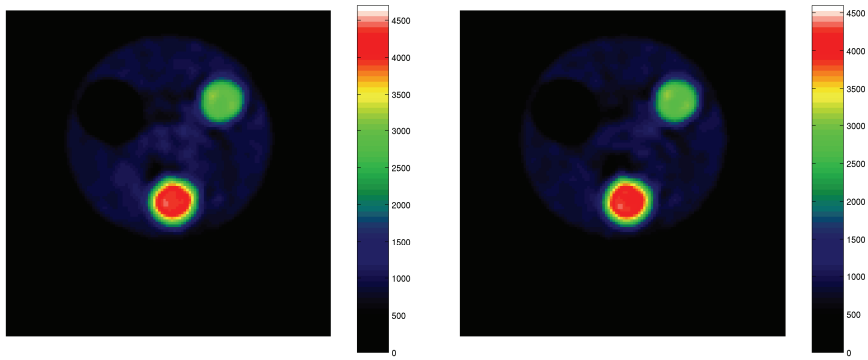

***Figure 5.12**: The reconstructed centre slice of the phantom data with the Dual Energy Window scatter correction combined with downscatter correction. In the left panel with theoretical weights and in the right panel with experimentally determined weights.*

Visual inspection reveals more noise in the images with TEW, otherwise all images in figure 5.11 and figure 5.12 look comparable. Quantitative analysis was performed by determining the ratio between the hotspots and ratio between the hot spots and the background (bg) shown in table 5.4. The ratios were determined by measuring a 1D profile in one slice through the phantom and the centre of the hot spots, where the border of the hot spot was set at the average intensity of the surroundings and the hot spot.

***Table 5.4**: Ratios of the hot spots I, II and the background (bg) for the different methods*

Ratio	true	SEW	SEW+D†	DEW	DEW+D	DEW+D†	TEW	TEW†
I/bg	5.36	3.44	4.10	4.22	4.68	5.07	5.19	5.38
II/bg	3.54	2.37	2.74	2.82	3.10	3.32	3.56	3.68
I/II	1.52	1.45	1.50	1.50	1.51	1.53	1.46	1.46

† indicates experimentally determined weights

5.8.4 Discussion and Conclusions

It was shown that the DEW scatter correction method can be combined with a downscatter correction. Weights for downscatter windows can be experimentally determined and are as expected higher than the theoretical values due the broad peak of backscattered high energy photons close to the energy of the imaging photons. For the TEW-method experimentally a 15% higher weighting factor was found.
Assuming that most of the counts come from the object the total amount of counts after energy window subtraction was 4% and 14% lower after applying the experimentally determined weights for the TEW and DEW+D method, respectively. The difference in the ratio between the hot spots and the background between the theoretical and experimental weights was 3-4% for the TEW method and 7-8% for the DEW+D method. The difference in weights did not influence the ratio between the two hot spots significantly.
The ratios determined by the DEW+D† method are still a bit too low. This might be caused by a too low applied scatter multiplier. Luo(1994) showed that a scatter multiplier of 0.6-0.8 in stead of 0.5 might be appropriate for high activity regions in I-123 studies. Another reason might be that large angle and higher order scattering is included in the broad DEW scatter window, where this is not present in the imaging window. As can be seen from the TEW reconstructed images in figure 5.11 the TEW method introduces even at this high count level extra noise. Therefore the DEW+D method might be preferred, despite that it does not mimic the scattered photons in the imaging window as well.
It is most important to correct for both scatter and downscatter in I-123 SPECT. Depending on the counts statistics the more noise sensitive and more correct TEW method or the less sensitive and less correct DEW+D method can be chosen. The use of experimentally determined weights is a significant improvement for DEW+D, but not for TEW.

CHAPTER 6

Recommendations and Outlook

During the project I discovered an important engineering rule of thumb for the acquisition and processing of medical scanner data:

It is better to correct in an approximately correct way than not to correct.

In this final chapter some recommendations and a future outlook are given.

6.1 Recommendations

In MR SVS not the sum or mean of all acquisitions needs to be stored, but all acquisitions individually. The data can then be analyzed by the user or automated algorithms. A first improvement would be to store both the mean and median, since the difference between these two reveals the presence of outliers, and the median corrects (but not entirely) for outliers.

SPECT scanners should have an automatic way to combine energy window with user defined weights during acquisition. This does not need the user interaction, which is required in the process of scatter and downscatter correction during post-processing, and will remove the hurdle of the intensive post-processing experienced by the users.

6.2 Outlook

Motion correction for MR SVS might be improved more by actually measuring movement of the subject in the MR-scanner. This could be done by three small perpendicular coils which give rise to a voltage, which is proportional to the flux change. The signal of these three coils can be transferred to the acquisition computer in the same way physiological data is sent. In the case of brain studies the three coils can be positioned on the head of the subject. This will also give the possibility to validate the performance of the in this thesis described motion correction algorithms.

As described in this thesis the optimal cut-off frequency depends amongst others on the noise in the SPECT-images. As King (1997) already discovered a different filtering of the energy windows optimizes the trade-off between filtering and image quality. Instead of minimizing the normalized mean squared error (NMSE) the cut off frequencies can be determined in a way based on an understanding of the noise and spectral properties of the images as described in this thesis.

The combination of downscatter and scatter with broad energy windows looks promising in the phantom study, and it will be interesting to see the performance on subject data, and compare this correction with the Triple Energy Window correction.

References

Andersson JLR. How to estimate global activity independent of changes in local activity. Neuroimage. 1977;60:237-44.

Barner KE, Arce GR. Order-statistic filtering and smoothing of time-series: Part II. In: Balakrishnan N, Rao CR, editors. Handbook of Statistics 17: Order Statistics: Applications. Amsterdam, The Netherlands: Elsevier; 1998. p. 555-602.

Bell A, Sejnowski TJ. An Information-Maximization Approach to Blind Separation and Blind Deconvolution. Neural Computation. 1995;7:1129-59.

Bhattacharyya PK, Lowe MJ, Phillips MD. Spectral quality control in motion-corrupted single-voxel J-difference editing scans: an interleaved navigator approach. Magn Reson Med. 2007;58(4):808-12.

Bolan PJ, Henry PG, Baker EH, Meisamy S, Garwood M. Measurement and correction of respiration-induced B0 variations in breast 1H MRS at 4 Tesla. Magn Reson Med. 2004;52(6):1239-45.

Bottomley PA. Spatial localization in NMR spectroscopy in vivo. Ann N Y Acad Sci. 1987;508:333-48.

Chang LT. A method for attenuation correction in radionuclide computed tomography. IEEE Trans Nucl Sci. 1978;25:638–43.

Dammann O, Leviton A. Maternal intrauterine infection, cytokines, and brain damage in the preterm newborn. Pediatr Res. 1997;42(1):1-8.

Danielsen ER, Ross B. Magnetic Resonance Spectroscopy Diagnosis of Neurological Diseases. Marcel Dekker, Inc. New York, 1999

Dobbeleir AA, Hambye AS, Franken PR. Influence of high-energy photons on the spectrum of iodine-123 with low- and medium-energy collimators: consequences for imaging with 123I-labelled compounds in clinical practice. Eur J Nucl Med. 1999;26(6):655-8.

Drost DJ, Riddle WR, Clarke GD. Proton magnetic resonance spectroscopy in the brain: report of AAPM MR Task Group #9. Med Phys. 2009;29(9):2177-97. Review.

Du Y, Tsui BM, Frey EC. Model-based compensation for quantitative 123I brain SPECT imaging. Phys Med Biol. 2006;51(5):1269-82.

El Fakhri G, Moore SC, Maksud P, Aurengo A, Kijewski MF. Absolute activity quantitation in simultaneous 123I/99mTc brain SPECT. J Nucl Med. 2001;42(2):300-8.

Felblinger J, Kreis R, Boesch C. Effects of physiologic motion of the human brain upon quantitative 1H-MRS: analysis and correction by retro-gating. NMR Biomed. 1998;1(3):107-14.

Frahm J, Merboldt KD, Hänicke W. Localized Proton Spectroscopy Using Stimulated Echoes. J Magn Reson. 1987;72(3):502-8.

Gabr RE, Sathyanarayana S, Schär M, Weiss RG, Bottomley PA. On restoring motion-induced signal loss in single-voxel magnetic resonance spectra. Magn Reson Med. 2006;56(4):754-60.

Hansen LK, Larsen J, Kolenda T. Blind detection of independent dynamic components. In Proceedings of IEEE International Conference on Acoustics, Speech, and Signal Processing (ICASSP), Salt Lake City, Utah, USA, 2001. p. 3197-3200.

Hanson LG, Is Quantum Mechanics necessary for understanding Magnetic Resonance? Concepts Magn Reson A. 2008;32A(5);329-40.

Helms G, Piringer A. Restoration of motion-related signal loss and line-shape deterioration of proton MR spectra using the residual water as intrinsic reference. Magn Reson Med. 2001;46(2):395-400.

Hyvärinen A, Oja E. Independent component analysis: algorithms and applications. Neural Netw. 2000;13:411-30.

Højen-Sørensen P, Hansen LK, Winther O. Mean Field Implementation of Bayesian ICA. In proceedings of the 3rd International Conference on Independent Component Analysis and Blind Signal Separation, San Diego, USA, 2001. p. 439-44.

Inder TE, Warfield SK, Wang H, Hüppi PS, Volpe JJ. Abnormal cerebral structure is present at term in premature infants. Pediatrics. 2005;115(2):286-94.

Jansen JF, Backes WH, Nicolay K, Kooi ME. 1H MR spectroscopy of the brain: absolute quantification of metabolites. Radiology. 2006;240(2):318-32. Review.

Jaszczak RJ, Greer KL, Floyd CE Jr, Harris CC, Coleman RE. Improved SPECT quantification using compensation for scattered photons. J Nucl Med. 1984;25(8):893-900.

Katz-Brull R, Lenkinski RE. Frame-by-frame PRESS 1H-MRS of the brain at 3 T: the effects of physiological motion. Magn Reson Med. 2004;51(1):184-7.

Katz-Brull R, Rofsky NM, Lenkinski RE. Breathhold abdominal and thoracic proton MR spectroscopy at 3T. Magn Reson Med. 2003;50(3):461-7.

Kenney JF, Keeping ES. The Median, §13.13 In: Mathematics of Statistics, Pt. 1, 3rd ed. Princeton, NJ: Van Nostrand; 1962. p. 211.

King MA, de Vries DJ, Pan TS, Pretorius PH, Case JA. An Investigation of the filtering of TEW Scatter Estimates used to Compensate for Scatter with ordered Subset Reconstructions. Trans Nucl Sci. 1997;44(3):1140-5.

Klose U, In vivo proton spectroscopy in presence of eddy currents. Magn Reson Med. 1990;14(1):26-30.

Kobayashi H, Momose M, Kanaya S, Kondo C, Kusakabe K, Mitsuhashi N. Scatter correction by two-window method standardizes cardiac I-123 MIBG uptake in various gamma camera systems. Ann Nucl Med. 2003;17(4):309-13.

Kocher DC. Radioactive Decay Data Tables. Report DOE/TIC-11026: Technical Information Center, U.S. Department of Energy, Washington, D.C.; 1981

Koikkalainen J, Hirvonen J, Nyman M, Lötjönen J, Hietala J, Ruotsalainen U. Shape variability of the human striatum--Effects of age and gender. Neuroimage. 2007;34(1):85-93.

Kolenda T, Hansen LK, Larsen J. Signal detection using ICA: application to chat room topic spotting. In proceedings of the 3rd International Conference on Independent Component Analysis and Blind Signal Separation, San Diego, USA, 2001. p. 540-5.

Krane KS. Introductory Nuclear Physics, John Wiley & sons, Inc. 1988

Lange K Carson R. EM reconstruction algorithms for emission and transmission tomography. J Comput Assist Tomogr. 1984;8(2):306–16.

Luo JQ, Koral KF. Background-adaptive dual-energy-window correction for Compton scattering in SPECT. Nucl Instr and Meth in Phys Res A. 1994;353:340-3.

Mewes AU, Hüppi PS, Als H, Rybicki FJ, Inder TE, McAnulty GB, Mulkern RV, Robertson RL, Rivkin MJ, Warfield SK. Regional brain development in serial magnetic resonance imaging of low-risk preterm infants. Pediatrics. 2006;118(1):23-33.

Miller RG. The JackKnife--A review. Biometrika. 1974;61(1):1-15.

Motomura N, Ichihara T, Takayama T, Aoki S, Kubo H, Takeda K. [Practical compensation method of downscattered component due to high energy photon in 123I imaging]. Kaku Igaku. 1999;36(9):997-1005. Japanese.

Nilsson H, Optimization of Sequence Parameters TE and TM to Detect and Separate Glutamate and Glutamine by Localized in vivo Magnetic Resonance Spectroscopy (MRS), Diploma Thesis in Physical Chemistry, MR Research Centre, Department of Clinical Neuroscience, Karolinska Institutet, 2002

Ogawa K, Harata Y, Ichihara T, Kubo A, Hashimoto S. A practical method for position-dependent Compton-scatter correction in single photon emission CT. IEEE Trans Med Imaging. 1991;10(3):408-12.

Pareto D, Cot A, Pavia J, Falcon C, Juvells I, Lomena F, Ros D. Iterative reconstruction with correction of the spatially variant fan-beam collimator response in neurotransmission SPET imaging. Eur J Nucl Med Mol Imaging. 2003;30(10):1322-9.

Pfeuffer J, Juchem C, Merkle H, Nauerth A, Logothetis NK High-field localized 1H NMR spectroscopy in the anesthetized and in the awake monkey. Magn Reson Imaging. 2004;22(10):1361-72.

Pinborg LH, Ziebell M, Frøkjaer VG, de Nijs R, Svarer C, Haugbøl S, Yndgaard S, Knudsen GM. Quantification of 123I-PE2I binding to dopamine transporter with SPECT after bolus and bolus/infusion. J Nucl Med. 2005;46(7):1119-27.

Radon JKA. Über die Bestimmung von Funktionen durch ihre Integralwerte langs gewisser Mannigfaltigkeiten. *Berichte Sachsische Akademie der Wissenschaften*. 1917;69:262-7.
Note: The title roughly translates to: “On the determination of functions by the integrals along certain manifolds”.

Ramachandran GN, Lakshminarayanan AV, Three-dimensional reconstruction from radiographs and electron micrographs: applicstions of convolutions instead of Fourier transforms. Proc Natl Acad Sci USA. 1971;68:2236-40.

Rider PR. Variance of the Median of Small Samples from Several Special Populations. J. Amer. Statist. Assoc. 1960;55:148-50.

Robertson NJ, Kuint J, Counsell TJ, Rutherford TA, Coutts A, Cox IJ, Edwards AD. Characterization of cerebral white matter damage in preterm infants using 1H and 31P magnetic resonance spectroscopy. J Cereb Blood Flow Metab. 2000;20(10):1446-56.

Seibert JA, Boone JM. X-ray imaging physics for nuclear medicine technologists. Part 2: X-ray interactions and image formation. J Nucl Med Technol. 2005;33(1):3-18.

Shanbhag DD, Dunham SA, Knight-Scott J. A water signal based navigation echo for localized MRS In Proceedings of the 13th Annual Meeting of ISMRM, Miami Beach, Florida, USA, 2005. p. 2505.

Shepp LA, Vardi Y. Maximum likelihood reconstruction for emission tomography. IEEE Trans Med Imaging. 1982;1(2):113-22.

Shiga T, Kubo N, Takano A, Kobayashi J, Takeda Y, Nakamura F, Katoh C, Koyama T, Tsukamoto E, Tamaki N. Which attenuation coefficient to use in combined attenuation and scatter corrections for quantitative brain SPET? Eur J Nucl Med Mol Imaging. 2002;29(7):969-70.

Skimminge A, Markenroth K, Hejl A, Hanson LG. Improved spectroscopy using cluster analysis and lipid signals as a motion indicator. In Proceedings of the 11th Annual Meeting of ISMRM, Toronto, Ontario, Canada, 2003. p. 270.

Slotboom J, van Ormondt D, Brekenfeld C, Nirkko A, Schroth G. The usage of median filtering for the elimination of patient motion related signal artifacts in single voxel spectroscopy. In Proceedings of the 22nd Annual Scientific Meeting of ESMRB, Basle, Switzerland, 2005. p. 124-5.

Slotboom J, van Ormondt D. Elimination of Patient-Motion Artefacts in In Vivo MR Spectroscopy. In Proceedings of ProRISC, IEEE Benelux, Veldhoven, The Netherlands, 2006. p. 204-7.

Slotboom J, Nirkko A, van Ormondt D. A Comparison of Time Domain and Frequency Domain All Rank Selection Order Statistics Filtering (ARSOS) of Single Voxel 1H MRS-signals. In Proceedings of the 15th Annual Meeting of ISMRM, Berlin, Germany, 2007a. p. 203.

Slotboom J , van Ormondt D. The Effect of Order-Statistics Filtering on the Output Probability Density Functions. In Proceedings of ProRISC, IEEE Benelux, Veldhoven, The Netherlands, 2007b. p. 254-8.

Small AD, Prosser J, Motherwell DW, McCurrach GM, Fletcher AM, Martin W. Downscatter correction and choice of collimator in 123I imaging. Phys Med Biol. 2006;51(17):N307-11.

Sorenson JA. Methods for quantitative measurement of radioactivity in vivo by whole-body counting. In: Hine GJ, Sorenson JA, editors. Instrumentation in Nuclear Medicine, Volume 2, Academic Press, New York, 1974. p. 311-48.

Tanaka M, Uehara S, Kojima A, Matsumoto M. Monte Carlo simulation of energy spectra for 123I imaging. Phys Med Biol. 2007:52;4409-25.

Thiel T, Czisch M, Elbel GK, Hennig J. Phase coherent averaging in magnetic resonance spectroscopy using interleaved navigator scans: compensation of motion artifacts and magnetic field instabilities. Magn Reson Med. 2002;47(6):1077-82.

Thomsen G, de Nijs R, Hogh-Rasmussen E, Frokjaer V, Svarer C, Knudsen GM. Required time delay from (99m)Tc-HMPAO injection to SPECT data acquisition: healthy subjects and patients with rCBF pattern. Eur J Nucl Med Mol Imaging. 2008;35(12):2212-19.

Tossici-Bolt L, Hoffmann SM, Kemp PM, Mehta RL, Fleming JS. Quantification of [123I]FP-CIT SPECT brain images: an accurate technique for measurement of the specific binding ratio. Eur J Nucl Med Mol Imaging. 2006;33(12):1491-9.

Webb S. The Physics of Medical Imaging. IOP Publishing Ltd, 1998

Zaidi H, Koral KF. Scatter modelling and compensation in emission tomography. Eur J Nucl Med Mol Imaging. 2004;31(5):761-82. Review.

Zeng GL, Gullberg GT. Can the backprojection filtering algorithm be as accurate as the filtered backprojection algorithm? Nuclear Science Symposium and Medical Imaging Conference IEEE Conference Record 1994;3:1232-6.

Zhu G, Gheorghiu D, Allen PS. Motional degradation of metabolite signal strengths when using STEAM: a correction method. NMR Biomed. 1992;5(4):209-11.

Ziebell M, Thomsen G, Knudsen GM, de Nijs R, Svarer C, Wagner A, Pinborg LH. Reproducibility of [123I]PE2I binding to dopamine transporters with SPECT. Eur J Nucl Med Mol Imaging. 2007;34(1):101-9.

APPENDIX A

Mean, median, variance

A.1 The influence of one sample on the median

The median $\tilde{x}$ is defined by the value of x where the cumulative distribution function D is $1/2$, which states that exactly half of the samples has a lower value than the median. The influence of one sample on the value of D is $1/2n$. This gives the possibility the approximate the influence of one sample on the median for large n with

$$\frac{dD(\tilde{x})}{dx} \cdot \Delta\tilde{x} \approx \frac{1}{2n} \qquad \longrightarrow \qquad \Delta\tilde{x} = \frac{1}{2np(\tilde{x})}, \tag{A.1}$$

where the derivative of the cumulative probability distribution is replaced by the probability (density) function.

A.2 The expected difference between mean and median

The expected squared difference of mean and median is given by

$$\begin{aligned} &< (\bar{x} - \tilde{x})^2 >=< \bar{x} - \tilde{x} >^2 + \mathrm{var}(\bar{x} - \tilde{x}) = \\ &=< \bar{x} - \tilde{x} >^2 + \mathrm{var}(\bar{x}) + \mathrm{var}(\tilde{x}) - 2 \cdot \mathrm{cov}(\bar{x}, \tilde{x}). \end{aligned} \tag{A.2}$$

The covariance between mean and median can be calculated with

$$\mathrm{cov}(\bar{x}, \tilde{x}) = \sum_i \Delta\bar{x}_i \Delta\tilde{x}_i \approx \frac{< |x| >}{2np(\tilde{x})}, \tag{A.3}$$

where $\Delta\bar{x}_i$ and $\Delta\tilde{x}_i$ are defined and approximated for large n by equations (3.1) and (3.2). For distributions with the same expectation value for mean and median and large n the expectation value of the squared difference between mean and median is given by

$$< (\bar{x} - \tilde{x})^2 >\approx \frac{1}{n} \cdot \left(\mathrm{var}(x) + \frac{1}{4p^2(\tilde{x})} - \frac{< |x| >}{p(\tilde{x})} \right), \tag{A.4}$$

where the variance of the median is approximated by equation (3.3).

APPENDIX B

Publications

B.1 Peer reviewed articles

de Nijs R, Holm S, Thomsen G, Ziebell M, Svarer C.
Experimental determination of the weighting factor for the energy window subtraction based downscatter correction for I-123 in brain SPECT-studies.
J Med Phys. 2010:**35**(4):215-22.

Ziebell M, Pinborg LH, Thomsen G, de Nijs R, Svarer C, Wagner A, Knudsen GM.
MRI-guided region-of-interest delineation is comparable to manual delineation in dopamine transporter SPECT quantification in patients: a reproducibility study.
J Nucl Med Technol. 2010;**38**(2):61-8.

de Nijs R, Miranda MJ, Hansen LK, Hanson LG.
Motion correction of Single Voxel Spectroscopy by Independent Component Analysis applied to spectra from non-anesthetized pediatric subjects.
Magn Reson Med. 2009;**62**(5):1147-54.

Sardanelli F, Fausto A, Di Leo G, de Nijs R, Vorbuchner M, Podo F.
In vivo proton MR spectroscopy of the breast using the total choline peak integral as a marker of malignancy.
AJR Am J Roentgenol. 2009;**192**(6):1608-17.

Thomsen G, de Nijs R, Hogh-Rasmussen E, Frokjaer V, Svarer C, Knudsen GM.
Required time delay from (99m)Tc-HMPAO injection to SPECT data acquisition: healthy subjects and patients with rCBF pattern.
Eur J Nucl Med Mol Imaging. 2008;**35**(12):2212-9.

Frokjaer VG, Pinborg LH, Madsen J, de Nijs R, Svarer C, Wagner A, Knudsen GM.
Evaluation of the Serotonin Transporter Ligand 123I-ADAM for SPECT Studies on Humans.
J Nucl Med. 2008;**49**(2):247-54.

Ziebell M, Thomsen G, Knudsen GM, de Nijs R, Svarer C, Wagner A, Pinborg LH.
Reproducibility of [123I]PE2I binding to dopamine transporters with SPECT.
Eur J Nucl Med Mol Imaging. 2007;**34**(1):101-9.

Pinborg LH, Ziebell M, Frokjaer VG, de Nijs R, Svarer C, Haugbol S, Yndgaard S, Knudsen GM.
Quantification of 123I-PE2I binding to dopamine transporter with SPECT after bolus and bolus/infusion.
J Nucl Med. 2005;**46**(7):1119-27.

B.2 Accepted Abstracts

de Nijs R, Miranda MJ, Hanson LG.
Metabolite ratios in the brain of prematurely born infants determined by short and intermediate echo time single voxel proton spectroscopy at 3 Tesla.
Research day Hvidovre Hospital 2009, Copenhagen University Hospital

Miranda MJ, de Nijs R, Hanson LG.
Metabolite ratios in the brain of prematurely born infants at 3T SVS.
European Society of Magnetic Resonance in Neuropediatrics 9th congress 2007 (abstract T04)

de Nijs R, Miranda MJ, Hanson LG.
Significant changes in metabolite ratios in the brain of prematurely born infants determined by long echo time single voxel proton spectroscopy at 3 Tesla.
Proc Annu Meet Eur Soc Magn Reson Med Biol 2006, 135

de Nijs R, Hanson LG.
Motion correction of Single Voxel Spectroscopy by Independent Component Analysis.
Proc Annu Meet Eur Soc Magn Reson Med Biol 2005, 228

de Nijs R, Svarer C.
Determination of the weights of downscatter windows in I-123 SPECT studies.
Eur J Nucl Med Mol Imaging 2007;**34**(S2) ;p.346

de Nijs R, Svarer C.
Combined backscatter and scatter correction for low count I-123 SPECT studies.
J Nucl Med 2007;**48**(S1); p.424

Thomsen G, de Nijs R, Hogh-Rasmussen E, Frokjaer VG, Svarer C, Knudsen GM.
Thirty minutes delay between 99mTc-SHMPAO injection and SPET data acquisition is sufficient.
J Nucl Med 2006;**47**(S1): p.208

de Nijs R, Svarer C.
Correction of high energy photons and scatter for dynamic SPECT studies with I-123.
Eur J Nucl Med Mol Imaging 2005;**32**(S1), p. 259

de Nijs R, Svarer C, Holm S.
High energy photon correction for I-123 in SPECT studies.
Eur J Nucl Med Mol Imaging 2004;**31**(S1), p. 402

Magnetic Resonance in Medicine 62:1147–1154 (2009)

Motion Correction of Single-Voxel Spectroscopy by Independent Component Analysis Applied to Spectra From Nonanesthetized Pediatric Subjects

Robin de Nijs,[1,2] Maria J. Miranda,[1,3] Lars Kai Hansen,[4] and Lars G. Hanson[1]

For single-voxel spectroscopy, the acquisition of the spectrum is typically repeated *n* times and then combined with a factor $\sqrt{n}$ in order to improve the signal-to-noise ratio. In practice, the acquisitions are not only affected by random noise but also by physiologic motion and subject movements. Since the influence of physiologic motion such as cardiac and respiratory motion on the data is limited, it can be compensated for without data loss. Individual acquisitions hampered by subject movements, on the other hand, need to be rejected if no correction or compensation is possible. If the individual acquisitions are stored, it is possible to identify and reject the motion-disturbed acquisitions before averaging. Several automatic algorithms were investigated using a dataset of spectra from nonanesthetized infants with a gestational age of 40 weeks. Median filtering removed most subject movement artifacts, but at the cost of increased sensitivity to random noise. Neither independent component analysis nor outlier identification with multiple comparisons has this problem. These two algorithms are novel in this context. The peak height values of the metabolites were increased compared to the mean of all acquisitions for both methods, although primarily for the ICA method. Magn Reson Med 62:1147–1154, 2009. © 2009 Wiley-Liss, Inc.

Key words: single-voxel spectroscopy; motion correction; ICA; proton spectroscopy; outlier detection

Subject movement during consecutive single-voxel spectroscopy acquisitions is often not detected, and the resulting distorted data affect the outcome measures. Since severe patient movements, as present, for instance, in single-voxel spectroscopy of nonanesthetized pediatric patients and psychiatric and demented patients, cause significant deterioration in spectra, they should not be ignored. For example, movements may introduce a bias in a comparative study between patients and healthy controls. Despite its significance, the issue of identifying motion-distorted spectra, in contrast to motion correction and compensation, is quite unexplored and often not mentioned (1,2).

Compensation for spectra that are potentially affected by physiologic motion can be performed by cardiac and respiratory gating (3) and/or breath-holding techniques (4). Since disturbances in phase and frequency by physiologic motion are limited (5), they can be compensated for by phase correcting the individual acquisitions before averaging, a process known as phase coherent or constructive averaging (6), followed by frequency-shift correction (7,8). However, these techniques can potentially introduce a bias caused by differences in noise between subjects. A bias toward increased phase reference signals may also result.

Severe patient movement cannot be compensated for, and the acquisitions distorted by patient motion need to be identified and rejected. Motion can be tracked by a water-signal–based navigator (9) or an interleaved navigator scan (10). Especially J-difference editing is sensitive to motion artifacts, and it was shown that the interleaved navigator scan is sufficient (11).

However, a navigator scan is not necessarily needed since the single voxel spectra of the consecutive acquisitions reveal information of the subject's movement. The motion-distorted acquisitions seem easy to identify visually, but commonly used "objective" rejection criteria are typically based on the position, amplitude, and width of the suppressed water peak and an arbitrary threshold (12). Alternatively, a cluster analysis of the lipid signals can be used to correct for subject motion (13), but a lipid signal might not always be present.

In practice, motion correction consists of two steps. First, the acquisitions severely deteriorated by subject movements need to be identified and excluded. Second, the remaining acquisitions need to be frequency shifted and phase corrected individually (12).

Movements during an individual acquisition, and severe movements between acquisitions, may corrupt the entire spectrum of the acquisition irreversibly. Limited movement between individual acquisitions will introduce a simultaneous broadening and lowering of the peak in the mean spectrum, keeping the area under the peak approximately constant. This can affect the output of the fitting procedure if peak shapes are assumed. Movement can also result in a different location of the measured volume, which additionally can cause an error in metabolite concentrations if these vary with position. There can be a difference between the group of patients and the healthy controls regarding unrecoverable subject movements. The patient data might suffer more from subject movements, and if no movement compensation is performed, this will cause a systematic underestimation of metabolites in this group and thus introduce a bias in the study (7).

Corrections primarily have to ensure robust positioning of the measured volume while keeping the signal free of motion-induced bias and secondarily keeping the noise

[1]Danish Research Centre for Magnetic Resonance, Hvidovre, Denmark
[2]Neurobiology Research Unit, Copenhagen, Denmark
[3]Department of Pediatrics, Copenhagen University Hospital Hvidovre, Denmark
[4]Technical University of Denmark, Department of Informatics and Mathematical modeling, Lyngby, Denmark
*Correspondence to: Robin de Nijs, Danish Research Centre for Magnetic Resonance, Department of MR, Section 340, Copenhagen University Hospital Hvidovre, Kettegaard Allé 30, DK-2650 Hvidovre, Denmark. E-mail: rdenijs@drcmr.dk

Received 3 November 2008; revised 29 May 2009; accepted 2 June 2009.
DOI 10.1002/mrm.22129
Published online 24 September 2009 in Wiley InterScience (www.interscience.wiley.com).

low and the signal-to-noise ratio (SNR) as high as possible. SNR is typically increased compared to conventional averaging by phase-coherent averaging (14) and also potentially by outlier rejection techniques due to the unwanted contributions to the motion-distorted signal.

Here, subject movement is demonstrated to be a severe problem for nonanesthetized infants. Several algorithms for identifying and rejecting motion-corrupted spectra were implemented and compared.

MATERIALS AND METHODS

Subjects and Data Acquisition

Subjects were infants born at the Copenhagen University Hospital, Hvidovre, Denmark, and taking part in a MRI/magnetic resonance spectroscopy–preterm infant cohort study. The study includes data from 97 infants, 77 preterm infants (prematurely born between 12 and 6 weeks before term) and 20 controls (born at term). All infants were MR scanned around term or term-equivalent age and were not anesthetized before or during scanning. The local ethics committee accepted the study, and informed parental consent was obtained in all cases.

MR scanning was performed on a Magnetom Trio 3-T scanner (Siemens, Erlangen, Germany) with a quadrature single-channel head coil. An 8-mL cubic voxel was placed in the posterior periventricular white matter, by the posterior horn of the lateral ventricles, and a 3.4-mL cubic voxel was placed at the level of the basal ganglia and thalami, both randomly positioned in the right or left hemisphere. For each voxel position, 48 free induction decay signals based on two phase-cycled averages, each with 1024 complex points and a readout period of 850 ms, were acquired with a point resolved spectroscopy sequence (15) for two echo times (30 and 144 ms) with a repetition time of 2 s.

For every subject, four datasets of 48 repetitions each were acquired for the two different voxels and the two echo times. In order to investigate the effect of subject movement under more controlled conditions, a healthy volunteer was scanned with the same sequences with 30-ms echo time and same position and size of the 8-mL cubic voxel. The complete measurement of the volunteer with 48 acquisitions was repeated three times. The volunteer was instructed to lie motionless during the acquisition of the first dataset and instructed through the intercom to move his head a few centimeters to the left and right for a few seconds approximately at every 16th acquisition of the last two datasets.

Datasets where all 48 repetitions contained severely corrupted measurements, or where water suppression failed, were excluded from this comparative study after visual inspection of the spectrogram. This resulted in 130 datasets (64 with long echo time) for an 8-mL voxel and 113 datasets (56 with long echo time) for a 3.4-mL voxel. From the 130 datasets with an 8-mL voxel and from the 113 datasets with a 3.4-mL voxel size, 30 and 26 datasets, respectively, originated from term infants. The resulting mean or median spectra are zero-order phase corrected and filtered with a first-order gaussian low-pass filter with a full width at half maximum of 1 Hz. Spectra were frequency adjusted based on the position of the N-acetyl aspartate, creatine, and choline peaks, at 2.02 ppm, 3.04 ppm and 3.24 ppm, respectively. Phase-coherent averaging was not applied.

Since the motion-distorted acquisitions are visible as shifts in the frequency domain, it is natural to perform the motion rejection in this domain. It is also possible to carry out the analysis on the free induction decay signal in the time domain (16), but this has not been done in this study.

The performance of three classes of subject-movement-rejection algorithms was investigated: (1) simple median filtering, which provides a more robust but more noise-sensitive estimate than mean filtering; (2) an outlier identification (OI) algorithm with and without multiple comparisons; and (3) independent component analysis (ICA), where the main component represents the spectrum least affected by motion. Corrections as described in the introduction (6,7,10,14) were not performed. Focus was on identification and rejection of the corrupted acquisitions within a dataset.

Mean and Median Filtering

In the conventional way of data processing, all spectra are averaged permitting motion-distorted acquisitions to degrade the final spectrum. One way of dealing with this problem is to reduce the influence of outliers by median filtering (17,18). Instead of using the mean as a signal estimator, the median is used, and this provides a more robust estimate. The mean minimizes the expectation value of the squared deviation, i.e., the variance, while the median minimizes the expectation value of the absolute deviation. This means that the influence of outliers is reduced. An appealing property of the median is that the shift does not depend on the numerical value of the outlier; only the position of the median in the list of ordered samples is shifted half a position. In the case of an even number of outliers symmetrically spread around the true mean value, the shift is even cancelled.

The noise N is defined as the standard deviation (SD) of the signal estimator. For a dataset x_i with n samples, mean $\bar{x}$, median $\tilde{x}$, SD σ and probability function $p(x)$ the noise is given by

$$N^2_{\text{mean}} = \frac{\sigma^2}{n},$$

$$N^2_{\text{median}} \approx \frac{1}{4 \cdot n \cdot p^2(\tilde{x})} = c^2 \cdot N^2_{\text{mean}}, \qquad [1]$$

where c is the efficiency of the mean relative to the median, which is $\sqrt{\pi/2}$ and $\sqrt{3}$ for a normal distribution and uniform distribution, respectively. The approximation of the noise for the median holds for large sample sizes with an arbitrary probability function (19,20). The probability function of the median is normally distributed for any probability function of the samples. Median filtering (together with minimum and maximum filtering) is a well-known type of order-statistics filtering (21).

Since spectra are complex, the average and the median of both the real and imaginary part were calculated separately.

Outlier Identification

Outliers can be identified and excluded by an approximation of the SD and a *t* test. Performing this OI and rejection for every single frequency (pointwise OI) will reduce the contribution of outliers. In this context, a novel alternative is to reject a whole acquisition, if only one Fourier component is identified as an outlier (OI). It is assumed that the acquisitions without outliers are normally distributed. The significance level *P* for the first method was arbitrarily chosen at 5% double sided, i.e., $z_{max} = 1.96$, where *z* is the *z*-score, which is defined by the difference from the mean measured in the number of SDs. The significance level for the second method is corrected for multiple comparisons and this was arbitrarily chosen at 10% (double sided) divided by the number of data points (= 1024) for one acquisition, i.e., $z_{max} = 3.9$. Since the outliers were included in the calculation of the SD, the procedure needs to be repeated in an iterative fashion. The first (crude) estimation of the outlier-free signal is given by the mean and the SD of all samples x_i. The next estimates, denoted x^* with iteration number *j* are calculated in an iterative fashion (22) with

$$x^*_{j+1} = \bar{x} \quad \text{and}$$
$$\sigma^2_{j+1} = \overline{(x^*_{j+1} - x_i)^2} \quad \text{for all } x_i \quad \text{with } |x_i - x^*_j| < z_{max} \cdot \sigma_j, \quad [2]$$

until convergence is reached. An iterative *t* test has never been applied before in this context, but the idea behind the method is similar to the iterative f-test algorithm described by Andersson (23).

Independent Component Analysis

ICA supplies a mathematical framework for analysis of a group of acquisitions. The method (24) is implemented as a toolbox (25,26) in Matlab (Mathworks). ICA is a set of methods for blind signal separation, each method sharing the assumption that two arbitrary components are statistically independent (27). Blind signal separation refers to the common situation in signal processing, in which we aim to separate unknown source signals from an unknown mixture. Another way of describing or defining ICA is by minimizing the mutual information between the components.

With index *i* denoting the acquisition number, and the index *j* denoting the component number, the dataset consisting of *n* acquisitions $x_i(t)$ is described by *M* components $s_j(t)$ with coefficients a_{ij} with

$$x_i(t) = \sum_{j=1}^{M} a_{ij} \cdot s_j(t) + \text{noise}. \quad [3]$$

Since the ICA algorithm only works for real signals, the complex spectrum is transformed into a real signal by adding the imaginary amplitude spectrum behind the real spectrum. An important complication that often arises in practical applications is that the number of components *M* is unknown. Using a bayesian ICA formulation, this problem can be solved in the limit of many acquisitions (28,29). The bayesian information criterion selects the number of components by estimating the probability of the model containing *M* components given the observed data $p(M)$, where the number of components is varied in a range from 1 to M_{max} (the maximum number of components was set to 12). The signal variance not accounted for by the *M* components is assumed to be contributed by an additive, normal, independent, identically distributed, white-noise signal component (the bayesian information criterion selection of the number of components is included in the toolbox (26)). Checks are performed to see if the probability for the number of components is less than 50%.

In the case of a dataset without distorted spectra, ICA will find one component representing the underlying spectrum. The difference between the spectra reconstructed with this component and the measured spectra equals the noise as identified by the ICA algorithm.

If the ICA algorithm finds more than one component, the independent component representing the undistorted spectrum needs to be identified, since ICA does not assign a clear meaning to its components. The dominant component of every single acquisition is determined, and the acquisitions with the dominant component equal to the most frequent dominant component (the main component) for all acquisitions are considered to be a measurement of the undistorted spectrum. No arbitrary thresholds need to be set. The ICA method produces three spectra: (1) the mean of the selected acquisitions, (2) the mean of the selected acquisitions reconstructed with *M* independent components, and (3) the mean of the selected acquisitions reconstructed with only the main independent component. The latter spectrum corresponds to the scaled main independent component. The application of ICA and the identification of the nondistorted ICA component are novel in this context.

Noise and SNR Analysis

In principle, noise can be estimated at one frequency by determining the SD of the selected acquisitions and dividing by the square root of the number of acquisitions. Possibly only few acquisitions may be left, and this will make this noise estimation unreliable. However this is not a problem with the datasets used as completely corrupted data were excluded. Noise will be underestimated, however, since the SD is minimized for the OI methods. This is most prominent for the algorithm without connection between the Fourier components (the frequency direction). The ICA method does not have this problem, but the independent components have a lower noise than the original acquisitions. For ICA, the noise at each particular frequency can be determined by resampling with the Jack-Knife (30) method, but in order to aid comparison an identical noise estimation procedure for all motion-rejection algorithms is preferred. Since there are no metabolite signals between 8 and 9 ppm, this part of the spectrum is used for estimating the noise. The SD of the final signal is determined over this frequency range, which does not depend on the number of selected acquisitions. It is assumed that the signal is constant in this part of the spectrum and that the noise is independent of frequency.

For the SNR and signal analysis, the signal is regarded as the peak height of the three main metabolite peaks, N-

acetyl aspartate at 2.02 ppm, creatine at 3.04 ppm, and choline at 3.24 ppm. Both mean peak height and average SNR of these three peaks were calculated for each dataset. In order to be able to compare between subjects, both signal and SNR were normalized by the values for the mean filtered signal. The algorithm with both the highest signal and highest SNR is considered as the optimal algorithm. Since position change is a source of erroneous measurements and causes simultaneous broadening and lowering of peaks, the area under the metabolite peak is not a proper measure of the quality of the measurement.

Acceptance percentage for each algorithm and each dataset was defined by the number of single data points that were not rejected by the algorithm as a percentage of the total number of data points. The total number of data points equals the number of repetitions times the number of Fourier components.

RESULTS

The first dataset of the healthy volunteer had 48 comparable spectra and the ICA algorithm found only one component, as is expected for a dataset without motion. The effect of (instructed) motion on the other two datasets of the volunteer was comparable. Figure 1 shows the spectrogram (top panel) and the coefficients for the components (bottom panel) of the second dataset, where the healthy volunteer was instructed to move his head at certain times. The influence of head movement is clearly seen in the spectrogram, and ICA components describe the different periods. A typical result for measurement of a preterm infant that has been hampered by motion is shown in Figs. 2 to 6. The top panel in Fig. 2 shows the spectrogram for short echo time, and the bottom panel shows the coefficients for the components in the ICA algorithm. Figs. 3 and 4 show the final spectra between 2.8 and 3.5 ppm for all algorithms for an 8-mL voxel with short echo time (Fig. 3) and long echo time (Fig. 4). Figure 5 shows the entire short-echo-time spectrum. The noise is estimated from the signal between 8 and 9 ppm, since there are no metabolite signals there. Fig. 6 shows the short-echo-time spectrum around the residual water peak and the removal of a water peak erroneously displaced by subject movement.

Both peak heights and SNR for the three main metabolite peaks behave comparably, so only the average signal and SNR for the three metabolite peaks are discussed, and referred to as "the signal" and "the SNR." The SNR of the mean filtered spectra ranged from 8.4 to 54.3, and was highest for the 8-mL voxel with short echo time and lowest for the 3.4-mL voxel with long echo time. The SNR was (mean ± SD) 29.9 ± 8.3 for the 8-mL voxel with short echo time and 15.1 ± 5.1 the 3.4-mL voxel with long echo time.

The signal and the SNR relative to the signal, as well as the SNR of the mean of all repetitions (both defined as 1) for all motion-rejection algorithms with and without non–motion-distorted acquisitions are shown in Table 1. The acceptance percentage, defined as the percentage of the data points that is accepted by the algorithms described in the Materials and Methods section, is shown in the last column. The values for the subset of the datasets where ICA detected more than one component are given in brackets. The values for the signal, the SNR, and the acceptance

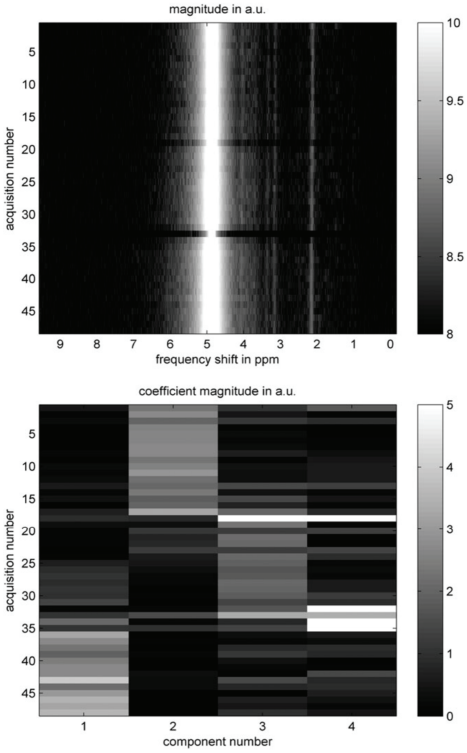

FIG. 1. The spectra of 48 acquisitions of an 8-mL voxel with an echo time of 30 ms for a healthy volunteer (top panel). The volunteer was instructed to move his head 2-3 cm continuously from the left to the right at acquisitions 18-19 and 32-34. Each spectrum is shown as a row, using the grayscale for the log of the magnitude of the signal intensity in arbitrary units (a.u.). The residual water peak at 4.7 ppm is clearly visible, as are metabolite signals at the right-hand side of the water peak. In the bottom panel, the coefficients for the ICA components for the spectra are shown. A grayscale is used to show the amplitude of the coefficients in a.u. The three periods without movement are mainly described by a single component for each period (component 2-3-1), while the spectra during head movement are described by a combination of all four components.

percentage in Table 1 are averaged over all datasets. All motion-rejection algorithms improve the signal and remove movement artifacts. The results for the dataset of the healthy volunteer, see Fig. 1, were similar to the results in Table 1.

Both the signal and the SNR were statistically tested bilaterally between all methods with a paired, double-sided t test. Apart from the difference in the signal for the two OI methods (pointwise OI and OI), all the differences in the signal and the SNR in Table 1 are significant ($P < 0.05$) for all datasets.

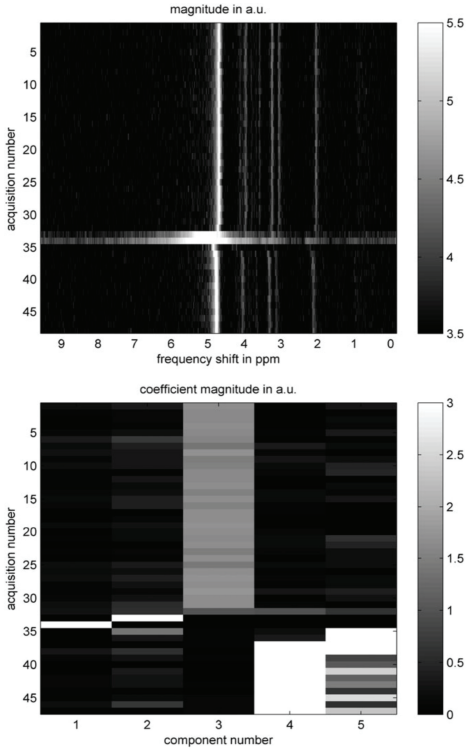

FIG. 2. The spectra of 48 acquisitions of an 8-mL voxel with an echo time of 30 ms for a preterm infant (top). Acquisitions number 33 and 34 are likely to be corrupted by motion, while acquisitions 35 to 48 are likely to be measured at another position (the spectrum is slightly shifted) and should be rejected. In the bottom panel, the coefficients for the ICA components for the spectra are shown. In this case, the most frequent dominant component is component 3, and it is interpreted by the ICA algorithm as the undistorted component. Components 1 and 2 describe acquisitions 33 and 34, which are interpreted as motion corrupted; see top panel. Components 4 and 5 describe the acquisitions 35 to 48. Notice that component 3 almost solely describes the undisturbed data.

ICA and Components

One hundred thirty-eight out of 243 subject spectra (each containing 48 acquisitions) contained more than one component. So in 105 subject spectra, the ICA algorithm finds only one component and identifies differences between this component and the measured signal as noise. The probability of having estimated the correct number of components was less than 100% for 30 of these patient spectra (ranging from 50 to 99%). Of the 138 spectra with more than one component, 43% of the measurements were rejected. The average number of components was 3.2 (range, 1-12; the maximum number of components was set to 12) for all measurements and 3.6 (range, 2-12) for the motion-distorted measurements. On average, 75% of all the measurements were kept.

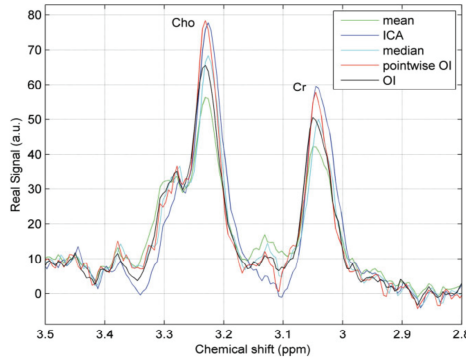

FIG. 3. A part of the zero-order phase-corrected spectrum for a 30-ms echo time after motion rejection with the creatine peak at the right and choline peak at the left. On the left shoulder of the choline peak, the myoinositol resonance at 3.28 ppm is visible. The curves illustrate the performance of the different algorithms, mean, ICA, median, pointwise OI, and OI. It is clearly seen that the median improves the signal and that in this case pointwise OI and ICA perform best in agreement with quantitative analysis.

DISCUSSION

Motion compensation of single-voxel spectroscopy spectra of nonanesthetized infants and other moving patients is necessary. The effect of motion on the spec-

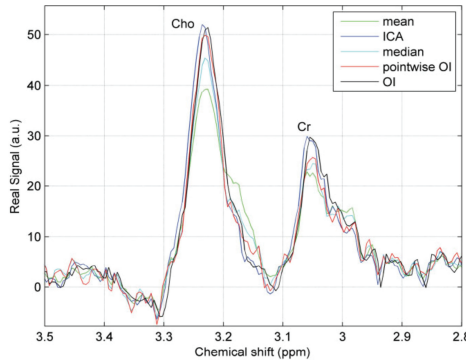

FIG. 4. Graph similar to Fig. 3 but based on data acquired with an echo time of 144 ms. It is seen that the median improves the signal, that pointwise OI performs better, and that in this case ICA and OI perform best in agreement with quantitative analysis.

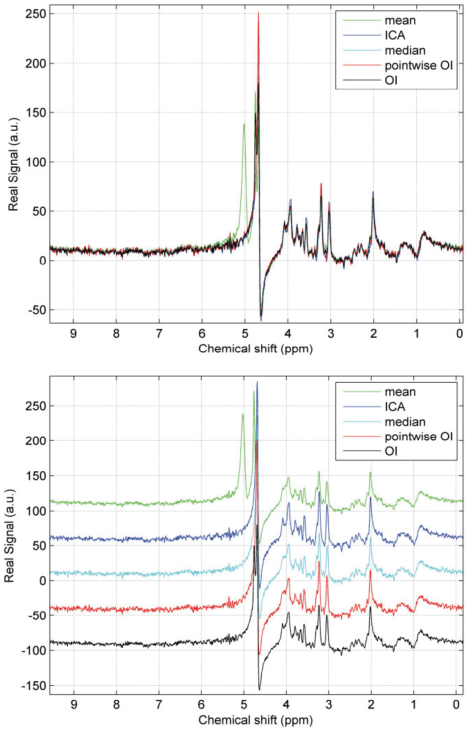

FIG. 5. Entire water-suppressed spectra acquired with an echo time of 30 ms for the same subject as in Fig. 3. The residual water peak at 4.7 ppm is clearly seen. Peaks in the mean signal (green) at 5.1 and 4.8 ppm originate from the residual water signal and subject motion.

trogram of the healthy volunteer in Fig. 1 showed that spectra are corrupted during motion and that the frequency of the metabolite peaks is shifted after motion due to a change of voxel position. During motion of the healthy volunteer, the water peak was reduced while it was increased in the preterm infant. A signal loss as seen in the volunteer spectrum is expected due to imperfect refocusing when motion happens during the spin-echo period of the sequence. A signal increase as seen in the infant spectrum is expected when the water suppression is compromised by movement. The proposed methods detect and compensate both effects.

Visual inspection of the spectra indicates higher signals and better spectral resolution for all the motion-rejection algorithms. In practice, it is not possible to visually appreciate the noise properties of the algorithms; for instance, by observing the signal where no metabolite peaks are present in Fig. 3. Visual inspection also indicates that the ICA methods are better at suppressing the signal just next to the metabolite peaks and that median filtering does not completely remove the influence of outliers, resulting in a lower signal at the metabolite peaks.

Because motion is likely to reduce the peak height, the signal and the SNR are reasonable measurements for the performance of the algorithms, although since true metabolite concentrations are not known, the true performance is also not known. Simulations could be performed to address the issue of the true performance of the algorithms.

If single-voxel spectroscopy with a relatively large voxel of more than 1 mL is used to measure a "global" metabolite concentration, small changes in which the voxel stays within the same tissue of interest are less relevant than in the case where a small voxel is used and a spectrum at a specific position, e.g., the hippocampus, is required. In the latter case it is advisable to perform a localizer scan before and after the spectroscopy measurement in order to ensure that the voxel position is not changed, even though the acquired spectra are not noticeably different. If the exact voxel position is very important, the selection of the ICA component can be altered by identifying the undistorted component as the dominant component of the first acquisition instead of the most frequent dominant component. In this way, the ICA algorithms reject acquisitions that differ significantly from the first acquisition. It is also possible to reject all acquisitions after the first detected movement. On the other hand, the selection of the acquisitions in the ICA method only accepts acquisitions which differ by the ICA-identified noise, which indicates that the underlying noiseless spectrum is unchanged by motion and that the head has therefore probably returned to the original position after motion.

Quantitative evaluation shows that median filtering results in a considerable improvement of the signal and

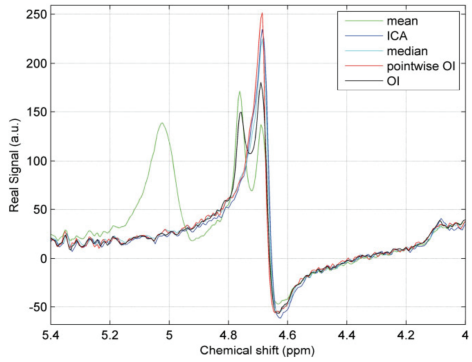

FIG. 6. The 1.4-ppm frequency range around the residual water peak acquired with an echo time of 30 ms for the same subject as in Fig. 3. The residual water peak at 4.7 ppm is clearly seen. Peaks in the mean signal (green) at 5.1 and 4.8 ppm originate from the residual water signal and subject motion. All motion rejection algorithms remove these erroneous water peaks, except the OI with multiple comparisons that fails to remove the peak at 4.8 ppm.

Table 1
The Mean Signal, SNR, and Acceptance Percentage for All Data Sets

Method	Signal	SNR	Acceptance percentage
Mean	1	1	100
Median	1.030 (1.036)	0.849 (0.866)	100
Pointwise OI	1.066 (1.082)	0.739 (0.758)	85.3 (84.8)
OI	1.069 (1.106)	0.939 (0.948)	75.7 (70.6)
ICA mean	1.114 (1.201)	0.950 (0.912)	75.4 (56.7)
ICA all components	1.100 (1.178)	0.976 (0.957)	75.4 (56.7)
ICA main component	1.088 (1.158)	0.970 (0.945)	75.4 (56.7)

Signal is defined as the average height of the NAA, Cho, and Cr peaks). Between brackets, the values for the subset of datasets where ICA detects more than one component, i.e., with motion artifacts, are shown. Signal and SNR are stated relative to the signal and SNR of the mean of all acquisitions.

compensation for movement-distorted spectra. However, it does not perform as well as the other methods, and the SNR is reduced by more than 15% compared to the uncorrected mean signal, although the mean signal may be corrupted. A combination of order-statistics filters such as all-rank selection order-statistics filtering (31) might reduce noise and outlier sensitivity compared to median filtering, but this has not been shown. Pointwise OI has even lower SNR but slightly better signal amplitude compared to the median filter. OI with connection between the consecutive Fourier components did not give this SNR loss and restored the signal well. The relatively conservative P value for the pointwise OI method is necessary, as otherwise too many measurements will be excluded. The OI method with multiple comparisons, however, needs a slightly higher P value in order to reject enough measurements.

The noise depends on the algorithm and it increases if the number of accepted acquisitions n is lower and is proportional to $1/\sqrt{n}$. The signal is increased if the motion-distorted acquisitions are rejected and the SNR is reduced less than expected from the increase in noise only. In general the noise in the median is higher than the noise in the mean. For normal distributions, this is approximately 25%. The SNR is only 15% lower for the median, and this is due to the fact that the median recovers the signal better than the mean. As an estimator, the median is more sensitive to noise, and therefore it is probably better to identify the outliers, reject them, and calculate the mean of the remaining data. OI with multiple comparisons performs better than the median, but the pointwise OI method does not. This is probably because of the noise sensitivity of the (pointwise) outlier detection itself.

The advantages of ICA compared with the other methods are that no arbitrary thresholds need to be set, that both the resulting signal and the SNR are best, and that it provides a possibility to identify outliers without ignoring connections between consecutive Fourier components. Another advantage of the ICA methods is that they make it possible to accept all the measurements if just one component is considered as most probable, for instance if the patient does not move. Also, the range of the acceptance-rate–defined percentage of the measurements that are not rejected indicates larger flexibility. The SD of the acceptance rate considering both movement-distorted and undistorted data for ICA was 25%, while it was 11% for OI and only 1.5% for pointwise OI. The latter is explained by the influence of the majority of the Fourier components, where no metabolite signal is present. The difference between the three versions of the ICA method was small. Using ICA only to identify movement-distorted acquisitions and then taking the mean of the remaining acquisitions gives the highest signal. On the other hand, taking the mean of signals reconstructed with the main or all components showed slightly better SNR.

In the case of a short movement, it is possible that the first few measurements after the movement are transients due to history effects in the spin system. ICA will describe this transition with two or more components. Hereafter, the measurement is described with one component, different from the component found before movement, unless the subject returned to the original position.

ICA instead of the better-known principal component analysis is used because the latter maximizes the explained variance for each component, i.e., minimizing the mean square error of approximating the data, whereas ICA seeks independent components. In the case of a measurement with some motion-distorted acquisitions, principal component analysis finds a mixture of all acquisitions for the first and other components (often after the mean has been subtracted), and because of the large deviations in the motion-distorted acquisitions, the uncorrelated principal components will be mainly determined by distorted acquisitions. This gives no opportunity to identify the motion-distorted acquisitions, while ICA finds the undistorted acquisitions as one independent component and one or more components for the motion-distorted acquisitions.

Phase-coherent averaging after motion rejection will probably increase the SNR even more, but caution is necessary, since it can potentially introduce a bias. In this study, no phase-coherent averaging was applied, because only the performance of the motion rejection algorithms was investigated.

CONCLUSION

Subject movements cannot be ignored in certain patient groups, and they need to be compensated for. This can be done by storing the individual single-voxel spectroscopy acquisitions and identifying and rejecting the acquisitions

distorted by subject movements, followed by phase-correcting (and optionally frequency-shift compensating) the individual remaining acquisitions before averaging. It is strongly advised to implement a procedure to detect subject motion. A first implementation of motion rejection in clinical practice could be to monitor the difference between the mean and the median and compare this with the estimated noise. If the difference is significant, the median instead of the mean should be used, or OI or ICA analysis could be applied to the dataset.

Fully automated ICA analysis proved to be the most powerful and reliable tool for movement identification and rejection. In this study, the signal increased by 20% for the subject-movement–distorted data, keeping the SNR as high as 91% of the SNR of the mean signal and keeping the undistorted patient data unaffected.

REFERENCES

1. Drost DJ, Riddle WR, Clarke GD. Proton magnetic resonance spectroscopy in the brain: report of AAPM MR Task Group #9. Med Phys 2002;29:2177–2197.
2. Jansen JF, Backes WH, Nicolay K, Kooi ME. ^{1}H MR spectroscopy of the brain: absolute quantification of metabolites. Radiology 2006;240:318–332.
3. Felblinger J, Kreis R, Boesch C. Effects of physiologic motion of the human brain upon quantitative ^{1}H-MRS: analysis and correction by retro-gating. NMR Biomed 1998;1:107–114.
4. Katz-Brull R, Rofsky NM, Lenkinski RE. Breathhold abdominal and thoracic proton MR spectroscopy at 3T. Magn Reson Med 2003;50:461–467.
5. Katz-Brull R, Lenkinski RE. Frame-by-frame PRESS ^{1}H-MRS of the brain at 3 T: the effects of physiological motion. Magn Reson Med 2004;51:184–187.
6. Zhu G, Cheorghiu D, Allen PS. Motional degradation of metabolite signal strengths when using STEAM: a correction method. NMR Biomed 1992;5:209–211.
7. Helms G, Piringer A. Restoration of motion-related signal loss and line-shape deterioration of proton MR spectra using the residual water as intrinsic reference. Magn Reson Med 2001;46:395–400.
8. Bolan PJ, Henry PG, Baker EH, Meisamy S, Garwood M. Measurement and correction of respiration-induced B0 variations in breast ^{1}H MRS at 4 tesla. Magn Reson Med 2004;52:1239–1245.
9. Shanbhag DD, Dunham SA, Knight-Scott J. A water signal based navigation echo for localized MRS. In: Proceedings of the 13th Annual Meeting of ISMRM, Miami Beach, Florida, 2005. p 2505.
10. Thiel T, Czisch M, Elbel GK, Hennig J. Phase coherent averaging in magnetic resonance spectroscopy using interleaved navigator scans: compensation of motion artifacts and magnetic field instabilities. Magn Reson Med 2002;47:1077–1082.
11. Bhattacharyya PK, Lowe MJ, Phillips MD. Spectral quality control in motion-corrupted single-voxel J-difference editing scans: an interleaved navigator approach. Magn Reson Med 2007;58:808–812.
12. Pfeuffer J, Juchem C, Merkle H, Nauerth A, Logothetis NK. High-field localized ^{1}H NMR spectroscopy in the anesthetized and in the awake monkey. Magn Reson Imaging 2004;22:1361–1372.
13. Skimminge A, Markenroth K, Hejl A, Hanson LG. Improved spectroscopy using cluster analysis and lipid signals as a motion indicator. In: Proceedings of the 11th Annual Meeting of ISMRM, Toronto, Ontario, Canada, 2003. p 270.
14. Gabr RE, Sathyanarayana S, Schär M, Weiss RG, Bottomley PA. On restoring motion-induced signal loss in single-voxel magnetic resonance spectra. Magn Reson Med 2006;56:754–760.
15. Bottomley PA. Spatial localization in NMR spectroscopy in vivo. Ann N Y Acad Sci 1987;508:333–348.
16. Slotboom J, Nirkko A, van Ormondt D. A comparison of time domain and frequency domain all rank selection order statistics filtering (ARSOS) of single voxel ^{1}H MRS-signals. In: Proceedings of the 15th Annual Meeting of ISMRM, Berlin, Germany, 2007. p 203.
17. Slotboom J, van Ormondt D, Brekenfeld C, Nirkko A, Schroth G. The usage of median filtering for the elimination of patient motion related signal artifacts in single voxel spectroscopy. In: Proceedings of the 22nd Annual Scientific Meeting of ESMRB, Basle, Switzerland, 2005. p 124–125.
18. Slotboom J, van Ormondt D. Elimination of patient-motion artefacts in in vivo MR spectroscopy. In: Proceedings of ProRISC, IEEE Benelux, Veldhoven, The Netherlands, 2006. p 204–207.
19. Rider PR. Variance of the median of small samples from several special populations. J Am Stat Assoc 1960;55:148–150.
20. Kenney JF, Keeping ES. The median, §13.13. In: Mathematics of statistics, pt. 1, 3rd ed. 1962. p 211.
21. Barner KE, Arce GR. Order-statistic filtering and smoothing of time-series: part II. In: Handbook of statistics 17: order statistics: applications. Elsevier; 1998. p 525–602.
22. Thomsen G, de Nijs R, Hogh-Rasmussen E, Frokjaer V, Svarer C, Knudsen GM. Required time delay from (99m)Tc-HMPAO injection to SPECT data acquisition: healthy subjects and patients with rCBF pattern. Eur J Nucl Med Mol Imaging 2008;35:2212–2219.
23. Andersson JLR. How to estimate global activity independent of changes in local activity. Neuroimage 1977;60:237–244.
24. Bell A, Sejnowski TJ. An information-maximization approach to blind separation and blind deconvolution. Neural Comput 1995;7:1129–1159.
25. Kolenda T, Sigurdsson S, Winther O, Hansen LK, Larsen J. DTU: Toolbox, Intelligent Signal Processing group at the Institute of Informatics and Mathematical Modelling at the Technical University of Denmark, 2002, http://isp.imm.dtu.dk/toolbox/.
26. Højen-Sørensen P, Hansen LK, Winther O. Mean field implementation of bayesian ICA. In: Proceedings of the 3rd International Conference on Independent Component Analysis and Blind Signal Separation, San Diego, 2001. p 439–444.
27. Hyvärinen A, Oja E. Independent component analysis: algorithms and applications. Neural Netw 2000;13:411–430.
28. Kolenda T, Hansen LK, Larsen J. Signal detection using ICA: application to chat room topic spotting. In: Proceedings of the 3rd International Conference on Independent Component Analysis and Blind Signal Separation, San Diego, 2001. p 540–545.
29. Hansen LK, Larsen J, Kolenda T. Blind detection of independent dynamic components. In: Proceedings of IEEE International Conference on Acoustics, Speech, and Signal Processing (ICASSP), Salt Lake City, 2001. p 3197–3200.
30. Miller RG. The JackKnife–a review. Biometrika 1974;61:1–15.
31. Slotboom J, van Ormondt D. The effect of order-statistics filtering on the output probability density functions. In: Proceedings of ProRISC, IEEE Benelux, Veldhoven, The Netherlands, 2007. p 254–258.

Original Article www.jmp.org.in

Experimental determination of the weighting factor for the energy window subtraction–based downscatter correction for I-123 in brain SPECT studies

Robin de Nijs, Søren Holm, Gerda Thomsen[1], Morten Ziebell[1], Claus Svarer[1]

Department of Clinical Physiology, Nuclear Medicine, PET and Cyclotron Unit, [1]Neurobiology Research Unit, Department of Neurology, Copenhagen University Hospital, Copenhagen, Denmark

Received on: 11.11.09 **Review completed on:** 15.04.10 **Accepted on:** 19.04.10 **DOI:** 10.4103/0971-6203.71765

ABSTRACT

Correction for downscatter in I-123 SPECT can be performed by the subtraction of a secondary energy window from the main window, as in the triple-energy window method. This is potentially noise sensitive. For studies with limited amount of counts (e.g. dynamic studies), a broad subtraction window with identical width is preferred. This secondary window needs to be weighted with a factor higher than one, due to a broad backscatter peak from high-energy photons appearing at 172 keV. Spatial dependency and the numerical value of this weighting factor and the image contrast improvement of this correction were investigated in this study. Energy windows with a width of 32 keV were centered at 159 keV and 200 keV. The weighting factor was measured both with an I-123 point source and in a dopamine transporter brain SPECT study in 10 human subjects (5 healthy subjects and 5 patients) by minimizing the background outside the head. Weighting factors ranged from 1.11 to 1.13 for the point source and from 1.16 to 1.18 for human subjects. Point source measurements revealed no position dependence. After correction, the measured specific binding ratio (image contrast) increased significantly for healthy subjects, typically by more than 20%, while the background counts outside of all subjects were effectively removed. A weighting factor of 1.1–1.2 can be applied in clinical practice. This correction effectively removes downscatter and significantly improves image contrast inside the brain.

Key words: weighting factors, downscatter correction, SPECT, iodine-123, energy window subtraction

Introduction

Radioisotopes used for imaging with single-photon emission computer tomography (SPECT), such as Technetium-99m, typically emit photons with energy between 100 and 200 keV. This allows effective collimation by lead. These emissions have a photon energy of 159 keV for Iodine-123, which also emits a significant amount of photons with a higher energy (abundance 3.1%). The most important of these have a photon energy of 529 keV and an abundance of 1.4%, whereas the primary photons at 159 keV have an abundance of 83.4%.[1] The high-energy photons are not well collimated, but penetrate through the lead into the scintillation crystal (septal penetration). Photons from parts of the patient's body outside the SPECT scanner may contribute to the projection data by penetration through either the collimator or the camera shield. Compton scatter for 529 keV photons in the sodium iodide crystal of the detector is a far more likely process than photo absorption, and only a minor portion of the counts will be located at the 529 keV photopeak. The resulting photons from scatter in the object will be collimated and are therefore less important than the high-energy photons scattering in the detector. Because the high-energy photons are detected at a lower energy, this process is called downscatter. The resulting spectrum is rather flat above the 159 keV peak, except for a weak and broad backscatter peak at 172 keV. This peak corresponds to photons passing the collimator and crystal without interaction, while being reflected in the material behind the crystal and finally being absorbed. Due to the low efficiency of collimators and the high probability of penetration, the erroneous counts coming from the high-energy photons become a significant fraction of the observed signal at 159 keV, despite their lower abundance. Consequently, the reconstructed SPECT images are deteriorated. The contribution of the high-energy photons depends on the type of collimator and can be significant for low-energy collimators,[2] as demonstrated by the fact that the so-called Compton edge at 358 keV (coming from

Address for correspondence:
Dr. Robin de Nijs,
Department of Clinical Physiology & Nuclear Medicine & PET and Cyclotron Unit, Copenhagen University Hospital, KF 4011, Blegdamsvej 9, DK – 2100, Copenhagen, Denmark
E-mail: robin.de.nijs@rh.regionh.dk

the 529 keV photons) is visible in the energy spectrum [Figure 1a].

The observation of a fairly constant energy spectrum above the 159 keV peak [Figure 1a] suggests that a correction can be estimated from a second energy window with an identical width above the one used for imaging. If a flat energy spectrum is assumed, then the second energy window is just subtracted from the main window before reconstruction.[3–5] However, within the main window at 172 keV, a broad backscatter peak, coming from high-energy photons, is present.[6] Therefore, it is expected that the second energy window has to be weighted with a factor slightly higher than one, depending on the height of the backscatter peak.

The triple-energy window (TEW) method[7] also corrects for downscatter but is based on the subtraction of narrow abutting energy windows, which are potentially noise sensitive in SPECT studies with limited counts (e.g., dynamic). The photons in the narrow abutting window, however, mimic the downscattered photons better than a broad energy window. This is also true for the correction of scatter of the main photons. The scatter correction part of the TEW method mimics scattered main photons better than the broad scatter correction window in the dual-energy window method[8], while the latter is potentially less noise sensitive. Other mathematically more advanced scatter correction methods[9,23] exist, but they demand more sophisticated ways of postprocessing and reconstruction. A downscatter correction by subtracting a uniform off-set[10,11] does not take the difference between spatial distribution of the downscattered and primary photons into account.

The impact of the energy window subtraction on the final images, and the value of the appropriate weighting factor for the second energy window, have been investigated in a brain SPECT study and in experiments with an I-123 point source. The kinetics are influenced by scatter corrections,[12] but this issue is not addressed here.

Materials and Methods

Energy windows and imaging

Measurements were performed with a triple-head IRIX camera (Philips Medical, Cleveland, U.S.A.) fitted with parallel hole, low-energy, general purpose (LEGP) collimators (spatial resolution 8.5 mm at 10 cm distance to the collimator) with an orbit radius of 16.5 cm. Projection data were obtained in 128 × 128 matrix size with an isotropic pixel size of 2.33 mm.

The energy window for the primary imaging photons, with corresponding raw projection data I, was set at 143–175 keV. The energy window for the downscattered photons with projection data D was set at 184–216 keV. Both energy windows have a full width of 32 keV. In order to minimize the contamination of the downscatter window by primary photons (caused by limited energy resolution) a small energy gap (175–184 keV) between the two windows was chosen. Downscatter-corrected projection data J was calculated using the formula:

$$J = I - k \cdot D \qquad .....(1)$$

where k is the spatially invariant weighting factor for the downscatter window.[3–5]

SPECT imaging was performed by recording projection data at 120 fixed angles, with an interval of 3° and a noncircular orbit. The mean radius of rotation was 13.9 cm. Reconstruction of projection data with standard filtered back-projection (FBP), both with and without downscatter correction, was performed in MATLAB 7.5

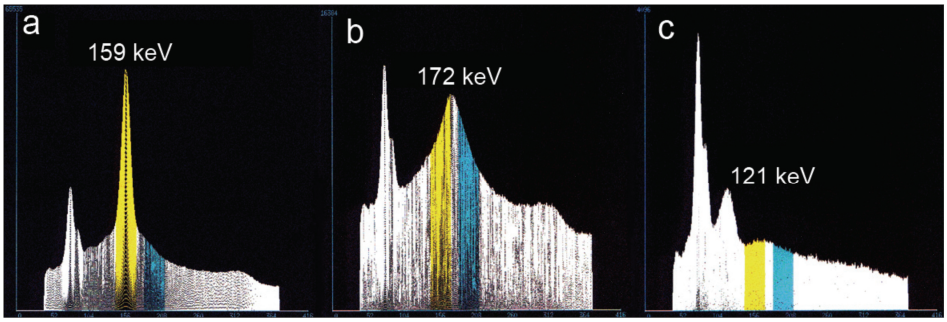

Figure 1: Energy spectra of an iodine-123 point source measured by the SPECT-scanner: (a) unshielded I-123 source in air; (b) source shielded with 6-mm lead, showing a broad peak at 172 keV due to reflected high-energy photons; (c) source placed outside the scanner, showing a peak at 121 keV from 90° Compton scattering of 159 keV photons inside the scanner. The main energy window is highlighted with yellow and the second energy window with cyan

(Mathworks, USA). Matrix size was 128 × 128, with 2.33 mm pixels and identical slice thickness. A 3D low-pass 4th-order Butterworth post-filter with a cut-off frequency of 0.3 Nyquist (= 0.64 cm^{-1}) was used. Attenuation correction with Chang's first-order correction[13] was applied with an empirical linear attenuation factor of 0.10 cm^{-1} for I-123 imaging without Compton scatter correction of the primary 159 keV photons.[11,14-16] The determination of the attenuation map was aided by an algorithm, which finds the most outward placed crossing of a manually set threshold (tuned at the edge) and the intensity for every projection angle in the sinogram [Figures 2a and 2b].

Experimental determination of the weighting factor

The weighting factor k in Equation 1 was determined experimentally with an I-123 point source with 37 MBq activity. The contribution of the primary photons was 'removed' either: (i) by shielding the source with 6-mm lead, thus efficiently excluding the 159 keV photons, and placing the source inside the camera field-of-view (FOV) or (ii) by placing the unshielded I-123 source outside the FOV, near the scanner axis but 20 cm in front of the gantry and placing a 6.3-liter cylindrical water-filled phantom with a diameter of 16 cm inside the scanner as a scattering medium for mimicking a subject.

The camera heads in both experiments were positioned at 90° (collimator surface perpendicular to the floor), 210°, and 330°, and the weighting factor k was determined as the ratio of the total counts between the two energy windows in the raw projection data, using the formula:

$$k = \frac{\sum \mathrm{I}}{\sum \mathrm{D}} \qquad \text{.....(2)}$$

for each angle. The energy spectrum in Figure 1b shows the contribution of the high-energy photons for the lead-shielded I-123 point source (method I) as a broad peak at 172 keV. This energy spectrum is similar to the energy spectrum of a Fluor-18 source (emitting mono-energetic photons of 511 keV) in the SPECT scanner with low-energy collimators. In method II, some of the 159 keV primary photons scatter around 90° in the water-filled phantom and give rise to 121 keV photons, while the primary photons are effectively removed [Figure 1c]. The broad backscatter peak of the high-energy photons at 172 keV was less visible in the latter case.

In order to investigate the spatial dependence of the weighting factor k, pixelwise k-maps were calculated. The statistical uncertainty in k depends on the number of counts. Therefore, a z-score, which does not scale with the amount of counts, was calculated. With I and D the pixel value in the corresponding projection data I and D the z-score for each pixel was defined by the difference between the global k factor defined by Equation 2 and the pixel value $k_{\mathrm{pixel}} = I/D$, normalized by the theoretical standard deviation σ_{pixel}; this was given by the formula

$$z = \frac{k - k_{\mathrm{pixel}}}{\sigma_{\mathrm{pixel}}} \approx \frac{k - \frac{I}{D}}{k \cdot \sqrt{\frac{1}{I} + \frac{1}{D}}} \qquad \text{.....(3)}$$

On the right hand side, the variance (σ^2) of the ratio I/D was approximated, for small variances, by adding the relative variances of I and D. These were expressed, assuming Poisson statistics, as the reciprocal value of the number of counts.

In order to detect significant outliers, the double-sided P-value was calculated from z for every pixel, based on the assumption that the data was normally distributed. Negative differences in Equation 3 were indicated with a negative P-value. All pixelwise P-values were corrected for multiple comparisons with the Bonferroni method, by multiplication with a global scaling factor $P/(1-\sqrt[n]{1-P})$, where P=.05 is the overall significance level and n the number of pixels. For small P-values, the scaling factor is approximately equal to the number of comparisons. Thus, a scaled P-value of .05 corresponds to a double-sided 5% confidence value corrected for multiple comparisons. Since outliers have a low P value, pixelwise 1/P maps were calculated. Pixelwise k-maps and 1/P-maps were investigated in different matrix

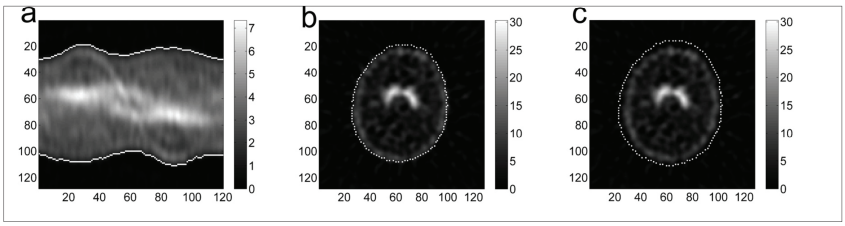

Figure 2: Illustration of the edge detection in a healthy subject (subject 3). The left panel (a) shows the so-called sinogram for a slice. Vertically the tangential position, and horizontally the 120 angles, are shown. The middle panel (b) shows the corresponding reconstructed slice. The edge is shown with maximum intensity (white). The right panel (c) shows the edge with a radial offset of 3 pixels.

sizes because a different balance between uncertainty and spatial resolution can reveal other outliers. Resolution was reduced by box filtering with a uniform kernel, i.e., adding the counts in the kernel area. In this way, Poisson statistics were preserved at the reduced resolution.

Subjects and evaluation of the downscatter correction

The downscatter correction was investigated in human brain studies of the dopamine transporter binding. Five subjects with a high specific binding ratio are referred to as healthy subjects, while five subjects with low specific binding ratio are referred to as patients. All subjects gave their informed written consent and the study was performed in accordance with the ethical standards set out in the Declaration of Helsinki and was approved by the ethical committee of Copenhagen and Frederiksberg (KF 12-009/04).

An average intravenous bolus of 74.3 MBq (range 65.8–79.9 MBq) of ^{123}I-PE2I (MAP-Medical Technologies Oy, Tikkakoski, Finland) was given, immediately followed by a constant infusion (mean 96.5 MBq; range 88.6–100.1 MBq) of ^{123}I-PE2I for 3 hours. The B/I (bolus infusion) protocol was similar in both healthy subjects and patients, with a bolus worth 2.7 hours (range 2.6–2.8 hours) of infusion (the B/I ratio).[17,18] Six SPECT acquisitions of 10-minutes duration each were obtained between 120 and 180 minutes post injection, resulting in typically 3–3.5 million counts (range 2.4–4.2 million counts) in the main energy window for the summed acquisitions. The total amount of counts in the downscatter energy window was approximately 35%–40% of the total counts in the main window.

The performance of the downscatter correction was evaluated as image contrast after reconstruction. The noise properties of the reconstructed images were not investigated in detail in this paper. Image contrast was evaluated as (1) the striatal contrast and (2) the contrast between the intensities of the background outside the subject and the reference region (both of the latter regions are expected to have a uniform intensity). Specific binding ratio (SBR) is used as a measure for striatal contrast, which has the advantage that it is a clinically known and familiar quantity. The SBR is defined as the ratio of the specific striatal count concentration and the reference count concentration in the rest of the brain. Count concentrations are defined by $c \equiv C/V$ and measured in counts/mL with C being the amount of counts and V the volume in milliliters. In order to minimize the subjectivity of drawing VOIs (volumes of interest), a method similar to the one developed by Tossici-Bolt *et al.*[19] was used. This method is not sensitive to the partial volume effect, since all striatal counts are contained in a relatively large VOI covering a larger volume than the striatum. The VOIs were drawn on every slice for each individual subject where the striatum was visible, and the SBR for each striatum was calculated using the formula:

$$\mathrm{SBR} \equiv \frac{c_S - c_{ref}}{c_{ref}} = \frac{1}{V_S} \cdot \left(\frac{C_{VOI}}{c_{ref}} - V_{VOI} \right) \qquad \text{.....(4)}$$

where subscript S refers to the striatum, VOI to the volume of interest around the striatum, and the subscript 'ref' to the reference region. Identical VOIs were used for both reconstructions, with and without downscatter correction. In order to ensure that all the striatal counts were contained in the large VOI, an extra top and bottom slice with VOIs were added. Examples of the VOIs are shown in Figures 3a and 4a. A standard striatal volume of 11.2 mL was assumed.[19] However, due to individual variations, this might be significantly different from the volume measured by a structural MRI scan.[20] For this reason, some caution is needed before interpreting the SBR values determined in this way. In this study, however, the improvement in SBR by downscatter correction is important, and since the striatal volume is a constant scaling factor in Equation 4, it cancels out in the calculation of the relative improvement in SBR.

For comparison with the I-123 source experiments, the weighting factor in each of the 10 subjects was determined by minimizing the background *outside* the subject. There should be no counts, neither primary photons nor scattered primary photons, outside the subject in the corrected projection data, i.e., J = 0 in Equation 1. By using the counts in the region outside the subject only the weighting factor

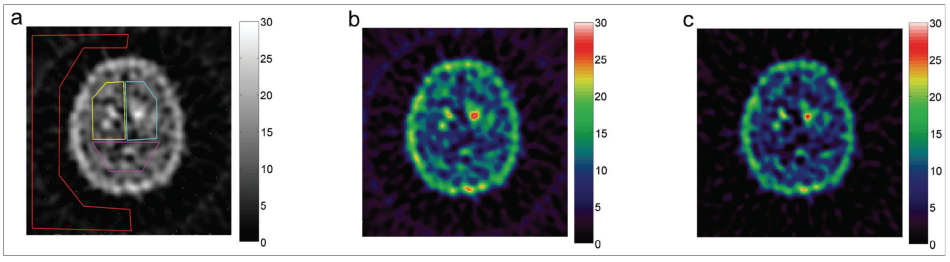

Figure 4: A slice of a reconstructed SPECT image for subject V (patient) in Table 1. The images shown correspond to those in Figure 3.

can be determined by applying Equation 2. The background region for determining k was drawn well outside the head limits, as defined by expanding Chang's attenuation map radially [Figure 2c] by three pixels (= 7 mm). The weighting factor k was calculated with Equation 2 applied to the raw projection data. For one subject, the edge threshold was varied in order to investigate its influence on k [Figure 5]. Differences between subject groups were t-tested, and the stated P-values were calculated by standard two-tailed t-tests. For the independent t-test, equal variance was not assumed.

Results

Figure 6 shows the dataset for the lead-shielded I-123 and the 90° camera configuration (similar results were obtained for the two other configurations of 210° and 330°). The $1/P$ maps show almost no significant differences from the global value of k. To the left of the k map, relatively far away from the source, there may be a larger area with a somewhat lower value of k. In a 8 × 8 matrix this is also indicated by four pixels, with a significant negative difference. As for the I-123 source placed outside the scanner, the maps did not show any significant difference of k from the global value.

The weighting factor k was calculated with Equation 2 for each of the three camera configurations. For the shielded source in the scanner, the respective values of k were 1.123, 1.132, and 1.122. The total number of counts in the primary window was 1.7, 1.1, and 1.7 million counts, respectively. The uncertainty in k due to Poisson statistics was less than 0.002.

Similarly, for the source placed outside the scanner, the values of k were 1.107, 1.109, and 1.115 for the three angles. The total number of counts in the primary window was 0.37, 0.39, and 0.24 million counts. The uncertainty in k due to Poisson statistics was less than 0.003.

Based on these results, a k-value of 1.1 was chosen for the reconstruction of the subject data. The results for the subjects are listed in Table 1, and an example of a reconstructed slice of a healthy subject and a patient are shown in Figures 3 and 4, both with and without downscatter correction. Figures 3a and 4a show the manually drawn regions of interest for determining the specific binding ratio and the contrast between the background and reference region.

For comparison with the I-123 source experiments, the weighting factor k was also determined in the subjects by minimizing the background. It was found to be slightly higher than 1.1 and significantly different ($P<.005$) between healthy subjects and patients, with ranges of 1.155–1.170 and 1.174–1.181, respectively. The uncertainty in k, caused by the limited amount of counts, was 0.002 for all subjects.

The background in the image was effectively removed by the downscatter correction for all subjects [Figures 3c and 4c]. Downscatter (with k=1.1) and non-downscatter–corrected images are visually comparable, but show improved contrast. Because of the energy window subtraction, the mean amount of counts in the reference

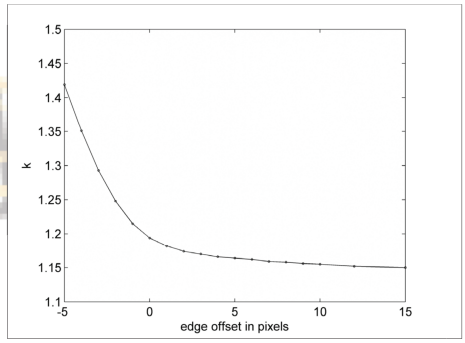

Figure 5: The calculated weighting factor k for subject 3 as a function of the edge-offset. Within the subject (offset<0) the assumption of no primary photon counts for the calculation of k is not valid.

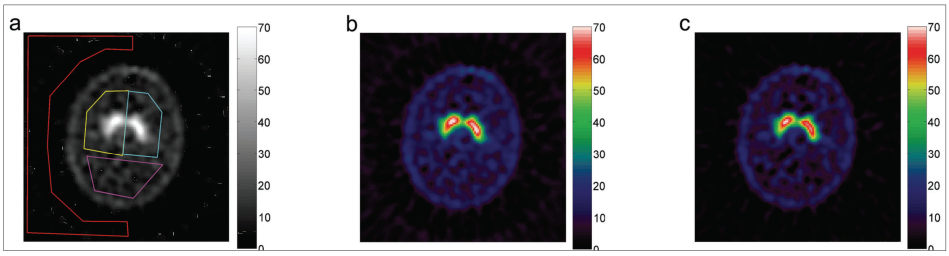

Figure 3: A reconstructed slice subject 3 (healthy) in Table 1. The regions of interest are shown in (a). The ROIs for the left stratium, right striatum, the reference region, and the region outside the brain are drawn in yellow, cyan, magenta, and red, respectively. The reconstructed slice is shown without downscatter correction (b) and with downscatter correction (c). Note the lower background and the improved contrast between the striatum and reference region. The amount of counts in the striata is slightly lower with correction, and the background outside the head is minimized by the correction.

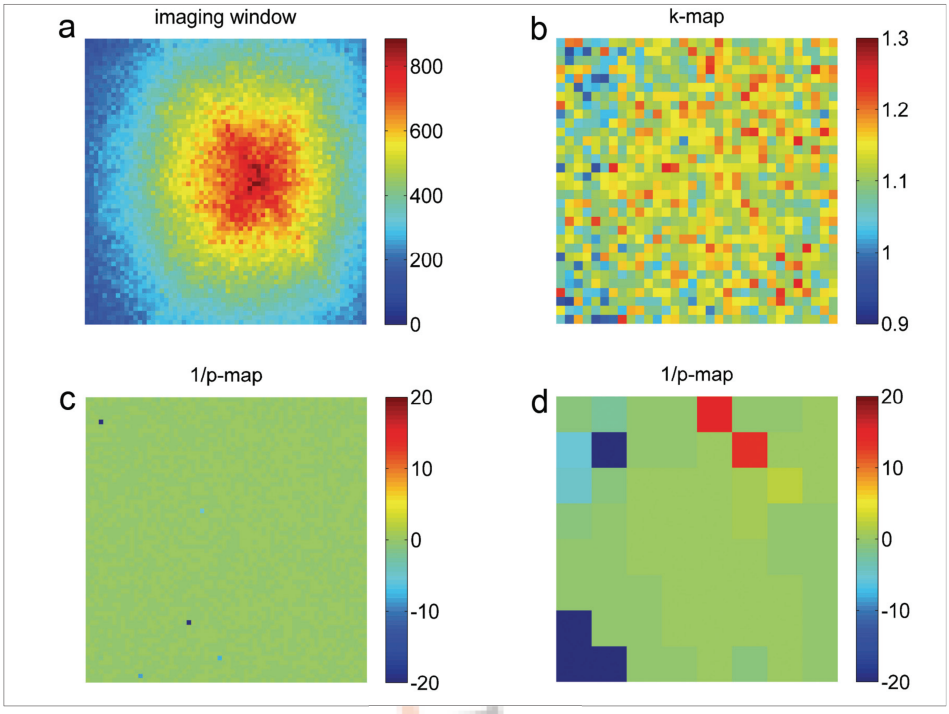

Figure 6: Projection data acquired by placing a 6-mm lead-shielded I-123 source in the SPECT scanner: (a) for energy window 1 (143–175 keV) in a 64 × 64 matrix size, data for energy window 2 (184–216 keV) looks similar to (a) (not shown); (b) the ratio (k map) of the two energy windows in a 32 × 32 matrix size; (c) 1/P maps in a 64 × 64 (c) and (d) 8 × 8 matrix size. The P-values correspond to Bonferroni-corrected double-sided significance levels. A 1/P value of 20 corresponds to a significance level of 5%. Negative P-values indicate negative differences.

region, the background, and (in lesser degree) in the striatal region is decreased. This is because the reduction in mean counts in the striatal region is comparatively smaller than that in the reference region.

The contrast between background outside the subject and the reference region decreased from 0.15 ± 0.02 to 0.00 ± 0.01 (mean ± SD). A *t*-test revealed a significant difference ($P<.005$) between the SBR, both with and without downscatter correction for each striatum in healthy subjects. The uncertainty in SBR due to the limited amount of counts is approximately 0.1 or less. The difference in SBR was not significant ($P>.2$) for the patient group. SBR for the healthy subjects was increased by 23% ± 3% and 22% ± 5% (mean ± SD) for the left and right striatum, respectively. The relative SBR change in the striatum for patients ranged from −13.5% to 16.9% (left striatum) and from −10.0% to 20.2% (right striatum). Linear regression without intercept revealed a slope of (1.21 ± 0.01) between corrected and uncorrected SBRs for all subjects and for both left and right striatums in Table 1. The correlation coefficient was 99.8%.

Figure 7 shows an intensity profile though the left striatum of the healthy subject, both with and without downscatter correction. In a typical patient study, the amount of counts in the downscatter window is approximately 35%–40% of the amount of counts in the main window, which is comparable to the value reported by Du *et al.*[21]

Discussion

A possible explanation for the small differences in k between the three camera configurations and the two setups with the iodine source could be the uncertainty in the calibration of the camera heads, the electronic noise, or a small geometrical dependency of k.

Inspection of the images in Figure 6 reveals a fairly uniform value of k. Smaller values of k are possibly observed in areas of no importance, far away from the source. Similar

results are observed when the iodine source is placed outside the scanner (images not shown). This indicates that the assumption of spatial invariance is within reason. More counts, however, might reveal more significant differences.

Figure 5 shows the dependency of calculation of k on the edge offset for a healthy subject. The determined weighting factor increases with decreasing edge offset. The assumption of no primary photons is not valid close to the edge and this results in a too high a value of k. The value of k determined at a distance of 3 pixels (edge offset) to the head for a 2-pixel thick layer was calculated as 1.245 ± 0.009. This indicates that the k factor is slightly higher for projection lines going through the head. Source–detector distance dependency of the downscatter count rate has been reported before.[2,3] Should this distance dependency be energy dependent, this might explain the distance dependency of weighting factor k.

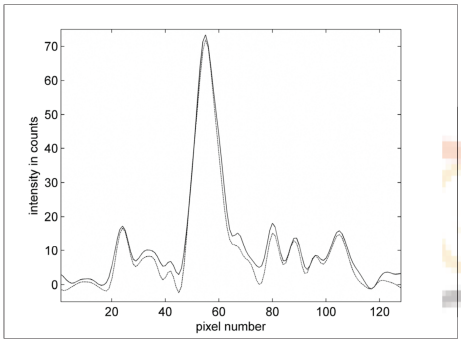

Figure 7: Intensity profile from front to the back of the head through the maximum of the left striatum of subject 3 [Figure 3]. The solid line is without downscatter correction, and the dashed line is with downscatter correction. Maximum intensities are similar, but the intensities are lower in the brain regions outside the striatum and close to zero outside the head.

The small but statistically significant difference in k between healthy subjects and patients might be caused by more uniform distribution of activity in the brain in patients.

Downscattered photons are not collimated and therefore a sinogram of these photons (not shown) has very limited visible structure and subtraction of the downscatter energy window has to be performed *before* reconstruction. Downscatter correction is not necessary if medium energy collimators are used, since the amount of detected downscattered high-energy photons is negligible; however, this is at the cost of a loss in sensitivity.

The largely improved SBRs for healthy subjects make discrimination between healthy subjects and patients easier. The effect of the novel result of a higher value (compared to one) of the weighting factor on the SBR is not profound, though it is not completely negligible. In healthy subjects with an SBR of approximately 10, the SBR compared to the calculated SBR for k=1 is increased by 0.3 for k=1.1 and 0.6 for k=1.2.

The chosen downscatter window is on the high-energy side of the backscatter peak, while the main window is placed on the low-energy side of the backscatter peak. A downscatter window around a higher energy will result in a higher value for the weighting factor. With the energy windows used in this paper, the weighting factor is close to one because the maximum of the backscatter peak is situated between the two window positions.

Contrast might be improved even more by applying a scatter correction for the primary photons. This might be included by one or more energy windows below the main window, as in the dual-energy window scatter correction for Tc-99m[8] (later adapted for I-123 by Luo *et al.*[22]). An extra complication is the contribution of downscattered

Table 1: Results of the evaluation for five healthy subjects (1–5) and five patients (I–V).

Subject	*k*	*SBR left*	*%*	*SBR right*	*%*	*Background/ reference*
1.	1.159	6.17/7.35	19.2	6.14/7.07	15.1	0.162/0.008
2.	1.168	9.22/11.03	19.7	8.76/10.43	19.0	0.134/0.006
3.	1.170	10.14/12.61	24.4	9.72/12.28	26.4	0.152/ 0.014
4.	1.163	8.45/10.70	26.6	9.13/11.32	24.1	0.152/−0.013
5.	1.155	9.25/11.46	23.9	7.91/9.93	25.6	0.133/−0.003
I.	1.179	2.11/2.28	7.9	2.06/2.31	12.3	0.119/−0.013
II.	1.174	3.99/4.66	16.9	5.50/6.61	20.2	0.117/0.004
III.	1.180	1.43/1.23	−13.5	1.72/2.02	17.9	0.141/0.007
IV.	1.181	5.30/5.69	7.3	4.38/4.50	2.7	0.155/0.004
V.	1.177	1.25/1.21	−3.1	1.57/1.42	−10.0	0.202/0.006

In the numerical fields where two values are separated by a slash, the first value is without downscatter correction (k = 0) and the second value is with downscatter correction (k = 1.1). The last column shows the contrast between background and the reference region. Uncertainty due to the amount of counts in SBR is of the order of 0.1. The percent symbol indicates the column with the relative improvement due to the downscatter correction

photons to the scatter energy window. The weight for the downscatter window needs to be reduced in this case.

Downscatter correction by energy window subtraction can easily be performed and is chosen because other techniques, such as the TDCS (transmission-dependent convolution subtraction) technique, demand advanced postprocessing.[9] Add to that the fact that the downscatter correction in the TDCS technique is often added as a rather crude constant scatter fraction.[10,11] The triple-energy window method[7] is straight forward, but suffers from noise sensitivity[23] for low count SPECT-studies. If a broad downscatter window is used, no noise issues are caused by the correction.

Conclusion

Septal penetration of high-energy photons reduces the contrast of I-123 SPECT images if low-energy collimators are used, but it can be corrected in a simple and effective way by subtraction of a second (higher) energy window from the raw emission data. Two novel methods for determining the weight of the second energy window have been presented in this article, the first based on phantom work and the second on the minimization of the background in the projection images before reconstruction.

The value of the weighting factor was found to be slightly higher than one, a consequence of the structure of the downscatter energy spectrum above the main window. In clinical practice, a spatially invariant weighting factor with a value of $k=1.1–1.2$ (or experimentally determined on-site) can be used. Correcting for high-energy photons significantly improves the contrast between high- and low-count regions. In the case of SPECT brain studies of the dopamine transporter with the PE2I tracer, the contrast was improved by more than 20% in healthy subjects.

References

1. Kocher DC. Radioactive Decay Data Tables. Report DOE/TIC-11026: Technical Information Center. U.S. Department of Energy, Washington, D.C.; 1981
2. Dobbeleir AA, Hambye AS, Franken PR. Influence of high-energy photons on the spectrum of iodine-123 with low- and medium-energy collimators: Consequences for imaging with 123I-labelled compounds in clinical practice. Eur J Nucl Med 1999;26:655-8.
3. Small AD, Prosser J, Motherwell DW, McCurrach GM, Fletcher AM, Martin W. Downscatter correction and choice of collimator in 123I imaging. Phys Med Biol 2006;51:N307-11.
4. Kobayashi H, Momose M, Kanaya S, Kondo C, Kusakabe K, Mitsuhashi N. Scatter correction by two-window method standardizes cardiac I-123 MIBG uptake in various gamma camera systems. Ann Nucl Med 2003;17:309-13.
5. Motomura N, Ichihara T, Takayama T, Aoki S, Kubo H, Takeda K. [Practical compensation method of downscattered component due to high energy photon in 123I imaging]. Kaku Igaku 1999;36:997-1005.
6. Tanaka M, Uehara S, Kojima A, Matsumoto M. Monte Carlo simulation of energy spectra for (123)I imaging. Phys Med Biol 2007;52:4409–25.
7. Ogawa K, Harata Y, Ichihara T, Kubo A, Hashimoto S. A practical method for position-dependent Compton-scatter correction in single photon emission CT. IEEE Trans Med Imaging 1991;10:408-12.
8. Jaszczak RJ, Greer KL, Floyd CE Jr, Harris CC, Coleman RE. Improved SPECT quantification using compensation for scattered photons. J Nucl Med 1984;25:893-900.
9. Larsson A, Ljungberg M, Mo SJ, Riklund K, Johansson L. Correction for scatter and septal penetration using convolution subtraction methods and model-based compensation in 123I brain SPECT imaging-a Monte Carlo study. Phys Med Biol 2006;51:5753-67.
10. Ito H, Iida H, Kinoshita T, Hatazawa J, Okudera T, Uemura K. Effects of scatter correction on regional distribution of cerebral blood flow using I-123-IMP and SPECT. Ann Nucl Med 1999;13:331-6.
11. Fujita M, Varrone A, Kim KM, Watabe H, Zoghbi SS, Seneca N, *et al*. Effect of scatter correction on the compartmental measurement of striatal and extrastriatal dopamine D2 receptors using [123I] epidepride SPET. Eur J Nucl Med Mol Imaging 2004;31:644-54.
12. Kim KM, Watabe H, Shidahara M, Onishi Y, Yonekura Y, Iida H. Impact of scatter correction in the kinetic analysis of a D2 receptor ligand SPECT study. IEEE Medical Imaging Conference. San Diego; 2001. p. 1509-12.
13. Chang LT. A method for attenuation correction in radionuclide computed tomography. IEEE Trans Nucl Sci 1978;25:638–43.
14. Shiga T, Kubo N, Takano A, Kobayashi J, Takeda Y, Nakamura F, *et al*. The effect of scatter correction on 123I-IMP brain perfusion SPET with the triple energy window method in normal subjects using SPM analysis. Eur J Nucl Med Mol Imaging 2002;29:342-5.
15. Zaidi H, Montandon ML. Which attenuation coefficient to use in combined attenuation and scatter corrections for quantitative brain SPET? Eur J Nucl Med Mol Imaging 2002;29;967-9.
16. Zaidi H, Montandon ML. Which attenuation coefficient to use in combined attenuation and scatter corrections for quantitative brain SPET? Eur J Nucl Med Mol Imaging 2002;29:969-70.
17. Pinborg LH, Ziebell M, Frøkjaer VG, de Nijs R, Svarer C, Haugbøl S, *et al*. Quantification of 123I-PE2I binding to dopamine transporter with SPECT after bolus and bolus/infusion. J Nucl Med 2005;46:1119 27.
18. Ziebell M, Thomsen G, Knudsen GM, de Nijs R, Svarer C, Wagner A, *et al*. Reproducibility of [123I]PE2I binding to dopamine transporters with SPECT. Eur J Nucl Med Mol Imaging 2007;34:101-9.
19. Tossici-Bolt L, Hoffmann SM, Kemp PM, Mehta RL, Fleming JS. Quantification of [123I]FP-CIT SPECT brain images: An accurate technique for measurement of the specific binding ratio. Eur J Nucl Med Mol Imaging 2006;33:1491-9.
20. Koikkalainen J, Hirvonen J, Nyman M, Lötjönen J, Hietala J, Ruotsalainen U. Shape variability of the human striatum--Effects of age and gender. Neuroimage 2007;34:85-93.
21. Du Y, Tsui BM, Frey EC. Model-based compensation for quantitative 123I brain SPECT imaging. Phys Med Biol 2006;51:1269-82.
22. Luo JQ, Koral KF. Background-adaptive dual-energy-window correction for Compton scattering in SPECT. Nucl Instr and Meth in Phys Res A 1994;353:340-3.
23. Zaidi H, Koral KF. Scatter modelling and compensation in emission tomography. Eur J Nucl Med Mol Imaging 2004;31:761-82.

Source of Support: Nil, **Conflict of Interest:** None declared.